DISSERTATION

HYPERPOLARIZED AND THERMALLY POLARIZED QUADRUPOLAR NOBLE GAS NUCLEI STUDIED BY NUCLEAR MAGNETIC RESONANCE SPECTROSCOPY AND MAGNETIC RESONANCE IMAGING

Submitted by

Karl F. Stupic

Department of Chemistry

In partial fulfillment of the requirements

For the Degree of Doctor of Philosophy

Colorado State University

Fort Collins, Colorado

Spring 2010

COLORADO STATE UNIVERSITY

March 2, 2010

WE HEREBY RECOMMEND THAT THE DISSERTATION PREPARED UNDER OUR SUPERVISION BY KARL F. STUPIC ENTITLED HYPERPOLARIZED AND THERMALLY POLARIZED QUADRUPOLAR NOBLE GAS NUCLEI STUDIED BY NUCLEAR MAGNETIC RESONANCE SPECTROSCOPY AND MAGNETIC RESONANCE IMAGING BE ACCEPTED AS FULFILLING IN PART REQUIREMENTS FOR THE DEGREE OF DOCTOR OF PHILOSOPHY.

Committee on Graduate Work

_____
Jacob L. Roberts

_____
Amy L. Prieto

_____
Grzegorz Szamel

_____
Ellen R. Fisher

_____
Advisor: Thomas Meersmann

_____
Department Chair: Ellen R. Fisher

ABSTRACT OF DISSERTATION

HYPERPOLARIZED AND THERMALLY POLARIZED QUADRUPOLAR NOBLE GAS NUCLEI STUDIED BY NUCLEAR MAGNETIC RESONANCE SPECTROSCOPY AND MAGNETIC RESONANCE IMAGING

This dissertation consists of several studies of two quadrupolar nuclei, ^{83}Kr and ^{131}Xe, with nuclear spin states of I = 9/2 and I = 3/2, respectively. These nuclei possess a nuclear electric quadrupole moment that strongly interacts with the surrounding electric field gradient (EFG). The quadrupolar interactions in these noble gas atoms dominate the longitudinal (T_1) spin relaxation. To fully study these nuclei, high non-equilibrium nuclear spin polarization, referred to as hyperpolarization (hp), is generated using spin exchange optical pumping (SEOP). By employing this technique, enhanced nuclear magnetic resonance (NMR) signals many orders of magnitude above that of a thermally polarized (Boltzmann distribution of spin states) sample are possible and allow for experiments where signal averaging over long periods of time is prohibited (i.e. *in vivo*).

The gas phase ^{83}Kr T_1 is shown to be sensitive to the surface composition/chemistry and the surface-to-volume ratio in an ideal system of closest packed glass beads. Understanding the behavior of ^{83}Kr in these conditions allows for its development as a surface sensitive probe that could provide information in opaque porous media environments. Similar relaxation behavior can be observed in ^{131}Xe; however, the

quadrupolar interactions experienced by ^{131}Xe also induce an observable splitting in the NMR spectrum. This quadrupolar splitting is extremely sensitive to surfaces during periods of adsorption as well as to the magnetic field strength when a ^{131}Xe atom is present in the bulk gas phase. As the influence on the quadrupolar splitting can be more readily observed than the relaxation of either ^{83}Kr or ^{131}Xe, the observed splitting in ^{131}Xe NMR can provide helpful insights into quadrupolar behavior experienced by both nuclei. To develop a better understanding of the quadrupolar behavior, both ^{131}Xe quadrupolar splitting and ^{83}Kr relaxation are explored as functions of magnetic field strength, gas phase composition and co-adsorbing species.

In closing, improvements in polarization of ^{83}Kr from line-narrowed diode array lasers as well as new delivery techniques have provided improvements that allow for the implementation of variable flip angle FLASH imaging sequence in an excised, intact rat lung. Additionally, initial evidence suggests the T_1 of ^{83}Kr can differentiate between the regions of the lung (the trachea, the bronchi and bronchioles, and the alveoli), which has potential as a diagnostic tool for the biomedical community. Improvements in signal intensity are needed to achieve *in vivo* studies, additional enhancements are possible through improved SEOP and by using isotopically enriched gases.

Karl Francis Stupic
Department of Chemistry
Colorado State University
Fort Collins, CO 80523
Spring 2010

"*Now this is not the end. It is not even the beginning of the end. But it is, perhaps, the end of the beginning.*"

- Winston Churchill

ACKNOWLEDGEMENTS

While I have pursued this degree for a number of years at CSU, the path I have taken to this degree started much further back then the degree itself. In reaching the end of this degree, and entering into the research world, I would be remiss if I did not thank the numerous people who have helped along the way. Though only a few are mentioned here, to everyone I have met on this journey, thank you.

I would like first to thank my adviser Professor Thomas Meersmann. I am grateful to have had the chance to watch the development of new research techniques from very early stages and to have contributed to it. Thanks to his enthusiasm, support, and the freedom to explore research ideas, I have had learn nearly as much breadth of science as I have depth of NMR and MRI. I would also like to thank all the members of the Meersmann group who I have had the opportunity to meet: Dr. Zackary Cleveland (originally a graduate student as well), Dr. Galina Pavlovskaya, Charlene Horton-Garcia, Catherine F. LeNoir, Ramon Saavedra, Markus Seitz, and Dr. Elias Haddad. Most of the initial work presented in this dissertation was done with the help and insights of Zackary

and Galina. I would particularly like to thank Zackary and Catherine for their friendship and being my companions on the path towards this degree. I am also grateful for the collaborators we have had while working on the myriad of projects we have done, particularly: Prof. John E. Repine, Nancy Elkins, Dr. Jan Wooten, and Prof. Randall Basaraba. I have also had very interesting and stimulating conversations over the years with Dr. Michael Barlow, Prof. Boyd Goodson, and Prof. David Grainger.

I owe many thanks to a large number of people within the Chemistry Department at CSU. Prof. Gary Maciel and his group have always been willing to lend help in the form of equipment, research materials, and expertise over the years. The highly skilled specialists that make up the shops of CSU and the Department of Chemistry, in particular Michael Olsen, Tom Frederick, Elden Burk, and James Shorkey, each of whom have built many critical pieces of equipment for my research. I would especially thank Michael Olsen for not only his amazing work with all of our "standard" glassware, but also countless thought provoking discussions involving all aspects of our research, and his never ending ability to envision and create equipment out of glass that I would never have thought possible. Also the Physical Chemistry division for their support, discussions, and interest in helping their students succeed with whatever career path they choose.

While CSU has been my home for many years, my love of science and engineering started back home with science teachers in rural Pennsylvania that were truly excited to teach the unformed minds of adolescents. I will be forever in debt to Beth Keim for being driven to work with high school students and develop their abilities for competitions such as the National Science Olympiad. The multitude of science at these

competitions would cement my interest in science. She would also set me on a course to my first scientific home, Juniata College. The atmosphere of Juniata as well as the professors, whose love of teaching and learning seems endless, would shape my mind and set me on a path from which I have never looked back. I am indebted to the entirety of the Departments of Chemistry and Physics at Juniata for their support and encouragement of my studies, past and present. I also thank Dr. Edward Hagaman of Oak Ridge National Laboratory for my initial interest in NMR. He took on a sophomore "organic" chemist and believed he could make an NMR spectroscopist out of him.

Over the years of CSU and Juniata, I have made many unforgettable friends that have made this journey all the more special. Elizabeth Denning who, since our first day at Juniata, has been my best friend and a source of strength as we both worked through our respective programs. Aimee Morris for the many lunches and coffees discussing work, class, and our lives since the day we joined the Department of Chemistry at CSU. Ina Martin who provided many times a welcome ear, guidance, and a different point of view not only on research but also on life itself. Myles Sedgwick whom I have spent many hours bouncing research ideas off of and an equal number of hours letting off steam after long days in the lab.

Many thanks are also due to Theresa Denison whose care and support over the last year and a half of my degree, including the much needed company during many a working weekend, has been much desired and continues to be uplifting.

Finally, I wish to especially thank my parents Joan and James Stupic and my sister Stephanie Putt. Their support and encouragement has never wavered and

Stephanie's love of editing has been a much-appreciated gift. Without my family, this would never have been possible.

DEDICATION

I dedicate this work to my parents, Joan and James Stupic. Their never ending support of my endeavor for this Ph. D. has been a much needed and well used constant in my life. Since the moment I applied to programs, they have supported every decision I have made. While some of these decisions have involved moving away from home, they have never questioned my choices, instead offering me even more support and opportunities.

Mom, Dad, this is for you.

TABLE OF CONTENTS

CHAPTER 1

Introduction of NMR, MRI, Spin Exchange Optical Pumping with regards to Quadrupolar Noble Gas Nuclei ^{83}Kr and ^{131}Xe

1.1 Background and motivation

Optical pumping was first reported by Kastler in 1950 [1]. He demonstrated that the interaction of circularly polarized light with mercury, Hg, resulted in the production of non-equilibrium population distributions of the electronic spins. Ten years after Kastler's study, optical pumping of an alkali metal, rubidium (Rb), was shown to induce a non-equilibrium polarization in the nuclear spins of ^{3}He via collision and spin-exchange [2]. Initial work with non-equilibrium polarization in ^{3}He was for applications as nuclear spin targets [3; 4] for particle physics. Over the decades, this non-equilibrium polarization, referred to as hyperpolarization (hp), has been obtained for all of the noble gas nuclei (details listed in Table 1.1) [2; 5; 6; 7; 8]. Additionally, spin exchange optical pumping (SEOP) has resulted in polarization of over 75% for the nuclei ^{3}He [9] and ^{129}Xe [10]. Hyperpolarization of noble gas nuclei has had an enormous impact on nuclear magnetic resonance (NMR) spectroscopy and magnetic resonance imaging (MRI) in the gas phase because the SEOP process overcomes the inherent insensitivity of the techniques.

NMR spectroscopy has low signal-to-noise compared to other analytical techniques, requiring approximately 10^{14} nuclei for signal detection. However, as NMR utilizes radio frequency (RF) pulses to observe spin active nuclei and RF can penetrate opaque non-conducting, non-magnetic media, this technique provides a non-invasive, non-destructive technology. Magnetic resonance (MR) studies of thermally polarized gases (i.e. gases with a Boltzmann distribution of nuclear spin states) are difficult due to low signal intensity. NMR, MRI, and *in vivo* MR involving thermally polarized gases are

Isotope	Spin	Natural Abundance	Gyromagnetic Ratio (γ) / 10^7 rad/Ts	Frequency Ratio $\left\|\gamma/\gamma_{^1H}\right\|\cdot 100\%$	Quadrupolar Moment (Q) / 10^{28} m^2
^{3}He	1/2	1.30×10^{-04}	-20.38	76.18%	---
^{21}Ne	3/2	0.26	-2.11	7.90%	9.00×10^{-02}
^{83}Kr	9/2	11.55	-1.03	3.90%	0.26
^{129}Xe	1/2	26.44	-7.44	27.81%	---
^{131}Xe	3/2	21.18	2.21	8.25%	-0.12

Table 1.1: Spin properties of stable, spin active, noble gas isotopes (from [11])

therefore impractical or impossible, as rapid data acquisition is required. These studies become feasible when SEOP is used to generate hp noble gas nuclei. Noble gas nuclei are of particular interest for medical MRI of the respiratory system. Medical MRI typically measures the ^{1}H nucleus due to its natural abundance and prevalence in the body; unfortunately, the respiratory system largely consists of void space and does not contain sufficient spin density for high-resolution imaging in the gaseous regions. However, by inhaling a quantity of hp noble gas, the requirements for high-resolution imaging in the respiratory system can be met. This was first shown for hp ^{129}Xe [12] followed shortly thereafter by hp ^{3}He [13].

^{3}He ($I = 1/2$) has the largest gyromagnetic ratio of the noble gas nuclei, resulting in a resonant frequency approximately 3/4 that of ^{1}H. Additionally, in the absence of paramagnetic species such as oxygen and iron, the longitudinal relaxation time (T_1) for ^{3}He approaches hundreds of hours [9]. With SEOP, this leads to high non-equilibrium polarizations that can be applied to high resolution MRI of lungs [14] and can provide information about alveolar size [15; 16]. However, ^{3}He has no chemical shift range, which limits ^{3}He MR studies to systems that require high signal intensity (via SEOP) or that are in contact with a relaxation-inducing agent. ^{3}He spin relaxation is sensitive to the presence of oxygen, and this sensitivity can be used to study oxygen partial pressures in lungs [17]. For *in vivo* studies, where oxygen must be present in a breathable mixture, the T_1 of ^{3}He is reduced to 10 – 20 s. In addition to the lack of chemical shift information, the reduction of the ^{3}He T_1 by paramagnetic relaxation dominates over any other relaxation interaction, making ^{3}He relaxation an insensitive probe for surfaces in the presence of oxygen.

^{129}Xe is another noble gas isotope with nuclear spin $I = 1/2$. ^{129}Xe has a smaller gyromagnetic ratio than ^{3}He and a shorter relaxation time than that of ^{3}He, approximately two hours in the gas phase [12]. However, ^{129}Xe has a chemical shift range of 300 ppm [18] that is not available with ^{3}He. Interest in ^{129}Xe began in the areas of material science and rapidly expanded to the biomedical field (material science reviews: [19; 20; 21; 22; 23]; biomedical reviews: [24; 25; 26]). ^{129}Xe has been used with NMR to explore systems such as single file diffusion in nanochannels [27; 28], combustion [29], and nanoporous media [30; 31; 32; 33; 34]. One aspect of xenon that is of interest to the biomedical community is the solubility of xenon into biological tissue (approximately 10%) [35]. ^{129}Xe experiences reduced T_1 times in the presence of oxygen in the range of 10 – 20 s. T_1 times for ^{129}Xe in biological fluids of tens of seconds has allowed for *in vivo* studies with ^{129}Xe in biological systems such as blood [36] and brain tissue [37; 38]. Hp ^{129}Xe was also explored for molecular imaging using functionalized xenon biosensors [39; 40] and was infused directly into blood for MR imaging applications [41].

This dissertation focuses on two of the quadrupolar noble gas nuclei, ^{83}Kr (I = 9/2) and ^{131}Xe (I = 3/2), and their development for NMR and MRI applications. As both nuclei possess a spin $I > 1/2$, they have a nuclear electric quadrupole that is sensitive to its surrounding environment. When the spherical electron cloud of these atoms becomes distorted, during events such as adsorption onto surfaces, electric field gradients (EFGs) are formed that interact with the nuclear electric quadrupole moment. These interactions lead to short longitudinal relaxation times for both nuclei, and in ^{131}Xe, an observable quadrupolar splitting. ^{83}Kr studies focus on understanding relaxation behavior such that applications to *in vivo* systems can be considered. ^{131}Xe, with its smaller spin quantum

number than ^{83}Kr, is studied in an effort to understand fundamental quadrupolar interactions via NMR spectra instead of relaxation experiments that could be time prohibitive.

1.2. Fundamentals of NMR spectroscopy and MR imaging

1.2.1. Signal intensity in NMR spectroscopy at thermal equilibrium

A nucleus with non-zero spin has a nuclear magnetic moment, μ, defined as $\mu = \gamma I$, where γ is the gyromagnetic ratio of the nucleus and I is the nuclear spin state of the nucleus. The orientation of the nuclear magnetic moment is arbitrary until it experiences a magnetic field, B_0. In a magnetic field, the macroscopic ensemble of the nuclear magnetic moments of the spins align with or against B_0. The direction of the B_0 is defined by convention to be the z-axis. Therefore, a net nuclear magnetization M_z will be produced upon realignment of spins; the observed NMR signal is proportional to M_z.

All spectroscopic techniques are based on observed transitions between energy levels; quantum mechanically:

$$\hat{H}\psi = E\psi \,, \qquad \text{[Eq. 1.1]}$$

where ψ is the spin wave function for NMR. The Hamiltonian operator for NMR is:

$$\hat{H} = -\gamma\hbar B_0 \hat{I}_z \,, \qquad \text{[Eq. 1.2]}$$

where ħ is Plank's constant divided by 2π and $\hat{I}_z$ is the z component of the spin operator $\hat{\mathrm{I}}$. $\hat{I}_z$ represents the eigenvalues $m = -I$ to $+I$ in steps of one. A consequence of the Hamiltonian operator is that the macroscopic ensemble of the nuclear spins precess

around the axis of the magnetic field B_0, at a resonant frequency determined by the gyromagnetic ratio of the nucleus, γ, defined as the Larmor frequency, $\omega_0 = \gamma B_0$.

The NMR signal in a pulsed NMR experiment is induced into the rf coil by the Lamor precession of the magnetization when RF irradiation is applied at the Larmor frequency, ω_0. If the simplest spin system is considered (I = 1/2), the two spin states, m_i = 1/2 and m_i = − 1/2 (m is the magnetic quantum number), have nearly equal populations, assuming Boltzmann distribution of spins. This results in only small observable differences for NMR signals; these differences in spin state populations are defined as polarization (P):

$$P = \frac{N_\uparrow - N_\downarrow}{N_\uparrow + N_\downarrow}, \qquad \text{[Eq. 1.3]}$$

where $N_\uparrow$ and $N_\downarrow$ are the number of spins in the m_i = 1/2 and m_i= − 1/2 spin states respectively. The fraction of nuclei that are in each spin state, N_i, is determined by the Boltzmann distribution:

$$N_i = \frac{e^{-m_i \gamma \hbar B_0 / k_b T}}{\sum_i e^{-m_i \gamma \hbar B_0 / k_b T}}, \qquad \text{[Eq. 1.4]}$$

where k_b is the Boltzmann constant, T is the temperature, and B_0 is the magnetic field strength. Applying Eq. 1.4 to Eq. 1.3 for an I = 1/2 spin system, polarization is redefined as:

$$P = \frac{e^{-\gamma \hbar B_0 / 2 k_b T} - e^{\gamma \hbar B_0 / 2 k_b T}}{e^{-\gamma \hbar B_0 / 2 k_b T} + e^{\gamma \hbar B_0 / 2 k_b T}}. \qquad \text{[Eq. 1.5]}$$

Under the conditions of thermal equilibrium (i.e. Boltzmann distribution of spins) and at high temperatures (i.e. $\gamma\hbar B_0/k_B T \ll 1$), Eq. 1.5 can be approximated by:

$$P \approx \frac{|\gamma|\hbar B_0}{2k_B T}. \qquad \text{[Eq. 1.6]}$$

The NMR observable magnitude of the magnetization, M_0, is proportional to P:

$$M_0 = \frac{1}{2} N_s \gamma \hbar P, \qquad \text{[Eq. 1.7]}$$

where N_s is the number of nuclear spins in the sample, and when combined with Eq. 1.6:

$$M_0 = \frac{N_s |\gamma|^2 \hbar^2 B_0}{4k_b T}. \qquad \text{[Eq. 1.8]}$$

It is evident from Eq. 1.8 that the observed magnetization will be a small value for all practical cases. Polarization for protons at 300 K in a 9.4 T magnetic field is only 3.3×10^{-5}. If a nucleus has a low natural abundance (i.e. <100%) or a low γ, then the already small magnetization becomes smaller. Although the variables of B_0 and T can be altered to increase the magnetization, certain experimental procedures restrict these values (i.e. *in vivo* cannot take place at 4 K). It is this low polarization that leads to the insensitivity associated with NMR and MRI. It is important to note that the derivations in this section are restricted to the I = 1/2 spin system. Defining polarization for spin systems where I > 1/2 (i.e. quadrupolar nuclei) is discussed further in chapter 4 of this dissertation.

1.2.2. Relaxation, spectral density, and correlation times

In the presence of a magnetic field, the spin magnetization (as defined in section 1.2.1) is aligned with the direction of the magnetic field, B_0. Detecting this magnetization involves applying an RF pulse at the Larmor frequency for a short period of time (typically on the order of milliseconds) to rotate the magnetization from longitudinal magnetization (M_z) to transverse magnetization ($M_{x,y}$). NMR detects the magnetization in the transverse plane although it is the longitudinal magnetization that determines the observable signal. Over a period of time, the magnetizations of M_z and $M_{x,y}$ will return to their original (i.e. equilibrium) conditions, considered in NMR to be relaxation processes. The equilibrium condition for M_z and $M_{x,y}$ is that magnetization is "stored" in M_z, and no magnetization is in $M_{x,y}$. The growth or restoration of magnetization along the z axis is called the T_1 relaxation process, while the decay of magnetization in $M_{x,y}$ after the application of the RF pulse is called the T_2 relaxation process. Whereas both of these processes occur in the time domain, it is important to note that both T_1 and T_2 do not describe the time for complete recovery or destruction of the associated magnetization. Complete, or quantitative, recovery/destruction is not considered to occur until at least five times the value of these constants has passed.

Mathematically, the relaxation process for transverse magnetization, T_2, can be described by a differential equation:

$$\frac{dM_{x,y}(t)}{dt} = \frac{-M_{x,y}(t)}{T_2} \quad . \qquad \text{[Eq. 1.9]}$$

Since no magnetization exists in $M_{x,y}$ at equilibrium, Eq. 1.9 can be solved as:

$$M_{x,y}(t) = M_{x,y}(0)e^{\left(-t/T_2\right)}, \qquad \text{[Eq. 1.10]}$$

where $M_{x,y}(0)$ is the magnetization in the transverse plane produced by the application of an RF pulse at time $t = 0$.

For traditional NMR, working with thermally polarized systems, the relaxation process for longitudinal magnetization, T_1, back to its equilibrium value can described by a differential equation:

$$\frac{dM_z(t)}{dt} \propto M_0 - M_z(t), \qquad \text{[Eq. 1.11]}$$

where M_0 is the equilibrium value of M_z (i.e. before RF is applied) and $M_z(t)$ is the present quantity of magnetization along the z axis at a particular time, t. With a proportionality constant, T_1, Eq. 1.11 can be rearranged:

$$\frac{dM_z(t)}{dt} = T_1\left(M_0 - M_z(t)\right). \qquad \text{[Eq. 1.12]}$$

After separating the variables, defining $M_z = 0$ at $t = 0$ (because there is no longitudinal magnetization immediately after the application of the RF pulse), and integrating from 0 $\rightarrow M_z$ and 0 $\rightarrow t$, the solution to Eq. 1.12 is:

$$\ln\left(\frac{M_0 - M_z}{M_0}\right) = -\frac{t}{T_1}, \qquad \text{[Eq. 1.13]}$$

which can be rearranged to:

$$M_z = M_0\left(1 - e^{-t/T_1}\right). \qquad \text{[Eq. 1.14]}$$

However, as stated above, Eq. 1.14 defines T_1 for a thermally polarized system. In a hyperpolarized system such as those produced by SEOP, the initial magnetization after SEOP is larger than the equilibrium polarization, which requires a substitution of $M_z(0)$ for M_0 in Eq. 1.15, resulting in:

$$M_z(t) \approx M_z(0)\left(1 - e^{-t/T_1}\right). \qquad \text{[Eq. 1.15]}$$

In 1948, Bloembergen, Purcell and Pound [42], laid the foundation for the quantum mechanical perspective of relaxation. From this foundation, relaxation is caused by fluctuations in the local magnetic environment. Fluctuations as small as the tumbling of a molecule, causing a change in its local dipolar field, are sufficient to induce transitions between energy levels and therefore cause relaxation. These fluctuations are found in the transverse magnetic field, $B_x(t)$, and for NMR experiments with liquids and gases, these fluctuations are considered to be rapid and random. It should be noted that an underlying assumption is that the difference in energy levels is small compared to k_bT (i.e. $\left(E_i - E_j\right)/k_bT \ll 1$) and that this assumption holds for nearly all NMR experiments. As the fluctuations are random and rapid, the average value of these fluctuations is considered to be zero, $\left\langle B_x(t)\right\rangle = 0$. However, it is the mean square fluctuations, $\left\langle B_x^2(t)\right\rangle \neq 0$, that are responsible for relaxation, not the average value of the fluctuations.

To define how rapidly these fluctuations occur in time, an autocorrelation function is introduced:

$$G(\tau) = \langle B_x(t) B_x(t+\tau) \rangle, \qquad \text{[Eq. 1.16]}$$

where τ is an increment of time, and by definition the autocorrelation function at $\tau = 0$ is equal to the mean square of the fluctuations, $G(0) = \langle B_x^2(t) \rangle$. For rapid fluctuations, the autocorrelation function decays quickly with respect to τ, whereas slow fluctuations decay slowly with respect to τ. In general, the autocorrelation function, $G(\tau)$, tends to be large for small τ values and small for large τ values. Therefore, assuming that $G(\tau)$ decays exponentially, Eq. 1.16 can be rewritten:

$$G(t) = \langle B_x^2 \rangle e^{-|\tau|/\tau_c}, \qquad \text{[Eq. 1.17]}$$

where τ_c is the correlation time of the fluctuations. Applying a Fourier transform to the autocorrelation function, the spectral density $\boldsymbol{J}(\omega)$ at a given frequency, ω, can be obtained:

$$\boldsymbol{J}(\omega) = \int_{-\infty}^{\infty} G(t) e^{(-i\omega\tau)} d\tau = 2 \langle B_x^2 \rangle \frac{\tau_c}{1+\omega^2\tau_c^2}. \qquad \text{[Eq. 1.18]}$$

It is common to work with the normalized spectral density, $J(\omega)$:

$$J(\omega) = \frac{\tau_c}{1+\omega^2\tau_c^2}, \qquad \text{[Eq. 1.19]}$$

instead of the complete expression $\boldsymbol{J}(\omega)$. Fig. 1.1 shows $J(\omega)$ versus the logarithm of ω for three different τ_c values. For any τ_c in Fig. 1.1, assuming the condition $\tau_c \ll 1/\omega_0$, referred to as the extreme narrowing condition, a region with nearly zero slope is found. When $\tau_c \ll 1/\omega_0$, Eq. 1.19 reduces to $J(\omega) \approx \tau_c$. However as $\log(\omega)$ increases, eventually

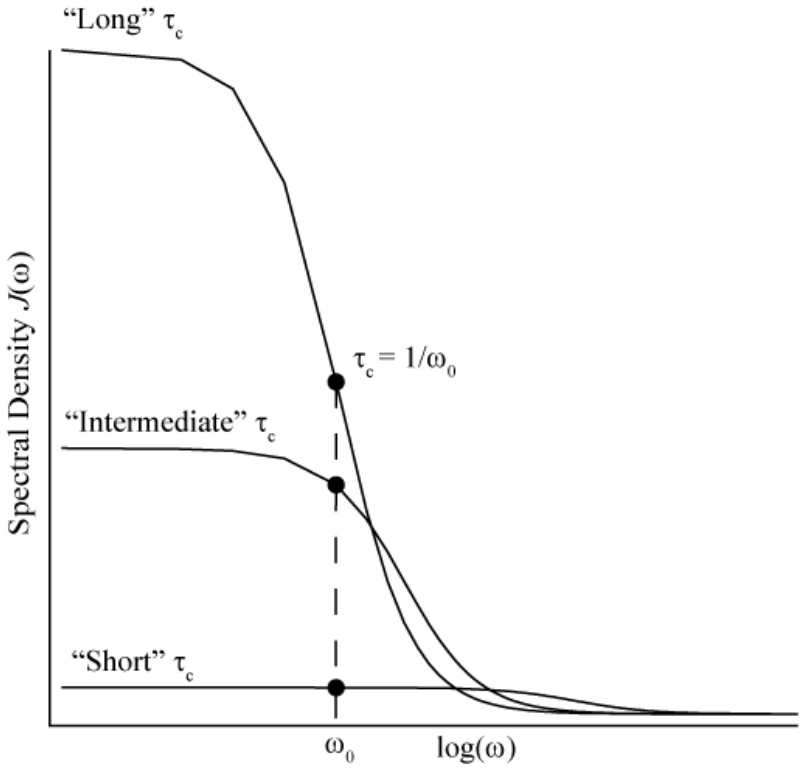

Fig. 1.1: Spectral density, $J(\omega)$, as a function of the log of the frequency. Three different correlation times, τ_c, are displayed to demonstrate the differences in behavior as τ_c becomes longer. For all three curves, an arbitrary larmor frequency, ω_0, has been marked as a reference. For the curve marked "Long" τ_c, the τ_c is equal to the inverse of the larmor frequency and any change in the log(ω) will result in changes in $J(\omega)$. For "Short" τ_c, the graph displays no significant change in $J(\omega)$ around ω_0. This is the extreme narrowing condition where $\tau_c << 1/\omega_0$, demonstrating field independent nature in the spectral density.

the extreme narrowing condition is violated (i.e. $\tau_c \approx 1/\omega_0$), $J(\omega)$ is governed by the complete Eq. 1.19 and a change in slope occurs in Fig. 1.1. It is around this value $\tau_c \approx 1/\omega_0$ that $J(\omega)$ has a dependence on magnetic field strength from $\omega = \omega_0 = \gamma B_0$. As τ_c becomes shorter, the log(ω) value needed to violate the extreme narrowing conditions increases. Therefore nuclei with short τ_c values may not experience any field dependence of $J(\omega)$ even at high magnetic field strengths. This field dependence is discussed along with experimental observations of relaxation times in chapter 5. Depending on the nature of the interaction responsible for relaxation, the functional dependence of the longitudinal relaxation on $J(\omega)$ will be different. Below are three cases for different relaxation: (1) Magnetic dipole-dipole interaction where relaxation is due to "through-space" interaction of magnetic moments of other nuclei, assuming a homonuclear sample:

$$\frac{1}{T_1^{DD-L}} = \frac{2}{5}\gamma^4\hbar^2 I(I+1)\sum_i r_i^{-6}\left(\frac{1}{1+\omega_0^2\tau_c^2}+\frac{1}{1+4\omega_0^2\tau_c^2}\right)\tau_c . \qquad \text{[Eq. 1.20]}$$

(2) Chemical shift anisotropy where relaxation is related to the variability of the chemical shift as a function of molecular/atomic orientation with respect to the magnetic field:

$$\frac{1}{T_1} = \frac{2}{15}\gamma^2 B_0^2\left(\sigma_{\parallel}-\sigma_{\perp}\right)\frac{\tau_c}{1+\omega_0^2\tau_c^2}, \qquad \text{[Eq. 1.21]}$$

where $\left(\sigma_{\parallel}-\sigma_{\perp}\right)$ describes the shielding anisotropy. (3) Quadrupolar interactions, which are studied extensively in later chapters of this dissertation, where relaxation is due to changes in the EFG coupled to the quadrupole moment:

$$\frac{1}{T_1} = \frac{3}{10}\left(1+\frac{\eta^2}{3}\right)\left(\frac{2I+3}{I^2(2I-1)}\right)\left(\frac{eqQ}{\hbar}\right)^2\left(\frac{2\tau_c}{1+\omega_0^2\tau_c^2}\right), \qquad \text{[Eq. 1.22]}$$

where $(eqQ/\hbar)$ is the quadrupole coupling constant and η is the asymmetry parameter of the quadrupolar nucleus. η is defined as:

$$\eta = \frac{(q_{yy} - q_{xx})}{q_{zz}}, \qquad \text{[Eq. 1.23]}$$

with the axes chosen to be $|q_{zz}| \geq |q_{xx}| \geq |q_{yy}|$ such that η is between zero and one. The longitudinal relaxation has a strong dependence on τ_c for all three of the cases presented above. In most cases, τ_c is small (i.e. $\omega_0\tau_c \ll 1$), reducing the longitudinal relaxation equations to $1/T_1 \propto \tau_c$, a consequence of the extreme narrowing condition mentioned above. Fig. 1.2 shows the behavior of T_1 as a function of τ_c at four different field strengths (0.5, 1, 2, 3 T). For all cases presented in Fig. 1.2, the fastest relaxation time occurs at $\tau_c \approx 1/\omega_0$. Fig. 1.2 illustrates how for a particular τ_c, it is possible to obtain different T_1 values by changing the field strength.

1.2.3. Magnetic resonance imaging and contrast

In NMR spectroscopy, highly homogenous magnetic fields are used to obtain narrow linewidths. In this case, the Larmor frequency is $\omega_0 = \gamma B_0$. When the homogeneity of the magnetic field is disrupted intentionally, the Larmor frequency becomes a function of position within the applied gradient:

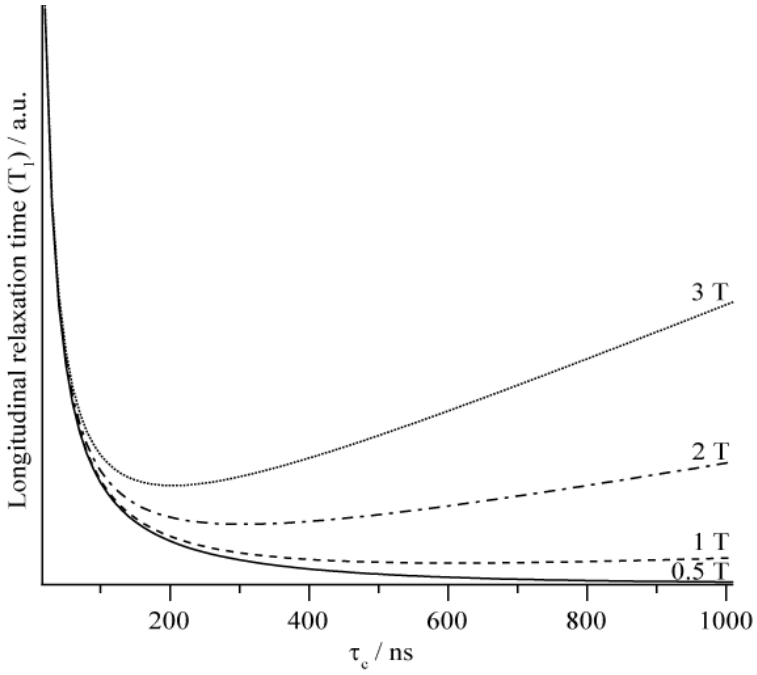

Fig. 1.2: Longitudinal relaxation time (T_1) of ^{83}Kr as a function of correlation time (τ_c) at four different field strengths. To calculate each T_1 curve, no specific relaxation mechanism was considered (therefore arbitrary units); it was assumed that relaxation took place in a homogenous magnetic field and ω_0 for each field strength is: 0.5 T: 0.82 MHz; 1 T: 1.64 MHz; 2 T: 3.27 MHz; and 3 T: 4.91 MHz. Each T_1 curve decreases with increasing τ_c until reaching the minimum value of $\tau_c = 1/\omega_0$, after which the T_1 values begins increasing.

$$\omega(r) = \gamma B_0 + \gamma G \bullet r \qquad \text{[Eq. 1.24]}$$

where G is the magnetic field gradient applied along a single axis, and r details the spatial coordinates for the observed nuclear spin. In the presence of a single linear gradient, a 1D image of the spin density in the sample is acquired, compared to a 1D spectrum that would be collected in a homogenous field under identical RF conditions. Using projection reconstruction methods, it is possible to acquire many 1D images at various angles and orientations of a sample to construct 2D and 3D images [43]. A second method for acquiring multi dimensional images is phase encoding, where a gradient is applied to the nuclear spins such that a location specific phase modulation is placed on the MR signal. In comparison to projection reconstruction, phase encoding allows for faster imaging as it can be applied to more than one gradient at a time [44].

Whereas MRI requires sufficient signal intensity to resolve areas of interest, the absence or the decay of signal (from relaxation) is also a useful tool in understanding the surroundings of the observed nuclei. MRI contrast depends on a difference in signal intensity caused by longitudinal (T_1) [45] or transverse (T_2) [46] relaxation or chemical shift differences [47; 48] between distinct areas (i.e. healthy versus cancerous tissue [49]). Therefore contrast provides a method for MRI where the absence of signal (or conversely increased signal) can provide information about specific regions of interest.

1.3. Spin exchange optical pumping with alkali metal vapor

1.3.1. Generation of polarization in the alkali metal

The first step in achieving high nuclear polarization in noble gas nuclei is to create high electronic polarization in an alkali metal, typically rubidium (Rb). The necessary electronic transitions for producing the high electronic polarization are displayed in Fig. 1.3. Typically, SEOP takes place in a glass cell containing the alkali metal with an appropriate gas mixture (this is detailed further in 1.3.3) at moderate temperatures (> 373 K) and in the presence of a magnetic field (in excess of 10 G) aligned with the laser. With the magnetic field aligned with the cell (defined as the z axis) the Hamiltonian for the alkali metal atom in the ground state is [4]:

$$H_a = A_a I_a \cdot S + g_s \mu_B S_z B_0 - \frac{\mu_a}{I_a} I_{az} B_0 . \qquad \text{[Eq. 1.25]}$$

The first term in Eq. 1.25, $A_a I_a \cdot S$, is the hyperfine interaction where A_a is the isotropic magnetic dipole coupling coefficient, I_a is the alkali metal nuclear spin, and S is the valence electron spin. The remainder of Eq. 1.25 describes the Zeeman interactions of the electronic and nuclear spins with an applied magnetic field strength, B_0. In the low magnetic fields used for SEOP, the Zeeman interactions can be ignored.

With the application of circularly polarized light (σ^+ or σ^-) resonant with the D1 transition of the alkali metal (794.7 nm for Rb), the conservation of angular momentum requires a selection rule of $\Delta m = 1$ (for σ^+) or $\Delta m = -1$ (for σ^-). The valence electron of the alkali metal can therefore be pumped from the $^2S_{1/2}$ ground state to the $^2P_{1/2}$ excited state. Fig. 1.3 shows the selection process using σ^- circularly polarized light: valence electrons in the spin-up (m_s = 1/2) sublevel of the ground state are excited into the spin-down ($m_j = -1/2$) sublevel of the excited state. At the pressures typical in an SEOP cell,

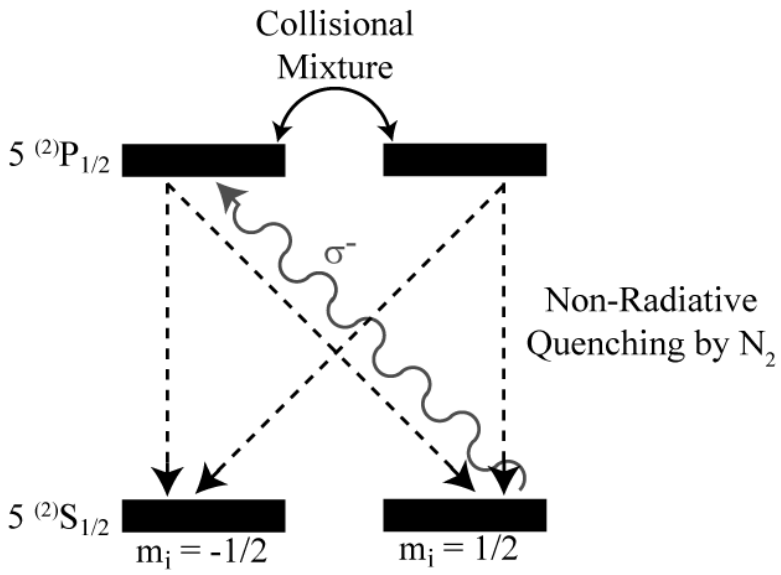

Fig. 1.3: Diagram of electronic transitions taking place in alkali metal Rb to produce non-equilibrium electronic polarization. The Zeeman splitting of the electronic sublevels is exaggerated in this illustration. Hyperfine splitting is neglected and under the experimental conditions (i.e. pressure broadening) used for SEOP would be unresolved. The alkali metal valence electron from the spin-up sublevel of the $^2S_{1/2}$ ground state (m_s = 1/2) is excited by circularly polarized (σ^-) light to the spin-down sublevel of the $^2P_{1/2}$ (m_j = − 1/2) by the $\Delta m = 1$ selection rule. Collisional mixing equalizes the populations of the $^2P_{1/2}$ sublevels and collisions of the excited alkali metal atom with diatomic N_2 allows for non-radiatively quenching of the electronic excited states down to their respective $^2S_{1/2}$ sublevels. While both excited state sublevels will be quenched with equal probability, electrons returning to the spin-up sublevel of the $^2S_{1/2}$ ground state would be re-excited leading to an eventual depletion of the m_s = − 1/2 sublevel population and building a non-equilibrium population in the m_s = 1/2 sublevel.

gas phase collisions will rapidly mix the $^2P_{1/2}$ sublevel populations, equalizing the spin polarization of the excited-state produced by photon adsorption. After collisional mixing, the excited states transition back to the ground state by either a radiative or a radiatively quenched process. This relaxation repopulates the sublevels equally; however, as circularly polarized light is always present during the SEOP process, any valence electrons that decay into the sublevel being pumped (m_s = 1/2 for the case presented in Fig. 1.3) will be re-excited into the $^2P_{1/2}$ states. This causes a depletion of the population for the sublevel being pumped and an increase in population for the sublevel that cannot be excited under the circularly polarized conditions. Approximately 100% polarization of the alkali metal atoms is possible under ideal experimental conditions [50].

1.3.2. Transfer of polarization to noble gas nuclei

After the production of electronically polarized alkali metal, the next step in the SEOP process is to transfer the polarization from the valence electron of alkali metal to the nucleus of the noble gas. This occurs by two different processes, either binary collisions or van der Waals complexes, shown in Fig. 1.4. For the low atomic number noble gas nuclei, in particular ^{3}He, binary collisions are the dominant mechanism for polarization transfer. For larger atomic number noble gas nuclei, such as ^{129}Xe, van der Waals complexes are the main polarization mechanism. The theory behind polarization transfer from the alkali metal valence electron to the nucleus of a noble gas atoms is detailed in [3] by Happer *et al.* From [3], the simplest Hamiltonian to describe the spin transfer and relaxation in alkali metal vapor and noble gas mixtures is:

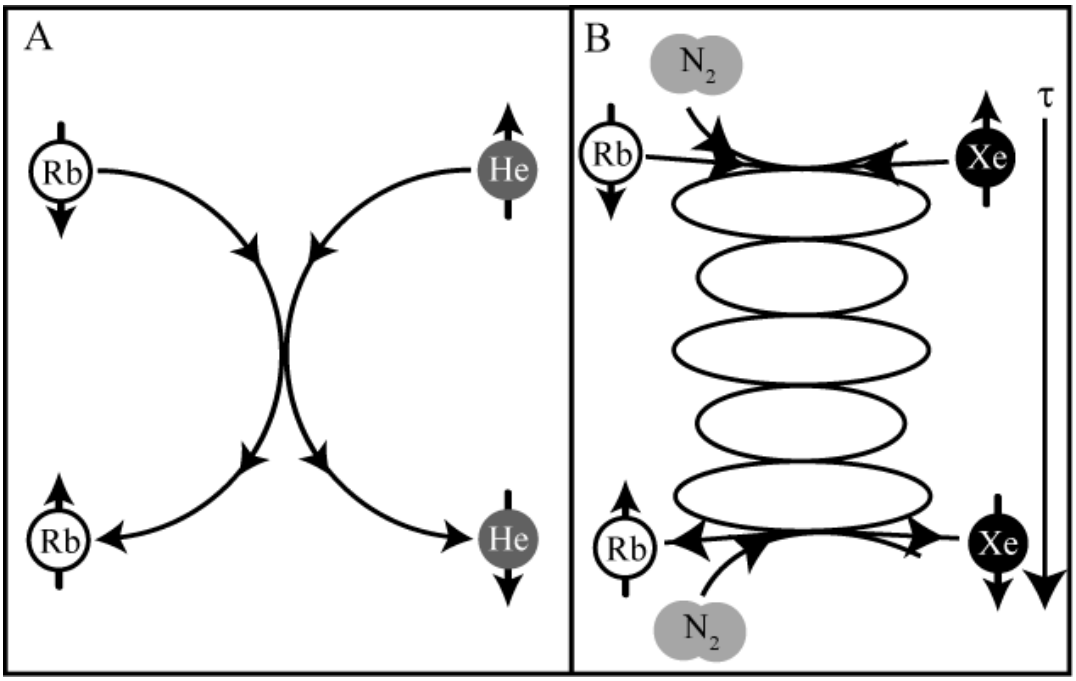

Fig. 1.4: The two spin exchange mechanisms. A: Binary collisions. Binary collisions are brief interactions between alkali metal and noble gas atoms. During this collision, Fermi contact between the valence electron of the alkali metal atom interacts with the nucleus of the noble gas atom. Spin flip transition can occur during Fermi contact where the alkali metal valence electron is depolarized and the noble gas nucleus is polarized. B: van der Waals complex. A van der Waals complex is the result of a three-body collision between an alkali metal atom, a noble gas atom (displayed here as Xe), and a third body (displayed here as N_2). The third body transfers translational energy away from the alkali metal–noble gas pair producing a sticking collision. The newly formed van der Waals pair remains bound for some lifetime, τ. During this lifetime, polarization can be transferred between the valence electron of the alkali metal to the nucleus of the noble gas by Fermi contact. The van der Waals pair is broken by a subsequent collision.

$$H = AI \bullet S + \gamma N \bullet S + \alpha K \bullet S + \ldots, \qquad \text{[Eq. 1.26]}$$

where $AI \bullet S$ is the hyperfine interaction between the alkali metal valence electron spin, *S*, and the alkali metal nuclear spin, *I*; $\gamma N \bullet S$ describes the spin-rotation interaction between the rotational angular moment, *N*, of the alkali metal-noble gas pair and *S*; $\alpha K \bullet S$ is the Fermi contact between *S* and the nuclear spin of the noble gas, *K*. From Eq. 1.26, the primary interest is in the Fermi contact term, $\alpha K \bullet S$, which is responsible for producing the non-equilibrium nuclear spin polarization.

The Fermi contact term contains two components, α and $K \bullet S$. α is the magnetic dipole coupling constant derived by [51]. The necessary part of α for consideration of transferring polarization is the Dirac delta function, $\delta(R)$. $\delta(R)$ is a three-dimensional delta function corresponding to the location of the alkali metal valence electron compared to the nucleus of the noble gas atom. $\delta(R)$ is equal to one when the alkali metal valence electron is at the noble gas nucleus and zero everywhere else. $K \bullet S$ can be rewritten using ladder operator formalism:

$$K \bullet S = \hat{K}_z \hat{S}_z + \frac{1}{2}\left(\hat{K}^+ \hat{S}^- + \hat{K}^- \hat{S}^+\right), \qquad \text{[Eq. 1.27]}$$

where the operators $\hat{K}^+ \hat{S}^-$ and $\hat{K}^- \hat{S}^+$ transfer angular momentum between the valence electron of the alkali metal and the nucleus of the noble gas. However, it was shown in ^{129}Xe [52] that the dominant relaxation mechanism for polarized Rb is not the transfer of polarization to the noble gas, it is the spin-rotation interaction $\gamma N \bullet S$. Happer and coworkers [3; 53] have shown that for each unit of angular momentum lost by the

collision of a Rb atom with a ^{129}Xe atom, ~ 10% of those collisions will result in angular momentum transfer (i.e. polarization) to the ^{129}Xe nucleus.

To consider polarization transfer from an alkali metal valence electron to the nucleus of a noble gas atom, the buildup of polarization in the alkali metal must first be established. These calculations are shown for Rb because it is the most commonly used alkali metal in SEOP and is also used in this dissertation. Rb polarization is treated as a function of position along the z-axis of the SEOP cell, given by P_{Rb}(z) [54]:

$$P_{Rb}(z) = \frac{\gamma_{op}(z)}{\gamma_{op}(z) + \gamma_{sd}}, \qquad \text{[Eq. 1.28]}$$

where γ_{op}(z) is the optical pumping rate per Rb atom at position z, and γ_{sd} is the Rb spin destruction rate expressed as:

$$\gamma_{sd} = \sum_i \kappa_{sd}^i [M_i], \qquad \text{[Eq. 1.29]}$$

where κ_{sd}^i is the spin destruction rate coefficient for a given gas mixture component, and $[M_i]$ is the number density for that component. Note that because the intensity of the circularly polarized light will weaken through the pump cell (i.e. optically thick beam path), the value of γ_{op}(z) is expected to change along the z axis. Nuclear polarization in the noble gas atoms can be defined as a function of time (t_p) [55]:

$$P_{Ng}(t_p) = \frac{\gamma_{se}}{\gamma_{se} + |\Gamma|} \cdot \frac{\gamma_{op}(z)}{\gamma_{op}(z) + \sum_i \kappa_{sd}^i [M_i]} \left(1 - e^{-(\gamma_{se}+\Gamma)t_p}\right), \qquad \text{[Eq. 1.30]}$$

where γ_{se} is the spin exchange rate and Γ is the rate of self relaxation of the noble gas nuclei originating from collisions with SEOP cell walls or other noble gas atoms. During optical pumping γ_{se} is positive (i.e. generating polarization) in value and Γ is negative as polarization in the noble gas nuclei is increasing faster than relaxation can destroy it. The spin exchange rate, γ_{se}, which governs the polarization transfer between Rb and the noble gas nucleus, is defined as [3; 56]:

$$\gamma_{se} = [Rb]\left(\frac{\gamma_{RbNg}\xi_{Rb}}{[N_g] + \sum_i b_i [M_i]} + \langle \sigma v \rangle\right), \qquad \text{[Eq. 1.31]}$$

where [Rb] is the number density of rubidium (found experimentally by [57]), γ_{RbNg} is the rate contribution from van der Waals complexes to spin exchange via Fermi contact, ζ_{Rb} is the isotropic composition of Rb [56], [N_g] is the number density of the noble gas, and $\langle \sigma \upsilon \rangle$ is the velocity averaged binary spin exchange cross-section.

In studies that utilize hp noble gases for NMR and MRI, the hp noble gas is typically separated from the SEOP cell to be studied. Under this premise, $\gamma_{op}(z)$ is difficult to quantify and can be simplified to γ_{op}, an average of the optical pumping rate over the entire SEOP cell. Additionally, the value of κ_{sd}^{Xe}, ~5.2×10^{-15} cm^3s^{-1} [50; 55] is orders of magnitude larger than the values obtained for κ_{sd}^{He}, ~2×10^{-18} cm^3s^{-1}, and $\kappa_{sd}^{N_2}$, ~9×10^{-18} cm^3s^{-1} [50]. Therefore when considering ^{129}Xe for SEOP, the spin destruction values from other gas mixture components can be disregarded. A final simplification comes for ^3He and ^{129}Xe, where the $\Gamma << \gamma_{se}$ for these nuclei, so Γ can be disregarded. In the case of hp ^{129}Xe production, Eq. 1.30 reduces to:

$$P_{^{129}Xe}\left(t_p\right) = \frac{\gamma_{op}}{\gamma_{op} + \kappa_{sd}^{Xe}\left[Xe\right]}\left(1 - e^{-\gamma_{se} t_p}\right). \qquad \text{[Eq. 1.32]}$$

Where only κ_{sd} for ^{129}Xe is considered since all other gas present can be excluded. However this is not the case for ^{3}He SEOP. Additionally, for spin $I > 1/2$ isotopes, relaxation is much faster than that of ^{129}Xe, therefore Γ cannot be disregarded. At high densities of the noble gas atoms, relaxation will accelerate, leading to higher values of Γ. Eq. 1.30, Eq. 1.31, and Eq. 1.32 are all dependent on the density of the noble gas: as the noble gas density increases, the spin exchange rate will decrease (Eq. 1. 31) and the noble gas polarization will decrease due to higher spin destruction (general form: Eq. 1. 30, ^{129}Xe specific: Eq. 1.32).

1.3.3. Considerations and improvements for spin exchange optical pumping

During the SEOP process, when the alkali metal atoms are in the excited state, the relaxation pathway of the alkali metal atoms back to the ground state can be radiative. The consequence of the radiative relaxation is that both transitions, $\Delta m_j = +1$ and $\Delta m_j = -1$, have an equal probability of occurring, which results in the emission of unpolarized light. This emission can be a significant depolarization source because unpolarized light will pump both sublevels of the ground state, thus destroying the built up non-equilibrium polarization. This is countered by the addition of a diatomic molecule (typically N_2) to the SEOP gas mixture, which allows the energy of the excitation to be transferred into excited rotational and vibrational modes of the diatomic molecule [58].

In most SEOP experiments involving NMR and MRI, solid-state diode array lasers provide cell illumination. These laser sources provide high power output at low cost; however, they have broad line widths (~2 nm) which are not fully absorbed by the narrow D1 transition of the Rb vapor. To improve absorption of the light, helium is added to the gas mixture (for ^{129}Xe SEOP, $\geq$ 90 % He is typical) to pressure broaden the Rb absorption line [55] with minimal depolarization of the Rb. In addition to pressure broadening, it is now commercially feasible to produce line-narrowing devices that improve the absorption of light and efficiently couple the laser power to the Rb absorption line [59; 60; 61; 62]. These devices can be fitted externally to broad lasers [59; 60], or internally allowing for fiber coupled, line narrowed laser systems [61; 62]. Both types of laser systems, broad and internally narrowed, have been employed throughout this dissertation.

When illuminating the SEOP cell, it is important to ensure that circularly polarized light is penetrating the full length and width of the cell. Illumination of the volume of the SEOP cell near the walls of the cell is of particular importance as the relaxation on the wall surface is one of the fastest relaxation sources for both polarized alkali metal and noble gas nuclei. Regions of the SEOP cell that are not illuminated by circularly polarized light (i.e. dark regions) contain alkali metal atoms that are not polarized. A collision between an unpolarized (i.e. “dark”) alkali metal and a polarized noble gas poses a significant problem as the dark alkali metal will quickly relax any hyperpolarized noble gas atom with which it collides. This is in contrast to the collision between a polarized (i.e. “light”) alkali metal and a polarized noble gas atom, which is unlikely to cause significant nuclear relaxation.

Gas mixtures with low percentages of noble gas atoms have provided the highest polarizations thus far (^{129}Xe: see refs. [10; 63; 64], ^{83}Kr: see ref. [65] and chapter 6); these quantities are not typically concentrated enough for the intended studies (i.e. *in vivo*). Currently, cryogenic accumulation is used to concentrate hp ^{129}Xe. To achieve this, slow flowing gas passes through the SEOP cell achieving hyperpolarization. Upon exiting the SEOP cell, the gas flows into a liquid nitrogen cold finger contained in a magnetic field (in excess of 500 G) [55; 66]. This allows for the hp ^{129}Xe to freeze out of the gas mixture and for the other components (N_2, He) to be removed as they do not freeze out at these temperatures. Under these conditions, the longitudinal relaxation time of ^{129}Xe in the solid state exceeds 2 hours [67]. This process results in the accumulation of pure xenon with only minor relaxation occurring. When the solid xenon is rapidly heated, it returns to the gas phase with high polarization. Unfortunately, hp ^{83}Kr and ^{131}Xe cannot make use of cryogenic accumulation at liquid nitrogen temperatures due to short longitudinal relaxation times (^{83}Kr: ~10 s; ^{131}Xe: ~1 s) [68; 69; 70].

1.4. Previous work with quadrupolar nuclei: ^{83}Kr and ^{131}Xe

1.4.1 Hyperpolarized and thermally polarized ^{83}Kr

Since its first experimental observation [52; 71], hp ^{83}Kr has not been used as widely as hp ^{3}He and hp ^{129}Xe. ^{83}Kr suffers several setbacks when compared to ^{129}Xe: a lower gyromagnetic ratio ($\gamma_{^{83}Kr}/\gamma_{^{129}Xe} \approx 0.14$), faster relaxation from quadrupolar interactions, lower natural abundance (~44% abundant as ^{129}Xe), and a smaller chemical shift range due to its smaller electron cloud and due to the lower gyromagnetic ratio [72]. Until recently [45], hp ^{83}Kr was limited to studies inside of the SEOP cell. Without

separation from the highly reactive alkali metal, hp ^{83}Kr research was limited. Studies included determining spin-parameters [73] and understanding the spin exchange process [6] in the SEOP cell. The behavior of ^{83}Kr transverse relaxation and frequency shifts as a function of SEOP cell temperature and geometry were also investigated [74; 75]. The small ^{83}Kr-Rb spin exchange cross section requires SEOP cells to operate at higher temperatures, which increase the density of Rb in the vapor phase making the penetration of the cell by light difficult. As many of the initial experiments used a pump-probe setup to detect magnetization changes in the Rb or ^{83}Kr [52; 71; 74], increasing the temperatures of the SEOP cell was a limiting factor due to limitations in light sources.

High power diode array lasers provide adequate optical penetration of the SEOP cell even at increased temperatures, so that hp ^{83}Kr can be polarized and separated from the Rb vapor in both continuous flow [45; 65] and stopped flow style [45; 65; 76; 77; 78; 79; 80; 81] setups. Cleveland *et al.* [65] demonstrated that continuous flow was possible with hp ^{83}Kr, resulting in enhancement factors of 27 times that of thermal signal. In contrast, in stopped flow SEOP, enhancement factors of 1200 times that of thermal signal were achievable. The quadrupolar relaxation of ^{83}Kr has been shown in many cases to be surface sensitive [65; 76; 77; 78]. T_1 times for ^{83}Kr were found to be sensitive to changes in surface chemistry and surface-to-volume ratio for ideally packed glass beads [76]. In soda lime glass capillaries, ^{83}Kr T_1 sensitivity to the deposition of tobacco smoke provided sufficient differences for MRI contrast [78]. Additionally, both the ^{83}Kr T_1 temperature dependence [65] and the ^{83}Kr T_1 relaxation behavior in the presence of co-adsorbing species on surfaces have been observed [77]. Hp ^{83}Kr has been used in MRI of biological systems as well. Initial MRI studies took place in desiccated lung tissue [45],

and later MR images of *ex vivo* rat lungs were obtained [79]; the initial report of T_1 times ranged from 0.6 – 3.7 s in lung tissue. Longitudinal relaxation mechanisms for ^{83}Kr in gas phase binary collisions [80] as well as relaxation induced by Kr-Kr dimers [81] has been reported.

^{83}Kr studies are not limited to hyperpolarized systems. Investigations date back almost 50 years to the fundamental work exploring ^{83}Kr chemical shift and longitudinal relaxation in solids, liquids and at high gas pressures [82]. Detailed studies by Norberg and coworkers [68; 83; 84; 85] provide useful insight into the behavior of ^{83}Kr in the solid and liquid state. Cowgill and Norberg outlined the relaxation behavior for ^{83}Kr in the solid and liquid phase [68]; at liquid nitrogen temperatures, T_1 for ^{83}Kr was ~8 s, and the shortest T_1 reported was ~0.6 s, near the triple point of krypton (115.8 K). In the presence of oxygen, T_1 was reduced by a maximum of 20%. This limited reduction is explored further in chapters 5 and 6, as the insensitivity of ^{83}Kr to paramagnetic oxygen can be utilized for surface sensitive contrast for *in vivo* systems.

^{83}Kr NMR spectroscopy has been carried out in a number of systems where krypton is dissolved into liquids or loaded into guest-host structures (i.e. zeolites). Mazitov *et al.* [72] presented an extensive study of the chemical shift and relaxation of ^{83}Kr in polar and non-polar solvent systems, and as a function of temperature. Studies of krypton dissolved in nematic liquid crystals [86; 87; 88] showed a series of peaks that corresponded to the number of energy transitions in ^{83}Kr spin states. These peaks in the ^{83}Kr NMR spectrum were observed due to interactions of the nuclear quadrupole moment with the net alignment of the liquid crystal anisotropy, allowing for the direct observation of quadrupolar effects by the associated peak splitting. In zeolite structures, the line

shape of ^{83}Kr, directly observed by NMR [89], was sensitive to pore dimensions, pore geometry, and counter-cation charge. These direct observations in zeolites were possible because ^{83}Kr in the porous material has a T_1 of a few milliseconds, allowing for rapid signal averaging to acquire reasonable signal-to-noise.

1.4.2. ^{131}Xe NMR in thermally and hyperpolarized systems

^{131}Xe, with a spin I = 3/2, possesses a nuclear electric quadrupole moment that is susceptible to interactions with EFGs. EFGs are caused during events such as adsorption onto surfaces, which distort the spherical shape of the large electron cloud. The quadrupolar interactions dominate ^{131}Xe longitudinal relaxation in all phases and cause ^{131}Xe relaxation to be significantly faster than ^{129}Xe. Extrapolating from experimental work by Brinkmann *et al.* [90], a T_1 of ~25 s for ^{131}Xe in pure xenon gas at atmospheric pressure is expected. This is substantially shorter than the T_1 of ^{129}Xe, which is expected to be on the order of 2 hours [12]. In the solid phase, ^{131}Xe does not show the sensitivity to oxygen that ^{129}Xe displays, as the ^{131}Xe T_1 is reduced by a maximum of 20% [69]. This reduction is nearly identical to the reduction seen in ^{83}Kr under similar conditions [68], which indicates that this phenomena of insensitive to paramagnetic species is general for quadrupolar nuclei. Warren and Norberg [69] reported a detailed survey of ^{131}Xe relaxation as a function of temperature ranging from 9 to 250 K (covering the solid and liquid phases): the T_1 of ^{131}Xe was 200 ms at the melting point (161 K) and 390 s at 9 K. The T_1 of one hour for ^{131}Xe at 4 K was reported although instability in the temperature control leaves this measurement as a first approximation.

^{131}Xe has been studied in a number of dissolved systems, in polar and non-polar solvents (review: [91]), and in liquid crystalline phases (review: [92]). ^{131}Xe has also been used near the supercritical point (289 K, 6 MPa) for MRI to provide contrast that is sensitive to the adsorption of water on aerogel surfaces [46]. The NMR spectrum of ^{131}Xe dissolved into liquid crystalline phases [86] contains a triplet of peaks attributed to interactions of the nuclear quadrupole moment with the net alignment of the liquid crystal anisotropy. This quadrupolar splitting has been further observed in the gas phase where anisotropy is provided by the walls of the NMR tube, and the quadrupolar splitting is found to be dependent on the magnetic field strength [93]. Two theoretical treatments for the dependence of the quadrupolar splitting of ^{131}Xe on magnetic field strength exist [94; 95], although there is disagreement on the functional form of the dependence. The observation of quadrupolar splitting in the gas phase is unique to ^{131}Xe and has not been observed in the gas phase for either of the other quadrupolar noble gas nuclei to date.

Hp ^{131}Xe has been produced by SEOP and studied with optically detected NMR (OD-NMR) inside of the SEOP cell. The spin exchange cross section for ^{131}Xe with rubidium was determined [8] and a study of relaxation caused by adsorption on the SEOP cell walls was reported [96]. In the SEOP cell, quadrupolar splitting of ^{131}Xe on the order of one Hz has been observed [97; 98; 99; 100; 101] with dependences on cell dimensions [97; 98; 99; 100; 101], orientation in the magnetic field [98], chemical treatment of SEOP cell wells [100], and temperature [101]. Luo *et al.* explored ^{129}Xe and ^{131}Xe SEOP using caesium in a high magnetic field (11.7 T) [102]. Additionally, Donley *et al.* used SEOP to explore the nuclear quadrupole resonance (NQR) of 131Xe in the transformation of NQR spectra from the NQR to the NMR regime [103].

References:

[1] A. Kastler, Quelques Suggestions Concernant la Production Optique et la Detection Optique Dune Inelalite de Population des Niveaux de Quantification Spatiale des Atomes - Application a Lexperience de Stern et Gerlach et a la Resonance Magnetique. Journal De Physique Et Le Radium 11 (1950) 255-265.

[2] M.A. Bouchiat, T.R. Carver, and C.M. Varnum, Nuclear Polarization in He-3 Gas Induced by Optical Pumping and Dipolar Exchange. Physical Review Letters 5 (1960) 373-375.

[3] W. Happer, E. Miron, S. Schaefer, D. Schreiber, W.a. Vanwijngaarden, and X. Zeng, Polarization of the Nuclear Spins of Noble-Gas Atoms by Spin Exchange with Optically Pumped Alkali-Metal Atoms. Physical Review A 29 (1984) 3092-3110.

[4] T.G. Walker, and W. Happer, Spin-exchange optical pumping of noble-gas nuclei. Review of Modern Physics 69 (1997) 629-642.

[5] T.E. Chupp, and K.P. Coulter, Polarization of Ne-21 by Spin Exchange with Optically Pumped Rb Vapor. Physical Review Letters 55 (1985) 1074-1077.

[6] S.R. Schaefer, G.D. Cates, and W. Happer, Determination of Spin-Exchange Parameters between Optically Pumped Rubidium and Kr-83. Physical Review A 41 (1990) 6063-6070.

[7] C.H. Volk, T.M. Kwon, and J.G. Mark, Measurement of the Rb-87-Xe-129 Spin-Exchange Cross-Section. Physical Review A 21 (1980) 1549-1555.

[8] C.H. Volk, T.M. Kwon, J.G. Mark, Y.B. Kim, and J.C. Woo, Measurement of the Rb-Xe-131 Spin-Exchange Cross-Section in Xe-131 Relaxation Studies. Physical Review Letters 44 (1980) 136-139.

[9] E. Babcock, B. Chann, T.G. Walker, W.C. Chen, and T.R. Gentile, Limits to the polarization for spin-exchange optical pumping of He-3. Physical Review Letters 96 (2006) 083003.

[10] K. Knagge, J. Prange, and D. Raftery, A continuously recirculating optical pumping apparatus for high xenon polarization and surface NMR studies. Chemical Physics Letters 397 (2004) 11-16.

[11] R.K. Harris, Nuclear Magnteic Resonance Spectroscopy, Pitman, London, 1983.

[12] M.S. Albert, G.D. Cates, B. Driehuys, W. Happer, B. Saam, C.S. Springer, and A. Wishnia, Biological Magnetic-Resonance-Imaging Using Laser Polarized Xe-129. Nature 370 (1994) 199-201.

[13] H. Middleton, R.D. Black, B. Saam, G.D. Cates, G.P. Cofer, R. Guenther, W. Happer, L.W. Hedlund, G.A. Johnson, K. Juvan, and J. Swartz, Mr-Imaging with Hyperpolarized He-3 Gas. Magnetic Resonance in Medicine 33 (1995) 271-275.

[14] B. Saam, D.A. Yablonskiy, D.S. Gierada, and M.S. Conradi, Rapid imaging of hyperpolarized gas using EPI. Magnetic Resonance in Medicine 42 (1999) 507-514.

[15] J.C. Woods, C.K. Choong, D.A. Yablonskiy, J. Bentley, J. Wong, J.A. Pierce, J.D. Cooper, P.T. Macklem, M.S. Conradi, and J.C. Hogg, Hyperpolarized He-3 diffusion MRI and histology in pulmonary emphysema. Magnetic Resonance in Medicine 56 (2006) 1293-1300.

[16] T.A. Altes, J. Mata, E.E. de Lange, J.R. Brookeman, and J.P. Mugler, Assessment of lung development using hyperpolarized helium-3 diffusion MR imaging. Journal of Magnetic Resonance Imaging 24 (2006) 1277-1283.

[17] M.C. Fischer, S. Kadlecek, J.S. Yu, M. Ishii, K. Emami, V. Vahdat, D.A. Lipson, and R.R. Rizi, Measurements of regional alveolar oxygen pressure using hyperpolarized He-3 MRI. Academic Radiology 12 (2005) 1430-1439.

[18] B.M. Goodson, Nuclear magnetic resonance of laser-polarized noble gases in molecules, materials, and organisms. Journal of Magnetic Resonance 155 (2002) 157-216.

[19] C. Dybowski, N. Bansal, and T.M. Duncan, Nmr-Spectroscopy of Xenon in Confined Spaces - Clathrates, Intercalates, and Zeolites. Annual Review of Physical Chemistry 42 (1991) 433-464.

[20] M.A. Springuel-Huet, J.L. Bonardet, A. Gedeon, and J. Fraissard, Xe-129 NMR overview of xenon physisorbed in porous solids. Magnetic Resonance in Chemistry 37 (1999) S1-S13.

[21] C.I. Ratcliffe, Xenon NMR. Annual Reports on NMR Spectroscopy 36 (1998) 123-221.

[22] D. Raftery, and B.F. Chmelka, Xenon NMR Spectroscopy. NMR Basic Principles and Progress 30 (1994) 111-158.

[23] D. Raftery, Xenon NMR Spectroscopy. Annual Reports on NMR Spectroscopy 57 (2006) 205-271.

[24] A. Cherubini, and A. Bifone, Hyperpolarised xenon in biology. Progress in Nuclear Magnetic Resonance Spectroscopy 42 (2003) 1-30.

[25] H.E. Moller, X.J. Chen, B. Saam, K.D. Hagspiel, G.A. Johnson, T.A. Altes, E.E. de Lange, and H.U. Kauczor, MRI of the lungs using hyperpolarized noble gases. Magnetic Resonance in Medicine 47 (2002) 1029-1051.

[26] A.M. Oros, and N.J. Shah, Hyperpolarized xenon in NMR and MRI. Physics in Medicine and Biology 49 (2004) R105-R153.

[27] T. Meersmann, J.W. Logan, R. Simonutti, S. Caldarelli, A. Comotti, P. Sozzani, L.G. Kaiser, and A. Pines, Exploring single-file diffusion in one-dimensional nanochannels by laser-polarized Xe-129 NMR spectroscopy. Journal of Physical Chemistry A 104 (2000) 11665-11670.

[28] C.Y. Cheng, and C.R. Bowers, Direct observation of atoms entering and exiting L-Alanyl-L-valine nanotubes by hyperpolarized xenon-129 NMR. Journal of the American Chemical Society 129 (2007) 13997-14002.

[29] S. Anala, G.E. Pavlovskaya, P. Pichumani, T.J. Dieken, M.D. Olsen, and T. Meersmann, In situ NMR spectroscopy of combustion. Journal of the American Chemical Society 125 (2003) 13298-13302.

[30] J.A. Ripmeester, and D.W. Davidson, Xe-129 Nuclear Magnetic-Resonance in the Clathrate Hydrate of Xenon. Journal of Molecular Structure 75 (1981) 67-72.

[31] M.A. Springuel-Huet, and J. Fraissard, ^{129}Xe NMR of Xenon adsorbed on the molecular sieves ALPO4-11 and SAPO-11 CSA related to the asymmetry of the adsorption zones. Chemical Physics Letters 154 (1989) 299-302.

[32] E. Haddad, A. Nossov, F. Guenneau, and A. Gedeon, General correlation between the chemical shift of hyperpolarized ^{129}Xenon and pore size of mesoporous solids. Comptes Rendus Chimie 7 (2004) 305-310.

[33] C.J. Jameson, A.K. Jameson, R. Gerald, and A.C. Dedios, Nuclear-Magnetic-Resonance Studies of Xenon Clusters in Zeolite Naa. Journal of Chemical Physics 96 (1992) 1676-1689.

[34] R.W. Mair, G.P. Wong, D. Hoffmann, M.D. Hurlimann, S. Patz, L.M. Schwartz, and R.L. Walsworth, Probing porous media with gas diffusion NMR. Physical Review Letters 83 (1999) 3324-3327.

[35] P.K. Weathersby, and L.D. Homer, Solubility of Inert Gases in Biological Fluids: a review. Undersea Biomedical Research 7 (1980) 277-297.

[36] M.S. Albert, V.D. Schepkin, and T.F. Budinger, Measurement of Xe-129 T_1 in Blood to Explore the Feasibility of Hyperpolarized Xe-129 Mri. Journal of Computer Assisted Tomography 19 (1995) 975-978.

[37] S.D. Swanson, M.S. Rosen, B.W. Agranoff, K.P. Coulter, R.C. Welsh, and T.E. Chupp, Brain MRI with laser-polarized Xe-129. Magnetic Resonance in Medicine 38 (1997) 695-698.

[38] J. Kershaw, K. Nakamura, Y. Kondoh, A. Wakai, N. Suzuki, and I. Kanno, Confirming the existence of five peaks in Xe-129 rat head spectra. Magnetic Resonance in Medicine 57 (2007) 791-797.

[39] L. Schroder, T.J. Lowery, C. Hilty, D.E. Wemmer, and A. Pines, Molecular imaging using a targeted magnetic resonance hyperpolarized biosensor. Science 314 (2006) 446-449.

[40] C. Hilty, T.J. Lowery, D.E. Wemmer, and A. Pines, Spectrally resolved magnetic resonance imaging of a xenon biosensor. Angewandte Chemie-International Edition 45 (2006) 70-73.

[41] Z.I. Cleveland, H.E. Moller, L.W. Hedlund, and B. Driehuys, Continuously Infusing Hyperpolarized Xe-129 into Flowing Aqueous Solutions Using Hydrophobic Gas Exchange Membranes. Journal of Physical Chemistry B 113 (2009) 12489-12499.

[42] N. Bloembergen, E.M. Purcell, and R.V. Pound, Relaxation Effects in Nuclear Magnetic Resonance Absorption. Physical Review 73 (1948) 679-712.

[43] P. Lauterbur, Image Formation by Induced Local Interactions - Examples Employing Nuclear Magnetic-Resonance. Nature 242 (1973) 190-191.

[44] P.T. Callaghan, Principles of Nuclear Magnetic Resonance Microscopy, Oxford University press, New York, 1991.

[45] G.E. Pavlovskaya, Z.I. Cleveland, K.F. Stupic, and T. Meersmann, Hyperpolarized Krypton-83 as a New Contrast Agent for Magnetic Resonance Imaging. Proceedings of the National Academy of Sciences of the United States of America 102 (2005) 18275-18279.

[46] G. Pavlovskaya, A.K. Blue, S.J. Gibbs, M. Haake, F. Cros, L. Malier, and T. Meersmann, Xenon-131 surface sensitive imaging of aerogels in liquid xenon near the critical point. Journal of Magnetic Resonance 137 (1999) 258-264.

[47] L.G. Kaiser, T. Meersmann, J.W. Logan, and A. Pines, Visualization of gas flow and diffusion in porous media. Proceedings of the National Academy of Sciences of the United States of America 97 (2000) 2414-2418.

[48] B. Driehuys, G.P. Cofer, J. Pollaro, J.B. Mackel, L.W. Hedlund, and G.A. Johnson, Imaging alveolar-capillary gas transfer using hyperpolarized Xe-129 MRI. Proceedings of the National Academy of Sciences of the United States of America 103 (2006) 18278-18283.

[49] R. Damadian, Tumor Detection by Nuclear Magnetic Resonance. Science 171 (1971) 1151-&.

[50] M.E. Wagshul, and T.E. Chupp, Laser Optical-Pumping of High-Density Rb in Polarized He-3 Targets. Physical Review A 49 (1994) 3854-3869.

[51] R.M. Herman, Theory of Spin Exchange between Optically Pumped Rubidium and Foreign Gas Nuclei. Physical Review 137 (1965) 1062-1065.

[52] M.A. Bouchiat, J. Brossel, and L.C. Pottier, Evidence for Rb Rare-Gas Molecules from Relaxation of Polarized Rb-Atoms in a Rare-Gas - Experimental Results. Journal of Chemical Physics 56 (1972) 3703-3714.

[53] X. Zeng, Z. Wu, T. Call, E. Miron, D. Schreiber, and W. Happer, Experimental-Determination of the Rate Constants for Spin Exchange between Optically Pumped K, Rb, and Cs Atoms and Xe-129 Nuclei in Alkali-Metal Noble-Gas van der Waals Molecules. Physical Review A 31 (1985) 260-278.

[54] W. Happer, and W.A. Vanwijngaarden, An Optical-Pumping Primer. Hyperfine Interactions 38 (1987) 435-470.

[55] B. Driehuys, G.D. Cates, E. Miron, K. Sauer, D.K. Walter, and W. Happer, High-volume production of laser-polarized Xe-129. Applied Physics Letters 69 (1996) 1668-1670.

[56] G.D. Cates, R.J. Fitzgerald, A.S. Barton, P. Bogorad, M. Gatzke, N.R. Newbury, and B. Saam, Rb Xe-129 Spin-Exchange Rates Due to Binary and 3-Body Collisions at High Xe Pressures. Physical Review A 45 (1992) 4631-4639.

[57] T.J. Killian, Thermionic phenomena caused by vapors of rubidium and potassium. Physical Review 27 (1926) 578-587.

[58] W. Happer, Optical-Pumping. Reviews of Modern Physics 44 (1972) 169-&.

[59] J.N. Zerger, M.J. Lim, K.P. Coulter, and T.E. Chupp, Polarization of Xe-129 with high power external-cavity laser diode arrays. Applied Physics Letters 76 (2000) 1798-1800.

[60] E. Babcock, B. Chann, I.A. Nelson, and T.G. Walker, Frequency-narrowed diode array bar. Applied Optics 44 (2005) 3098-3104.

[61] P. Nikolaou, N. Whiting, N.A. Eschmann, K.E. Chaffee, B.M. Goodson, and M.J. Barlow, Generation of laser-polarized xenon using fiber-coupled laser-diode arrays narrowed with integrated volume holographic gratings. Journal of Magnetic Resonance 197 (2009) 249-254.

[62] R.W. Mair, M.J. Barlow, M.S. Rosen, and R.L. Walsworth, Improved noble gas polarization production for porous and granular media studies using narrowed-line VBG laser sources. Journal of Magnetic Resonance 25 (2007) 549.

[63] A.L. Zook, B.B. Adhyaru, and C.R. Bowers, High capacity production of > 65% spin polarized xenon-129 for NMR spectroscopy and imaging. Journal of Magnetic Resonance 159 (2002) 175-182.

[64] I.C. Ruset, S. Ketel, and F.W. Hersman, Optical pumping system design for large production of hyperpolarized Xe-129. Physical Review Letters 96 (2006) 053002.

[65] Z.I. Cleveland, G.E. Pavlovskaya, K.F. Stupic, C.F. LeNoir, and T. Meersmann, Exploring hyperpolarized ^{83}Kr by remotely detected NMR relaxometry. Journal of Chemical Physics 124 (2006) 044312.

[66] M.S. Rosen, T.E. Chupp, K.P. Coulter, R.C. Welsh, and S.D. Swanson, Polarized Xe-129 optical pumping/spin exchange and delivery system for magnetic resonance

spectroscopy and imaging studies. Review of Scientific Instruments 70 (1999) 1546-1552.

[67] M. Gatzke, G.D. Cates, B. Driehuys, D. Fox, W. Happer, and B. Saam, Extraordinarily Slow Nuclear-Spin Relaxation in Frozen Laser-Polarized Xe-129. Physical Review Letters 70 (1993) 690-693.

[68] D.F. Cowgill, and R.E. Norberg, Spin-Lattice Relaxation and Chemical-Shift of Kr-83 in Solid and Liquid Krypton. Physical Review B 8 (1973) 4966-4974.

[69] W.W. Warren, and R.E. Norberg, Nuclear Quadrupole Relaxation and Chemical Shift of Xe-131 in Liquid and Solid Xenon. Physical Review 148 (1966) 402-412.

[70] W.W. Warren, and R.E. Norberg, Multiple-Pulse Nuclear-Magnetic-Resonance Transients of Xe-129 and Xe-131in Solid Xenon. Physical Review 154 (1967) 277-&.

[71] B.C. Grover, Noble-Gas Nmr Detection through Noble-Gas-Rubidium Hyperfine Contact Interaction. Physical Review Letters 40 (1978) 391-392.

[72] R.K. Mazitov, K.M. Enikeev, and A.V. Ilyasov, Magnetic-Resonance and Relaxation of Nuclei of Atomic Krypton in Liquid Solutions. Zeitschrift Fur Physikalische Chemie Neue Folge 155 (1987) 55-68.

[73] T.G. Walker, Estimates of Spin-Exchange Parameters for Alkali-Metal Noble-Gas Pairs. Physical Review A 40 (1989) 4959-4963.

[74] R. Butscher, G. Wäckerle, and M. Mehring, Nuclear quadrupole surface interaction of gas phase ^{83}Kr: comparison with ^{131}Xe. Chemical Physics Letters 249 (1996) 444-450.

[75] C.H. Volk, J.G. Mark, and B.C. Grover, Spin Dephasing of Kr-83. Physical Review A 20 (1979) 2381-2388.

[76] K.F. Stupic, Z.I. Cleveland, G.E. Pavlovskaya, and T. Meersmann, Quadrupolar Relaxation of Hyperpolarized Krypton-83 as a Probe for Surfaces. Solid State Nuclear Magnetic Resonance 29 (2006) 79-84.

[77] Z.I. Cleveland, K.F. Stupic, G.E. Pavlovskaya, J.E. Repine, J.B. Wooten, and T. Meersmann, Hyperpolarized Kr-83 and Xe-129 NMR relaxation measurements of hydrated surfaces: Implications for materials science and pulmonary diagnostics. Journal of the American Chemical Society 129 (2007) 1784-1792.

[78] Z.I. Cleveland, G.E. Pavlovskaya, K.F. Stupic, J.B. Wooten, J.E. Repine, and T. Meersmann, Detection of Tobacco Smoke Deposition by Hyperpolarized Krypton-83 MRI. Magnetic Resonance Imaging 26 (2008).

[79] Z.I. Cleveland, G.E. Pavlovskaya, N.D. Elkins, K.F. Stupic, J.E. Repine, and T. Meersmann, Hyperpolarized Kr-83 MRI of lungs. Journal of Magnetic Resonance 195 (2008) 232-237.

[80] Z.I. Cleveland, and T. Meersmann, Binary-collision-induced longitudinal relaxation in gas-phase Kr-83. Journal of Chemical Physics 129 (2008) 6.

[81] Z.I. Cleveland, and T. Meersmann, Density-independent contributions to longitudinal relaxation in Kr-83. Chemphyschem 9 (2008) 1375-1379.

[82] D. Brinkmann, Local Magnetic Field Shift in Natural Krypton. Physics Letters A A 25 (1967) 520-521.

[83] D.F. Cowgill, and R.E. Norberg, Pulsed Nmr-Studies of Self-Diffusion and Defect Structure in Liquid and Solid Krypton. Physical Review B 13 (1976) 2773-2781.

[84] E.I. Madaras, and R.E. Norberg, Kr-83 in Solid Krypton .1. Defects and Diffusion. Physical Review B 33 (1986) 5999-6014.

[85] E.I. Madaras, and R.E. Norberg, Kr-83 in Solid Krypton .2. Rotating-Frame Relaxation and Spectral Diffusion. Physical Review B 33 (1986) 6015-6024.

[86] P. Ingman, J. Jokisaari, and P. Diehl, Kr-83 and Xe-131-Nmr of the Noble-Gases Dissolved in Nematic Liquid-Crystals - Determination of Quadrupole Couplings and Electric-Field Gradients. Journal of Magnetic Resonance 92 (1991) 163-169.

[87] J.H. Lounila, O. Muenster, J. Jokisaari, and P. Diehl, Temperature-Dependence of Nuclear Shielding and Quadrupolar Coupling of Noble-Gases in Liquid-Crystals. Journal of Chemical Physics 97 (1992) 8977-8985.

[88] J. Jokisaari, P. Ingman, J. Lounila, O. Pukkinen, P. Diehl, and O. Muenster, Electric-Field Gradients Experienced by the Noble-Gas Isotopes Ne-21, Kr-83 and Xe-131 in Thermotropic Liquid-Crystals. Molecular Physics 78 (1993) 41-54.

[89] C.F. Horton-Garcia, G.E. Pavlovskaya, and T. Meersmann, Introducing krypton NMR spectroscopy as a probe of void space in solids. Journal of the American Chemical Society 127 (2005) 1958-1962.

[90] D. Brinkmann, E. Brun, and H.H. Staub, Kernresonanz Im Gasformigen Xenon. Helvetica Physica Acta 35 (1962) 431-436.

[91] M. Luhmer, and J. Reisse, Quadrupole NMR relaxation of the noble gases dissolved in simple liquids and solutions - A critical review of experimental data in the light of computer simulation results. Progress in Nuclear Magnetic Resonance Spectroscopy 33 (1998) 57-76.

[92] J. Jokisaari, Nmr of Noble-Gases Dissolved in Isotropic and Anisotropic Liquids. Progress in Nuclear Magnetic Resonance Spectroscopy 26 (1994) 1-26.

[93] T. Meersmann, and M. Haake, Magnetic field dependent xenon-131 quadrupolar splitting in gas and liquid phase NMR. Physical Review Letters 81 (1998) 1211-1214.

[94] J. F. R. Salsbury, and R.A. Harris, The origin of the magnetic-field dependent quadrupolar splitting. JCP 109 (1998) 8338-8341.

[95] J. Vaara, and P. Pyykko, Magnetic-field-induced quadrupole splitting in gaseous and liquid Xe-131 NMR: Quadratic and quartic field dependence. Physical Review Letters 86 (2001) 3268-3271.

[96] T.M. Kwon, J.G. Mark, and C.H. Volk, Quadrupole Nuclear-Spin Relaxation of Xe-131 in the Presence of Rubidium Vapor. Physical Review A 24 (1981) 1894-1903.

[97] Z. Wu, W. Happer, and J.M. Daniels, Coherent Nuclear-Spin Interaction of Adsorbed 131Xe Gas with Surfaces. Phys. Rev. Lett. 59 (1987) 1480-1483.

[98] Z. Wu, S. Schaefer, G.D. Cates, and W. Happer, Coherent interactions of polarized nuclear spins of gaseous atoms with container walls. Physical Review A 37 (1988) 1161-1175.

[99] Z. Wu, W. Happer, M. Kitano, and J. Daniels, Experimental Studies of Wall Interactions of Adsorbed Spin-Polarized Xe-131 Nuclei. Physical Review A 42 (1990) 2774-2784.

[100] D. Raftery, H.W. Long, D. Shykind, P.J. Grandinetti, and A. Pines, Multiple-Pulse Nuclear-Magnetic-Resonance of Optically Pumped Xenon in a Low Magnetic-Field. Physical Review A 50 (1994) 567-574.

[101] R. Butscher, G. Wäckerle, and M. Mehring, Nuclear quadrupole interaction of highly polarized gas phase ^{131}Xe with a glass surface. Journal of Chemical Physics 100 (1994) 6923-6933.

[102] J. Luo, X. Mao, J. Chen, S. Wang, M. Zhao, L. Fu, and X. Zeng, Frequency-selective laser optical pumping and spin exchange of cesium with Xe-129 and Xe-131 in a high magnetic field. Applied Magnetic Resonance 17 (1999) 587-595.

[103] E.A. Donley, J.L. Long, T.C. Liebisch, E.R. Hodby, T.A. Fisher, and J. Kitching, Nuclear quadrupole resonances in compact vapor cells: The crossover between the NMR and the nuclear quadrupole resonance interaction regimes. Physical Review A 79 (2009) 5.

CHAPTER 2

Quadrupolar Relaxation of Hyperpolarized Krypton-83 as a Probe for Surfaces

This chapter is a reproduction of the journal article by Karl F. Stupic, Zackary I. Cleveland, Galina E. Pavlovskaya, and Thomas Meersmann, titled: "Quadrupolar Relaxation of Hyperpolarized Krypton-83 as a Probe for Surfaces", published in the journal of *Solid State Nuclear Magnetic Resonance* in 2006, pages 79-84. This article is reproduced for the dissertation under the privileges afforded to the authors of the paper by the publisher, Elsevier.

The publication presented in *Solid State Nuclear Magnetic Resonance* was written by Thomas Meersmann, Karl F. Stupic, and Zackary I. Cleveland with Karl F. Stupic and Zackary I. Cleveland collecting the data presented in the publication. Galina E. Pavlovskaya provided technical advice and edited the manuscript. A discussion of data concerning hp ^{83}Kr relaxation on glass beads including an altered version of Fig. 2.2 appeared in the dissertation of Zackary I. Cleveland.

2.1. Introduction

The only stable NMR active isotope of the noble gas krypton, ^{83}Kr, has a natural abundance of 11.5 % and a NMR resonance frequency of 15.4 MHz at 9.4 T magnetic field strength. Because of its spin I = 9/2, the nucleus of ^{83}Kr possesses an electric quadrupole moment (Q = 0.28 10^{-28} m^2). An anisotropic environment will induce an electric field gradient in the electronic cloud of the noble gas atom, and quadrupolar coherence can cause quadrupolar splitting if the anisotropy has a macroscopic net alignment with respect to the magnetic field. This has been observed previously by conventional NMR with krypton dissolved in nematic phase liquid crystals [1; 2; 3] and by optically detected magnetic resonance in quadrupole nutation experiments of gaseous krypton within non-spherical macroscopic glass containers [4; 5]. In the absence of unpaired electrons, the quadrupole moment is the dominating factor for relaxation of the ^{83}Kr nuclear spin in gas, liquid, and solid phases [6; 7; 8]. The ^{83}Kr NMR relaxation in various liquid solutions has been studied in the past [3; 9; 10; 11; 12; 13], and the chemical shift in gas and dissolved phases has been investigated [3; 9; 14; 15]. Krypton has also been used to explore nanoporous materials indirectly through ^{129}Xe NMR chemical shift measurements in xenon-krypton gas mixtures within zeolites [16; 17]. Recently, direct ^{83}Kr NMR observations of this noble gas inside a number of zeolites have been reported [18]. The ^{83}Kr lineshape was found to strongly depend on internal cage structure and the charge of the cations inside the nanoporous materials. The field dependence of the lineshape observed in some Ca^{2+} exchanged zeolites has been attributed to long-range disorder. The ^{83}Kr chemical shift has been studied as a function of krypton loading in these materials, but the contributions from the second-order

quadrupolar interactions to the observed shift remain unexplored thus far. Despite the low sensitivity of natural abundance ^{83}Kr (i.e. about 3.8% of the sensitivity obtained from thermally spin polarized ^{129}Xe), meaningful ^{83}Kr NMR measurements in zeolites can typically be accomplished within a few hours at medium field strength (i.e. 9.4 T) with thermally polarized krypton. This is possible because of the relatively fast longitudinal relaxation of ^{83}Kr that ranges from milliseconds to tens of milliseconds in these materials.

The usage of thermally polarized ^{83}Kr as a probe for materials with small surface to volume ratios is hampered in part by the lower krypton loading compared to those found in zeolites. Even more problematic for ^{83}Kr NMR are the increased longitudinal relaxation times in large pore materials with typical values ranging from seconds to many tens of seconds. However, experiments with small surface areas have become feasible because of recent developments in optical pumping that lead to the production of hyperpolarized (hp) ^{83}Kr for NMR and MRI applications [19]. The theoretical longitudinal relaxation time of ^{83}Kr in the pure gas phase (i.e. in the absence of a container wall) at 300 K, 100 kPa and 2.1 T can be estimated as T_1 = 470 s [8]. However, longitudinal relaxation times of 90–150 s have been measured in 10–11.5 mm diameter and 4–5 cm long glass cylinders at 289 K, 100–200 kPa, and 9.4 T (with the relaxation rates also depending on the treatment of the glass surface). The long relaxation time of ^{83}Kr in the gas phase allows for the production of hp ^{83}Kr by spin exchange optical pumping with rubidium vapor [20] and for the subsequent separation of the alkali metal from the hyperpolarized ^{83}Kr gas [19]. Signal enhancements of more than three orders of magnitude compared to thermally polarized ^{83}Kr NMR signals at ambient temperature and 9.4 T have been achieved. The apparatus and procedure for the production of hp ^{83}Kr

is briefly described in the Section 2. Details of the proof of principle optical pumping work including the first applications of hp ^{83}Kr MRI are discussed elsewhere [19].

2.2. Methods and materials

2.2.1. Krypton optical pumping

A number of researchers have explored alkali metal vapor optical pumping of quadrupolar noble gas isotopes, including ^{83}Kr, in the past [4; 5; 20; 21; 22; 23; 24; 25; 26; 27]. The setup described here has been used for the first successful separation of a hp noble gas with a quadrupolar nucleus from the rubidium vapor [19]. The separation process is similar to the ones previously used for production of non-quadrupolar hp noble gases in batch or continuous flow modes [28; 29; 30; 31; 32; 33; 34]. The separation of the hp gas from the rubidium vapor is crucial for NMR and MRI applications because of the reactivity of alkali metals. The experimental setup is similar to the one reported in literature for the production of hp ^{129}Xe (I = 1/2) [31; 33; 34]. The gas mixture used for all experiments reported in this publication consists of a high concentration of natural abundance krypton (typically 95%) and about 5% of molecular nitrogen added for radiation quenching purposes [35]. The gas pressure in the pumping cell ranged from 110 kPa to 220 kPa. Pumping with high noble gas density has been thoroughly explored for ^{129}Xe [33; 35; 36; 37; 38] and is found to be vital for obtaining the highest signal intensities with hp ^{83}Kr. A COHERENT 60 W continuous wave diode array solid-state laser system is applied to the stopped flow type pumping process and leads to a signal enhancement of about 1200 times greater than the thermal signal at 9.4 T and 300 K [19]. Research grade natural abundance krypton (99.995%; Airgas, Radnor, PA) is used for the

pumping in a cylindrical Pyrex cell (length = 125 mm, I.D. = 24 mm) that contains 2.5 – 5.0 g of rubidium (99.6%; Sigma-Aldrich, Milwaukee, WI & 99.75%; Alfa Aesar, Ward Hill, MA). The temperature of the cell is maintained at approximately 433 K, a pumping cell temperature that is about 40 K higher than the temperature typically used for hp ^{129}Xe. In the stopped flow experiments the sample is evacuated to 0.1 kPa and the krypton-nitrogen gas mixture is kept under laser radiation for 10 min. Subsequently, the optically pumped krypton is transferred using pressure equalization into the sample cell where a krypton gas pressure range of 100 – 200 kPa is maintained. The rubidium vapor is separated from the krypton by an air-cooled filter located inside the transfer line between the pumping cell and the detection cell.

2.2.2. NMR measurements

Experiments are performed at 15.4 MHz with a Chemagnetics CMX II spectrometer and a 9.4 T wide-bore (89 mm) superconducting magnet. T_1 values from optical pumping data are calculated by nonlinear least-squares fitting of the ^{83}Kr signal intensity as a function of time and number of applied medium flip angle (12°) r.f. pulses (see Fig. 2.1).

2.2.3. Preparation of samples

The 0.1 – 2.5 mm diameter glass beads (Biospec Products, Inc., Bartlesville, OK) are degassed overnight at a pressure of less than 0.1 Pa and stored under dry nitrogen until use. The beads used as obtained from the supplier except for overnight degassing under vacuum conditions are referred to within this text as ‘untreated beads’. The ‘pretreated glass beads’ are obtained by washing untreated beads for 15 min with a 1:1:5 solution of 30% v/v NH_4OH, 30% v/v H_2O_2, and distilled water while stirring vigorously.

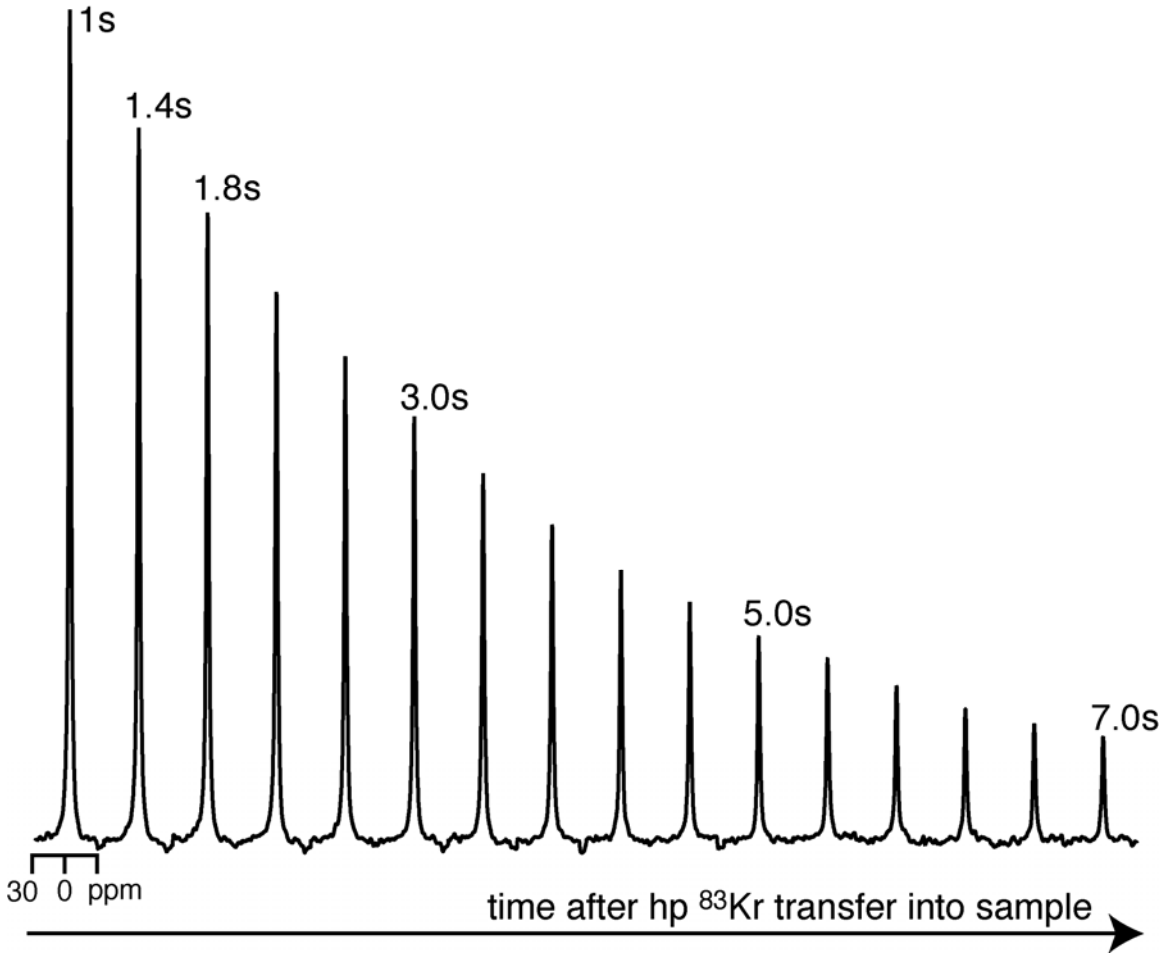

Fig. 2.1: Signal intensity decay resulting from T_1 relaxation and the application of a series of medium flip angle r.f. pulses. Using stopped flow optical pumping, hyperpolarized ^{83}Kr is transferred into a sample of porous polyethylene (mean pore size 70 μm). Signal is acquired by applying a series of sixteen 12° r.f. pulses spaced evenly every 0.4 s. Similarly robust decay patterns are observed in all of the porous samples studied.

Following NH_4OH/H_2O_2 treatment, the beads are washed for 15 min at 358 K with a 1:1:5 solution of 30% v/v HCl, 30% v/v H_2O_2, and distilled water while stirring vigorously. The beads are then washed five times with distilled water and dried in a vacuum desiccator at 523 K for 1 h. 'Siloxane treated beads' are pretreated beads siliconized with a 1:10 mixture of SurfaSil^{TM} (Pierce Biotechnology Inc., Rockford, IL) in acetone and washed with distilled water in accordance with the manufacturer's instructions. 'Fluorosilane treated beads' are obtained from pretreated beads through reaction with a 1:100 mixture of (3,3,3-Trifluoropropyl) tri-methoxyl silane (Gelest Inc., Morrisville, PA) in toluene with occasional stirring for 3 hours and later washed with toluene 4 times followed by drying in a vacuum desiccator at 398 K overnight.

The 70 - 250 μm porous polyethylene samples (Small Parts, Inc., Miami Lakes, FL) are degassed overnight at pressure of less than 0.1 Pa and stored under dry nitrogen until use.

2.3. Results and discussion

Glass beads of four different sizes (i.e. 0.1 mm, 0.5 mm, 1.0 mm and 2.5 mm) are separately placed in a 10.8 mm I.D. sample cell that is connected to the pumping cell through a PFA transfer line. The beads are assumed to be in an arrangement resembling the closest packing of spheres with a constant total pore volume of 26% of the overall sample. The pores are the tetrahedral and octahedral holes expected from the closest packing and can accommodate spherical objects of radii up to r = 0.223 and r = 0.414 respectively, if the radius of the closest packed beads is r = 1. Deviations from the ideal packing occur because of the finite sample container dimensions and are most

pronounced for the beads with the largest diameter (2.5 mm). Nevertheless, these test systems are reasonably well defined especially for beads with smaller radii and can easily be reproduced. Four different types of surfaces have been explored by ^{83}Kr NMR, namely untreated, pretreated, siloxane treated and fluorosilane treated glass beads as described in Section 2. The results of the ^{83}Kr NMR relaxation measurements are summarized in Table 2.1 and Fig. 2.2. The ^{83}Kr relaxation rates are found to increase with decreasing pore size for all surfaces studied except for the fluorosilane sample where only one bead size was used. The geometry of the pores is unaffected by the bead diameter. Thus the effect must be caused by the surface to volume ratio of the material that is directly proportional to the inverse radius of the spheres if ideal packing is assumed. Fig. 2.2 depicts the relaxation rates as a function of inverse bead radius. The general dependence of the observed relaxation on inverse radius (i.e. surface to volume ratio) is not unexpected since longitudinal relaxation in quadrupolar noble gasses caused by surface collisions has been observed before in the case of ^{131}Xe (I = 3/2) [26; 39; 40; 41]. In the current study the noble gas is detected in the bulk gas phase, but the major source of relaxation is caused by the particularly pronounced quadrupolar interactions during brief adsorption periods of the atoms on the surrounding surfaces. The longest ^{83}Kr relaxation times of T_1 = 90–150 s are observed in detection cells without beads where the container walls remain as the sole exposed surface. If quadrupolar interactions on the surface are the only source for the observed relaxation, a linear dependence of the relaxation rates on the inverse radii is anticipated. A clear deviation from the expected linear behavior is observed in particular for the larger diameter beads probably because of non-ideal packing and a more significant contribution from relaxation at the container glass wall.

Bead Dia. (mm)	Untreated Beads T_1 (s)	Pretreated Beads T_1 (s)	Fluorosilane Treated Beads T_1 (s)	Siloxane Treated Beads T_1 (s)
2.5	53 ± 1	35.2	---	21.1 ± 0.9
1.0	35.3 34.3 (200 kPa)[a]	20.5	15.2 ± 0.5	9.0 ± 0.2 9.0 (200 kPa) [a]
0.5	29.0	17.9	---	6.1 ± 0.3
0.1	15.0	6.5	---	2.5 ± 0.1 2.6 (thermal) [b]

Table 2.1: ^{83}Kr T_1 relaxation times in the void spaces of surface treated glass beads.

T_1 values were measured using hyperpolarized ^{83}Kr at 100 kPa and 9.4 T unless otherwise specified. The uncertainties are the standard deviation in T_1 measurements and are reported only when at least four measurements were performed.

[a] The value was obtained from hyperpolarized ^{83}Kr at 200 kPa.

[b] The reported value was obtained from thermally polarized ^{83}Kr at 100 kPa and a magnetic field strength of 14.1 T. The saturation experiment used to measure the T_1 value comprises 6000 signal acquisitions at each time delay. The total experimental time for this data point was approximately 4 days.

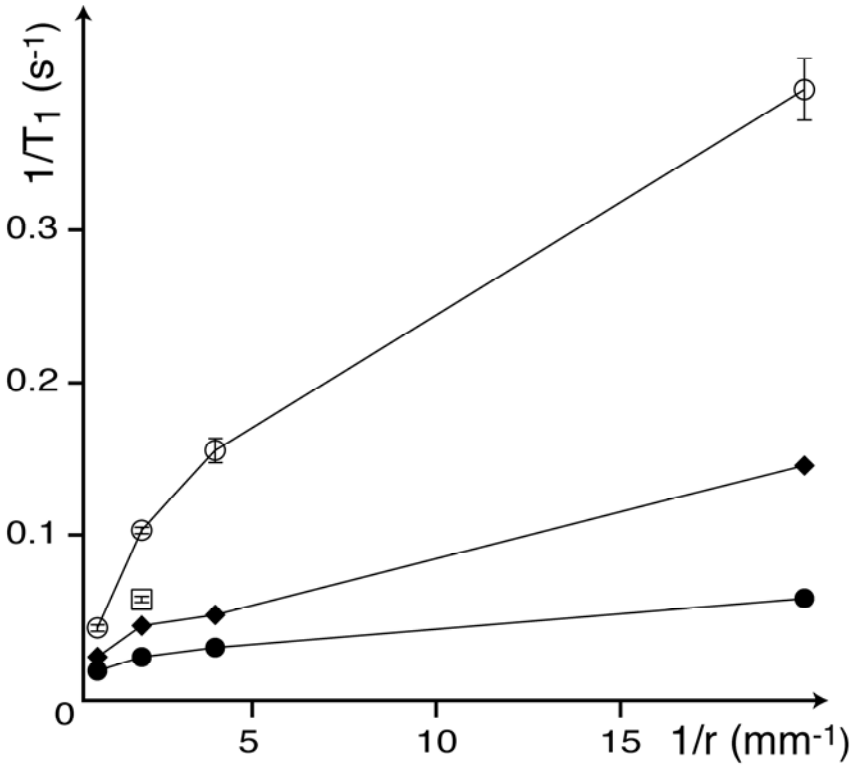

Fig. 2.2: Relaxation rates versus inverse bead radii from the experimental results summarized in Table 2.1. The inverse radius is directly proportional to the surface to volume ratio in the porous samples. Relaxation rates for the various bead surfaces are represented by the following symbols: siloxane treated – open circles, pretreated – closed diamonds, and untreated – closed circles. The single data point for a flourosilane treated surface (1.0 mm beads) is represented by an open square. Error bars represent standard deviations resulting from at least four replicate measurements. The lines are only intended as guides to the eye.

A more detailed mapping of the relaxation dependence on bead diameter (with bead diameters < 0.5 mm) is needed to quantify the effect. Note that generation of quadrupolar coherence [40; 41; 42; 43; 44] is not investigated in this work. In ideal closest packed spheres such coherence is not predicted because of the high symmetry of tetrahedral and octahedral pores.

Beyond the surface to volume ratio a second parameter has to be considered, namely the van der Waals interactions that are the driving force for the hp ^{83}Kr adsorption on the surface. The non-polar but highly polarizable krypton electron cloud leads to more favorable surface adsorption enthalpies with non-polar (i.e. hydrophobic) surfaces than with polar (i.e. hydrophilic) surfaces. The slopes for linear fitting in Fig. 2.2 are correlated to the strength of the interaction between the surface and the krypton atoms. The longitudinal relaxation depends significantly on the chemical composition of the surface, that may influence the adsorption time, the surface coverage, and the magnitude of the quadrupolar coupling. The relaxation times are therefore shorter in glass beads with siloxane treated (i.e. non-polar) surfaces than in the untreated or pretreated beads. The opposite effect is observed with ^{129}Xe and ^{3}He NMR $I = 1/2$ [45; 46], because the surface coating insulates the noble gas atoms from magnetic sites in the glass surface [47] and therefore prolongs the lifetime of the hp magnetization for spin $I = 1/2$ noble gasses. However, the quadrupolar relaxation of ^{83}Kr dominates over all other types of relaxation in this study resulting in the observed trend.

The cause for the difference in the observed krypton relaxation between untreated and pretreated surfaces is less obvious than the source of the difference between untreated and siloxane treated surfaces. In addition to being more fully covered with

hydroxyl groups than the untreated surfaces, it can be speculated that the pretreated surfaces have activated adsorption sites or perhaps greater surface corrugation. The only fluorosilane sample tested is made of coated 1.0 mm glass beads and results in slower relaxation than the siloxane (hydrophobic) treated surface but faster relaxation than that found in pretreated and untreated 1.0 mm beads.

Little effect on the relaxation rates is observed when the krypton gas pressure is varied by a factor of 2 (from 100 kPa to 200 kPa), therefore the method can be considered rather robust. At a first glance this may appear suprising since the ^{83}Kr bulk gas phase relaxation rate is directly proportional to the gas density [8] and therefore directly proportional to the gas pressure (assuming ideal gas behavior). However, any change in the bulk gas phase relaxation will have little effect on the observed relaxation, because pure gas phase relaxation is about one order of magnitude slower than the observed rates that are dominated by surface processes. At the conditions used in this study, the surface coverage of krypton atoms should approximately be directly proportional to the gas pressure (i.e. Langmuir isotherm for case with low surface coverage). Therefore, the ratio between atoms in the gas phase and atoms adsorbed on the surfaces should be somewhat constant leading to relaxation rates that are relatively independent of the gas pressure. Although not tested in this work, a more extreme change in pressure should have a stronger influence on diffusion, surface adsorption and therefore on the relaxation rates.

The measurement of longitudinal relaxation in the 0.1 mm siloxane coated sample with thermally polarized ^{83}Kr at 100 kPa and 14.1 T field strength did not show significant deviation from the optical pumping data at 9.4 T (Table 2.1). This indicates

there is no dramatic field dependence at these field strengths as is to be expected from quadrupolar relaxation under these conditions (i.e. short mean adsoption times and therefore short correlation times τ_c). Because the thermal measurement for even the fastest relaxing sample took about four days (as opposed to less than 15 min for the optical pumping experiments), only one such measurement is available to date.

This new method is also explored in systems that are less ideal than the glass beads. Fig. 2.3 shows the ^{83}Kr NMR spectrum of krypton inside a porous polymer sample with 70 μm mean pore size and of bulk gas phase krypton at 100 kPa pressure. The gas phase peak has been referenced to 0 ppm, and the krypton gas inside the polymer appears upfield shifted at -1.84 ppm. The ^{83}Kr is observed to resonate between -1 to -2 ppm for the glass beads and the polymer, respectively. From previous experience in ^{129}Xe NMR spectroscopy, it is unexpected to observe a signal from the bulk gas phase that resonates at higher frequency than the noble gas contained in a porous material [48; 49; 50; 51; 52; 53]. However, the krypton chemical shift inside the macroscopic pores in the polymers used in this work is very small (The ^{129}Xe chemical shift on macroscopic polymer surfaces at ambient temperature is only a few ppm [54], and the krypton chemical shift is generally only a fraction of the xenon shift). Most likely the small downfield krypton chemical shift is not strong enough to offset the shielding effect caused by the magnetic susceptibility of the material. Fig. 2.3 demonstrates the effect of longitudinal relaxation in this sample, clearly distinguishing the gas phase krypton from the krypton in the polymer void spaces because of the higher relaxation rate in the material.

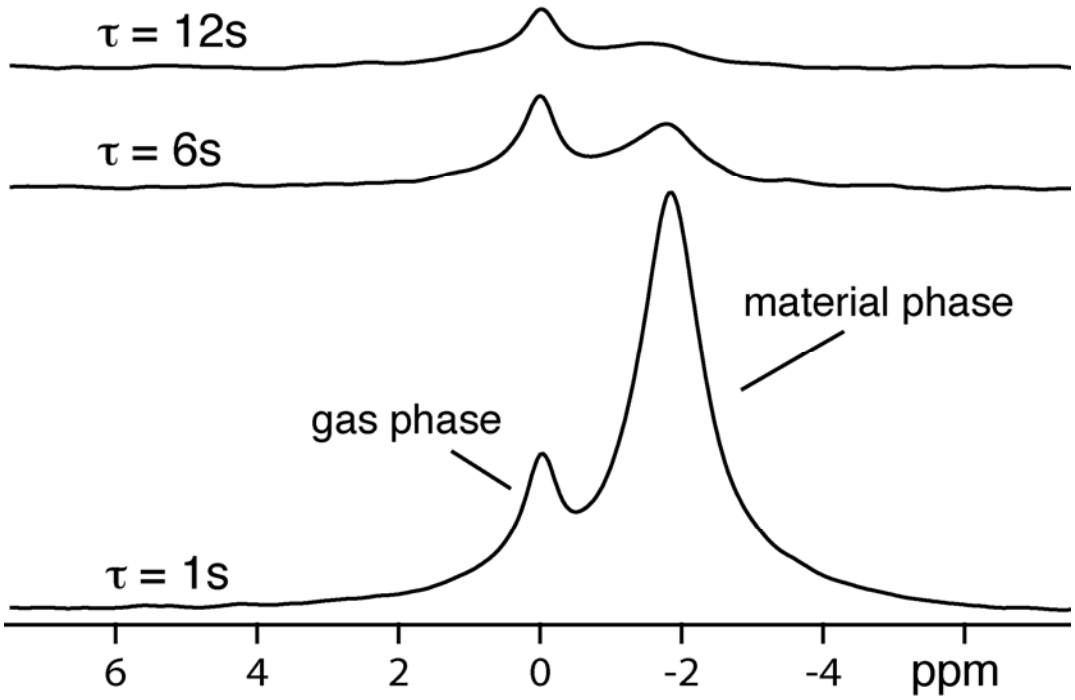

Fig. 2.3: ^{83}Kr NMR spectrum of 70 μm hydrophobic porous polymer (-1.8 ppm) and of (bulk) gas phase at 100 kPa (referenced as 0 ppm). The bulk gas phase is contained inside a PFA tube with a 3.0 mm OD and a 1.65 mm ID located with axial symmetry in a cylindrical polymer sample. The negative (upfield) shift of the krypton inside the material is caused by shielding through the macroscopic magnetic susceptibility of the polymer. The ^{83}Kr NMR spectrum is shown at different delay times, τ, after the transfer of the hyperpolarized gas into the sample. The gas phase peak is clearly identified by its slower relaxation compared to the krypton inside the porous polymer.

Table 2.2 shows the longitudinal relaxation times of hp ^{83}Kr in porous polymers recorded in samples without bulk gas phase. As expected, the relaxation time increases with a more hydrophilic surface compared to a hydrophobic surface with similar pore dimension (90 - 130 μm pore range for the hydrophilic and 120 μm mean pore size for the hydrophobic sample). However, the trend in relaxation dependence on pore sizes in the hydrophobic samples seems to contradict the results obtained with the glass beads. The polymer with the largest mean pore size has the shortest relaxation time, and the polymer with the smallest pores has the longest relaxation time. It is important to note however, that the ^{83}Kr relaxation time does not directly depend on the pore sizes but rather on the surface to volume ratios. In the well-defined glass beads both parameters are directly correlated, however the polymer micrograph in Fig. 2.4 demonstrates a very complex internal structure of the porous polymeric solid that is more difficult to describe explicitly. The surface area could increase with increasing corrugation of the polymer microparticles, even if the average pore size increases. Generally, the ^{83}Kr relaxation times depend directly on surface to volume ratios and not necessarily on the mean pore size that may be determined by alternative techniques.

2.4. Conclusion

It is shown that hp ^{83}Kr NMR relaxation measurements are highly sensitive to the chemical composition of surfaces and to the surface to volume ratios in porous materials. In contrast to direct observation of surfaces by traditional solid-state NMR, hp ^{83}Kr NMR does not require the use of any line narrowing techniques. Sensitivity is often a limiting

Porous Polymer	T_1 (s)
Hydrophobic: 70 μm pores [a]	3.6 ± 0.1
Hydrophobic: 120 μm pores [a]	2.7 ± 0.1
Hydrophilic: 90-130 μm pores [b]	7.1 ± 0.2
Hydrophobic: 250 μm pores [a]	2.1 ± 0.1

Table 2.2: ^{83}Kr T_1 relaxation times in porous polyethylene samples.

The reported uncertainty is the standard deviation resulting from four replicate T_1 measurements.

[a] Mean pore size as stated by the supplier.

[b] Pore range as stated by the supplier.

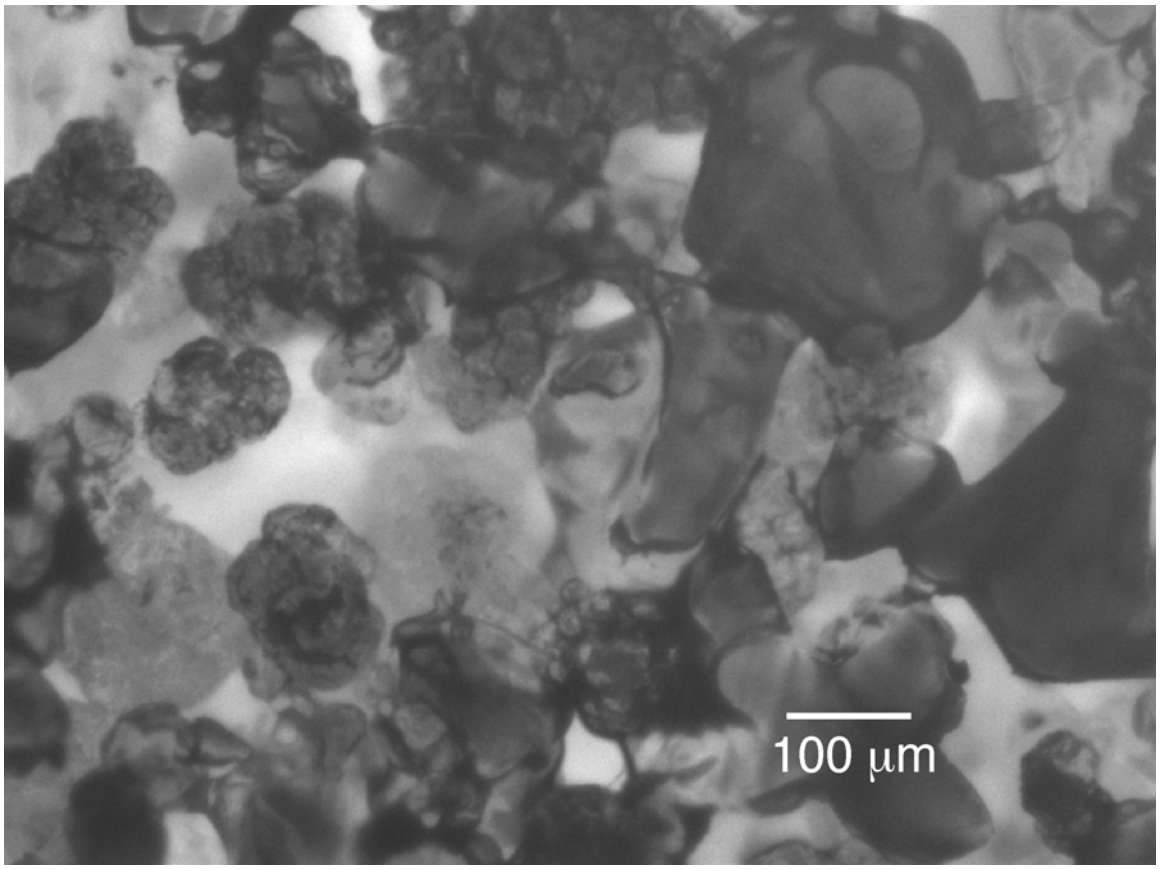

Fig. 2.4: Micrograph of porous polyethylene obtained from an inverted microscope. The sample has a mean pore size of 70 μm as characterized by the supplier. For ^{83}Kr NMR spectra of this sample see Fig. 2.1 and 2.3.

factor in NMR of surfaces but is not an obstacle for hp ^{83}Kr. Furthermore, there is no need to discriminate between signals arising from the sample surface and from the bulk gas phase, since the technique is entirely surface selective. An advantage hp ^{83}Kr NMR has over optical and other surface techniques is that it can be easily applied to opaque and amorphous materials even under atmospheric or greater pressures. Like the well-established ^{129}Xe NMR spectroscopy, the new technique is only an indirect probe for surface structure. However, for the first time a quadrupolar noble gas in a hyperpolarized state is available for materials science studies that provides information highly complementary to that obtained from ^{129}Xe NMR. The closest packed glass beads are an ideal test system for the exploration of the surface sensitivity of new technique. Hp ^{83}Kr NMR might be helpful for instance, in characterizing the homogeneity of grafting, wetting and other surface treatments in amorphous materials.

2.5. Acknowledgements

This material is based upon work supported by the National Science Foundation under Grant No.: CHE-0135082. We thank Michael D. Olsen for glassware preparation; Megan M. Caulum, Yan Liu, and Prof. Charles S. Henry for support with the micrograph image; and Profs. Gary Maciel and David Grainger for instrumental support and stimulating discussions.

References:

[1] P. Ingman, J. Jokisaari, and P. Diehl, Kr-83 and Xe-131-Nmr of the Noble-Gases Dissolved in Nematic Liquid-Crystals - Determination of Quadrupole Couplings and Electric-Field Gradients. Journal of Magnetic Resonance 92 (1991) 163-169.

[2] J. Jokisaari, P. Ingman, J. Lounila, O. Pukkinen, P. Diehl, and O. Muenster, Electric-Field Gradients Experienced by the Noble-Gas Isotopes Ne-21, Kr-83 and Xe-131 in Thermotropic Liquid-Crystals. Molecular Physics 78 (1993) 41-54.

[3] J. Jokisaari, Nmr of Noble-Gases Dissolved in Isotropic and Anisotropic Liquids. Progress in Nuclear Magnetic Resonance Spectroscopy 26 (1994) 1-26.

[4] C.H. Volk, J.G. Mark, and B.C. Grover, Spin Dephasing of Kr-83. Physical Review A 20 (1979) 2381-2388.

[5] R. Butscher, G. Wäckerle, and M. Mehring, Nuclear quadrupole surface interaction of gas phase ^{83}Kr: comparison with ^{131}Xe. Chemical Physics Letters 249 (1996) 444-450.

[6] D.F. Cowgill, and R.E. Norberg, Spin-Lattice Relaxation and Chemical-Shift of Kr-83 in Solid and Liquid Krypton. Physical Review B 8 (1973) 4966-4974.

[7] D.F. Cowgill, and R.E. Norberg, Pulsed Nmr-Studies of Self-Diffusion and Defect Structure in Liquid and Solid Krypton. Physical Review B 13 (1976) 2773-2781.

[8] D. Brinkmann, and D. Kuhn, Nuclear Magnetic-Relaxation of Kr-83 in Krypton Gas. Physical Review A 21 (1980) 163-167.

[9] R.K. Mazitov, K.M. Enikeev, and A.V. Ilyasov, Magnetic-Resonance and Relaxation of Nuclei of Atomic Krypton in Liquid Solutions. Zeitschrift Fur Physikalische Chemie Neue Folge 155 (1987) 55-68.

[10] P. Diehl, and J. Jokisaari, Nuclear Magnetic-Relaxation of the Xe-129 and Xe-131 Isotopes of Xenon Gas Dissolved in Isotropic and Anisotropic Liquids. Journal of Magnetic Resonance 88 (1990) 660-665.

[11] J. Vaara, J. Jokisaari, T.T. Rantala, and J. Lounila, Computational and Experimental-Study of Nmr Relaxation of Quadrupolar Noble-Gas Nuclei in Organic-Solvents. Molecular Physics 82 (1994) 13-27.

[12] M. Holz, R. Haselmeier, A. Klein, and R.K. Mazitov, Temperature-Dependence of Ne-21, Kr-83, and Xe-131 Quadrupole Relaxation and of Xenon Diffusion in Polyatomic Solvents. Applied Magnetic Resonance 8 (1995) 501-519.

[13] M. Luhmer, and J. Reisse, Quadrupole NMR relaxation of the noble gases dissolved in simple liquids and solutions - A critical review of experimental data in the light of computer simulation results. Progress in Nuclear Magnetic Resonance Spectroscopy 33 (1998) 57-76.

[14] J. Lurie, J.L. Feldman, and G.K. Horton, Nuclear Magnetic Resonance Local-Magnetic-Field Shift in Solid Xenon. Physical Review 150 (1966) 180-185.

[15] Brinkman.D, Local Magnetic Field Shift in Natural Krypton. Physics Letters A A 25 (1967) 520-&.

[16] A.K. Jameson, C.J. Jameson, A.C. Dedios, E. Oldfield, R.E. Gerald, and G.L. Turner, Xe-129 Magic-Angle-Spinning Spectra of Xenon in Zeolite Naa - Direct Observation of Mixed Clusters of Coadsorbed Species. Solid State Nuclear Magnetic Resonance 4 (1995) 1-12.

[17] C.J. Jameson, A.K. Jameson, and H.M. Lim, Competitive adsorption of xenon and krypton in zeolite NaA: Xe-129 nuclear magnetic resonance studies and grand canonical Monte Carlo simulations. Journal of Chemical Physics 107 (1997) 4364-4372.

[18] C.F. Horton-Garcia, G.E. Pavlovskaya, and T. Meersmann, Introducing krypton NMR spectroscopy as a probe of void space in solids. Journal of the American Chemical Society 127 (2005) 1958-1962.

[19] Z.I. Cleveland, G.E. Pavlovskaya, K.F. Stupic, T. Meersmann, First presented at 229th ACS meeting, San Diego, CA, March 2005, submitted for publication, 2005.

[20] S.R. Schaefer, G.D. Cates, and W. Happer, Determination of Spin-Exchange Parameters between Optically Pumped Rubidium and Kr-83. Physical Review A 41 (1990) 6063-6070.

[21] B.C. Grover, Noble-Gas Nmr Detection through Noble-Gas-Rubidium Hyperfine Contact Interaction. Physical Review Letters 40 (1978) 391-392.

[22] C.H. Volk, T.M. Kwon, J.G. Mark, Y.B. Kim, and J.C. Woo, Measurement of the Rb-Xe-131 Spin-Exchange Cross-Section in Xe-131 Relaxation Studies. Physical Review Letters 44 (1980) 136-139.

[23] T.E. Chupp, and K.P. Coulter, Polarization of Ne-21 by Spin Exchange with Optically Pumped Rb Vapor. Physical Review Letters 55 (1985) 1074-1077.

[24] Z. Wu, W. Happer, and J.M. Daniels, Coherent Nuclear-Spin Interaction of Adsorbed 131Xe Gas with Surfaces. Phys. Rev. Lett. 59 (1987) 1480-1483.

[25] D. Raftery, H.W. Long, D. Shykind, P.J. Grandinetti, and A. Pines, Multiple-Pulse Nuclear-Magnetic-Resonance of Optically Pumped Xenon in a Low Magnetic-Field. Physical Review A 50 (1994) 567-574.

[26] R. Butscher, G. Wäckerle, and M. Mehring, Nuclear quadrupole interaction of highly polarized gas phase 131Xe with a glass surface. Journal of Chemical Physics 100 (1994) 6923-6933.

[27] T.G. Walker, and W. Happer, Spin-exchange optical pumping of noble-gas nuclei. Review of Modern Physics 69 (1997) 629-642.

[28] D. Raftery, H. Long, T. Meersmann, P.J. Grandinetti, L. Reven, and A. Pines, High-Field NMR of Adsorbed Xenon Polarized by Laser Pumping. Physical Review Letters 66 (1991) 584-587.

[29] M.S. Rosen, T.E. Chupp, K.P. Coulter, R.C. Welsh, and S.D. Swanson, Polarized Xe-129 optical pumping/spin exchange and delivery system for magnetic resonance spectroscopy and imaging studies. Review of Scientific Instruments 70 (1999) 1546-1552.

[30] R. Seydoux, A. Pines, M. Haake, and J.A. Reimer, NMR with a continuously circulating flow of laser-polarized Xe-129. Journal of Physical Chemistry B 103 (1999) 4629-4637.

[31] J.M. Kneller, R.J. Soto, S.E. Surber, J.F. Colomer, A. Fonseca, J.B. Nagy, and T. Pietrass, Continuous-flow optical pumping NMR in a closed circuit system. Journal of Magnetic Resonance 147 (2000) 261-265.

[32] A.L. Zook, B.B. Adhyaru, and C.R. Bowers, High capacity production of > 65% spin polarized xenon-129 for NMR spectroscopy and imaging. Journal of Magnetic Resonance 159 (2002) 175-182.

[33] S. Anala, G.E. Pavlovskaya, P. Pichumani, T.J. Dieken, M.D. Olsen, and T. Meersmann, In situ NMR spectroscopy of combustion. Journal of the American Chemical Society 125 (2003) 13298-13302.

[34] K. Knagge, J. Prange, and D. Raftery, A continuously recirculating optical pumping apparatus for high xenon polarization and surface NMR studies. Chemical Physics Letters 397 (2004) 11-16.

[35] M.G. Mortuza, S. Anala, G.E. Pavlovskaya, T.J. Dieken, and T. Meersmann, Spin-exchange optical pumping of high-density xenon-129. Journal of Chemical Physics 118 (2003) 1581-1584.

[36] L.G. Kaiser, T. Meersmann, J.W. Logan, and A. Pines, Visualization of gas flow and diffusion in porous media. Proceedings of the National Academy of Sciences of the United States of America 97 (2000) 2414-2418.

[37] T. Meersmann, J.W. Logan, R. Simonutti, S. Caldarelli, A. Comotti, P. Sozzani, L.G. Kaiser, and A. Pines, Exploring single-file diffusion in one-dimensional nanochannels by laser-polarized Xe-129 NMR spectroscopy. Journal of Physical Chemistry A 104 (2000) 11665-11670.

[38] L.G. Kaiser, J.W. Logan, T. Meersmann, and A. Pines, Dynamic NMR microscopy of gas phase Poiseuille flow. Journal of Magnetic Resonance 149 (2001) 144-148.

[39] G. Pavlovskaya, A.K. Blue, S.J. Gibbs, M. Haake, F. Cros, L. Malier, and T. Meersmann, Xenon-131 surface sensitive imaging of aerogels in liquid xenon near the critical point. Journal of Magnetic Resonance 137 (1999) 258-264.

[40] T. Meersmann, M. Deschamps, and G. Bodenhausen, Probing aerogels by multiple quantum filtered Xe-131 NMR spectroscopy. Journal of the American Chemical Society 123 (2001) 941-945.

[41] Y. Millot, P.P. Man, M.A. Springuel-Huet, and J. Fraissard, Quantification of electric-field gradient in the supercage of Y zeolites by comparing the chemicl shifts of Xe-131 (I=3/2) NMR. Studies in Surface Sciences and Catalysis 135 (2001).

[42] T. Meersmann, S.A. Smith, and G. Bodenhausen, Multiple-quantum filtered xenon-131 NMR as a surface probe. Physical Review Letters 80 (1998) 1398-1401.

[43] I.L. Moudrakovski, C.I. Ratcliffe, and J.A. Ripmeester, Xe-131, a new NMR probe of void space in solids. Journal of the American Chemical Society 123 (2001) 2066-2067.

[44] H.W. Long, M. Luzar, H.C. Gaede, R.G. Larsen, J. Kritzenberger, A. Pines, and G.P. Crawford, Xenon Nmr-Study of a Nematic Liquid-Crystal Confined to Cylindrical Submicron Cavities. Journal of Physical Chemistry 99 (1995) 11989-11993.

[45] B. Driehuys, G.D. Cates, and W. Happer, Surface Relaxation Mechanisms of Laser-Polarized Xe-129. Physical Review Letters 74 (1995) 4943-4946.

[46] S.R. Breeze, S. Lang, I. Moudrakovski, C.I. Ratcliffe, J.A. Ripmeester, G. Santyr, B. Simard, and I. Zuger, Coatings for optical pumping cells and short-term storage of hyperpolarized xenon. Journal of Applied Physics 87 (2000) 8013-8017.

[47] R.E. Jacob, B. Driehuys, and B. Saam, Fundamental mechanisms of He-3 relaxation on glass. Chemical Physics Letters 370 (2003) 261-267.

[48] M.A. Springuel-Huet, J.L. Bonardet, A. Gedeon, and J. Fraissard, Xe-129 NMR overview of xenon physisorbed in porous solids. Magnetic Resonance in Chemistry 37 (1999) S1-S13.

[49] C.I. Ratcliffe, Xenon NMR. Annual Reports on NMR Spectroscopy 36 (1998) 123-221.

[50] C.J. Jameson, A.K. Jameson, R.E. Gerald_II, and H.-M. Lim, JPCB 101 (1997) 8418-8437.

[51] D. Raftery, and B.F. Chmelka, Xenon NMR Spectroscopy. NMR Basic Principles and Progress 30 (1994) 111-158.

[52] P.J. Barrie, and J. Klinowski, 129Xe NMR as a Probe for the study of microporous solids: a critical review. Progress in NMR Spectroscopy 24 (1992) 91-108.

[53] C. Dybowski, N. Bansal, and T.M. Duncan, Nmr-Spectroscopy of Xenon in Confined Spaces - Clathrates, Intercalates, and Zeolites. Annual Review of Physical Chemistry 42 (1991) 433-464.

[54] D. Raftery, L. Reven, H. Long, A. Pines, P. Tang, and J.A. Reimer, Spin-Polarized Xe-129 Nmr-Study of a Polymer Surface. Journal of Physical Chemistry 97 (1993) 1649-1655.

CHAPTER 3

Hyperpolarized ^{131}Xe NMR Spectroscopy

The results presented in this chapter are being prepared for submission as a journal article with authorship as follows: Karl F. Stupic, Zackary I. Cleveland, Galina E. Pavlovskaya and Thomas Meersmann. Karl F. Stupic and Thomas Meersmann wrote the submission with Zackary I. Cleveland and Galina E. Pavlovskaya providing edits. Karl F. Stupic designed, built, and carried out all the experimental work. Zackary I. Cleveland and Galina E. Pavlovskaya provided useful discussions and technical support.

3.1. Introduction

In contrast to the extensive literature reporting nuclear magnetic resonance (NMR) studies with the spin I = 1/2 isotope ^{129}Xe (110.5 MHz resonance frequency at 9.4 T, 26.4 % natural abundance) [1; 2; 3; 4; 5; 6; 7], the only other NMR active stable isotope of this noble gas, ^{131}Xe, has attracted much less attention since its first reported NMR observation in 1954 [8]. The ^{131}Xe isotope (41.2 MHz resonance frequency at 9.4 T, 21.2% natural abundance) has a spin I = 3/2 and thus possesses a nuclear electric quadrupole moment [9]. The electric quadrupole moment of the xenon nucleus is susceptible to interactions with electric field gradients (EFGs) and serves therefore as a very sensitive probe for distortions of its large surrounding electron cloud [7]. Quadrupolar interactions are the dominating cause for ^{131}Xe nuclear spin relaxation in all phases unless a high concentration of paramagnetic substances is present. Confirming the earlier theory of Staub [10], Brinkmann et al. [11] determined the ^{131}Xe relaxation time (T_1) to be inversely proportional to the gas density ρ with $1/T_1 = \rho \cdot 3.96 \cdot 10^{-2} \text{amagat}^{-1}\text{s}^{-1}$ (1 amagat is the density ρ of the gas under standard conditions). For pure xenon gas at ambient pressure a ^{131}Xe a relaxation time of $T_1 \approx 25$ s can be extrapolated, neglecting relaxation caused by the surrounding container walls.

Warren and Norberg [12; 13] found that frozen natural abundance ^{131}Xe has a longitudinal relaxation time of $T_1 = 390\ s$ at 9 K that decreases monotonically by more than three orders of magnitude with increasing temperature to $T_1 \approx 200$ ms at temperatures close to the melting point (161 K). Upon melting, a fivefold acceleration of the relaxation was observed that slows down with increasing temperature and follows an approximate $T_1 \propto e^{-E_A/RT}$ dependence, with $E_A = 2.68 \pm 0.13\ \text{kJ} \cdot \text{mol}^{-1}$ as the activation

energy for the thermal motion processes in the liquid phase. At 3 MPa and 250 K the relaxation slowed to $T_1 \approx 80$ ms and later work [14] determined $T_1 = 110$ ms at conditions just below the critical point, i.e. 298 K and 5.8 MPa. Fast longitudinal relaxation leads to rapid depolarization and makes usage of hp ^{131}Xe in the condensed phase impractical, except perhaps in the frozen state at temperatures far below that of the liquid nitrogen.

The ^{131}Xe relaxation behavior of xenon dissolved in various solvents has been subject to various experimental NMR spectroscopy and computational studies in the past (see [15] for a review). Longitudinal relaxation in polar solvents is fairly fast ($T_1 < 10$ ms) due to the electric field gradient fluctuations induced by the dipoles. However, even in non-polar solvents, the ^{131}Xe T_1 relaxation times are typically below 50 ms and hence to short for most application of hyperpolarized ^{131}Xe. Rapid signal averaging with thermally polarized ^{131}Xe NMR spectroscopy is the method of choice for these samples. Using thermally polarized ^{131}Xe, NMR studies have been reported in a variety of material sciences related systems such as liquid crystalline phases where ^{131}Xe a triplet caused by interactions of the nuclear quadrupole moment with the anisotropic environment (see [16] for a review), liquid crystals contained in micro channel [17], and in bicells [18]. Other studies extended ^{131}Xe NMR spectroscopy to surfaces at low temperatures [19], porous materials [20; 21; 22; 23; 24], to macro molecules [25] and even to actual xenon compounds [26; 27]. Thermally polarized ^{131}Xe magnetic resonance imaging (MRI) provides a contrast that is sensitive to water adsorbed on aerogel surfaces [28]. Unfortunately, the fast longitudinal relaxation in all these systems does not permit for

meaningful applications of hp ^{131}Xe NMR, unless interfaces or material regions in immediate vicinity to the gas phase were to be studied.

Previously, spin exchange optical pumping (SEOP) with alkali metal vapor [29; 30] was successfully applied to produce hyperpolarized ^{131}Xe, as studied in detail by Volk [31; 32], Happer [33; 34; 35], Pines [36] and Mehring [37] and their respective co-workers. Luo et al. explored ^{131}Xe SEOP using caesium in high magnetic fields [38].

The hp ^{131}Xe is never without a surrounding container wall in these experiments, affecting apparent gas phase ^{131}Xe relaxation behavior. Effects of glass surfaces on the gas phase ^{131}Xe relaxation were measured in the presence of alkali metal vapor in optically detected NMR experiments using SEOP [33; 34; 35; 36; 37]. Moreover, the shape of macroscopic containers with centimeter-sized dimensions can cause an anisotropy in the effective electric field gradient that in turn can produce a small quadrupolar splitting observed in the gas phase [33; 34; 35; 36; 37; 39; 40]. In cylindrical cells an observable splitting, typically in the Hz regime or less, was observed that depends on the aspect ratio of the cell dimensions and the cell orientation within the magnetic field. This splitting is averaged out in cells with spherical symmetry if macroscopic gas diffusion allows the xenon atoms to sample surface segments with different orientations during the relevant NMR timescale. Quadrupolar splitting caused by an anisotropic macroscopic surface orientation can also be observed in NMR tubes with thermally polarized ^{131}Xe NMR spectroscopy [14; 39; 40]. In an intriguing experiment, Mehring and co-workers used optical detection and hp ^{131}Xe in a rotating glass cell to construct a gyroscope that utilizes geometric quantum-phase [41; 42; 43] (see refs. [44; 45] for further theoretical work).

A quadrupolar splitting can also be generated in the bulk gas phase, independent of the presence of surfaces [14]. The high magnetic field $\vec{B}_0$ used in NMR spectroscopy generates an electric field gradient in atoms that are placed into this field. This EFG is always aligned with $\vec{B}_0$ and can lead to a $\left|\vec{B}_0\right|$ dependent ^{131}Xe quadrupolar splitting of a few Hz or less in the bulk gas phase. The EFG is a result of interactions of the external magnetic field $\vec{B}_0$ with the ring current and its resulting magnetization $\vec{M}$ induced by $\vec{B}_0$ into the atomic electron cloud. The resulting quadruplolar splitting shows, therefore, a quadratic dependence upon $\left|\vec{B}_0\right|$ as shown previously [14]. Theory papers following the experimental observation of the quadratic magnetic field dependence of the splitting disagree about the presence of an additional linear term [46; 47]. At the currently available magnetic field strengths, this effect has only be observed by NMR spectroscopy of the noble gas isotope ^{131}Xe, utilizing the unique combination of its large and easily distortable electron cloud, the spherical symmetry of the unbound noble gas atoms, its 'high resolution grade' NMR linewidth in the gas phase and its large nuclear electric quadruple moment at a relatively small spin I = 3/2 value.

The work presented here is concerned with the production of alkali metal free hp ^{131}Xe, a general treatment of hp noble gas polarization in spin I > 1/2, and a study of the effects of gas composition including the presence of water vapor upon the ^{131}Xe quadrupolar splitting.

3.2. Methods and materials

3.2.1. Generating alkali-metal free hp ^{131}Xe

As detailed in the introduction, ^{131}Xe has been previously explored through spin-exchange optical pumping (see introduction), however separation from the alkali metal vapor has never been reported. Separation from the alkali metal vapor is well developed for ^{3}He, ^{129}Xe, (both spin I =1/2) [48; 49] and was accomplished with ^{83}Kr [48; 50; 51; 52; 53; 54; 55; 56], a noble gas isotope with spin I = 9/2. The major obstacle for producing alkali metal free hyperpolarization with spin I > 1/2 noble gases is the nuclear electric quadrupole moment of these isotopes. Quadrupolar interactions caused by gas phase collisions, in van der Waals complexes of noble gas atoms (within the gas phase), and during brief surfaces adsorption of the noble gas atoms typically lead to fast longitudinal relaxation that diminishes the hyperpolarization. Although the spin I = 1/2 isotope ^{129}Xe has a T_1 time on the order of many tens of minutes at near ambient pressures and temperatures [57], T_1 of only 5 s for the quadrupolar ^{131}Xe isotope was obtained in this work at a pressure of 120 kPa (using mixture III at 9.4 T in a 12.6 mm I.D. glass cell). This value is much shorter than $T_1 \approx 25$ s expected from pure gas phase relaxation (see introduction) because of the relatively large surface to volume ratio in the NMR tubes. The fast longitudinal relaxation makes ^{131}Xe more problematic than ^{83}Kr that exhibits T_1 times of around 150 s under similar conditions [58; 59]. This predicament is amplified in continuous flow optical pumping where the hp noble gas is generated outside the superconducting magnet and slowly transported through tubing into the NMR detection cell in the center of the magnet. The tubing has typically a high surface to

volume ratio compared to that of the pump cells and causes fast depolarization that is even further accelerated due to increased relaxation at low magnetic field strengths [54].

Because the T_1 for ^{131}Xe in the solid phase is extremely short (at 77 K a T_1 slightly above 1 s was observed [12]), freezing the hp noble gas at liquid nitrogen temperatures - a methods frequently used for ^{129}Xe separation from ^{4}He gas used in the pumping process [60; 61]- would be completely destructive to the ^{131}Xe polarization. As a consequence, either no helium is used for ^{131}Xe optical pumping or the helium is not removed from the mixture after optical pumping.

In this work, a "batch" or stopped-flow delivery method [53; 54; 55; 56] is used that quickly shuttles the hp ^{131}Xe after 5-10 minutes of SEOP through transfer tubing to the detection cell as shown in Fig. 3.1. SEOP is carried out in cylindrical Pyrex glass cells (length = 125 mm, I.D. = 27 mm) containing 1 to 2 g of rubidium (99.75%; Alfa Aesar, Ward Hill, MA). Illumination of the SEOP cell is provided by a Coherent diode array laser system producing 40 W of circularly polarized light at 794.7 nm. The gas pressure in the pumping cell ranged from 120 kPa to 460 kPa depending on the desired final pressure. Three gas mixtures are used in this work, 5% Xe, 5% N_2, and 90% He (mixture I); 20% Xe, 5% N_2, and 75% He (mixture II); or 93% Xe and 7% N_2 (mixture III), produced from research grade Xe (99.995%, natural abundance), N_2 (99.9997%), and He (99.9999%) (Airgas, Radnor, PA). The ^{131}Xe T_1 relaxation in the 27 mm I.D. SEOP cell at operation temperatures of T = 453K in 0.05 G magnetic fields was not determined. The shuttling is accomplished by pre-evacuation of the detection cell to a pressure of less than 0.1 kPa, followed by pressure equalization between the detection cell and the pumping cell that allows for rapid transfer of hp ^{131}Xe. Loosely packed glass

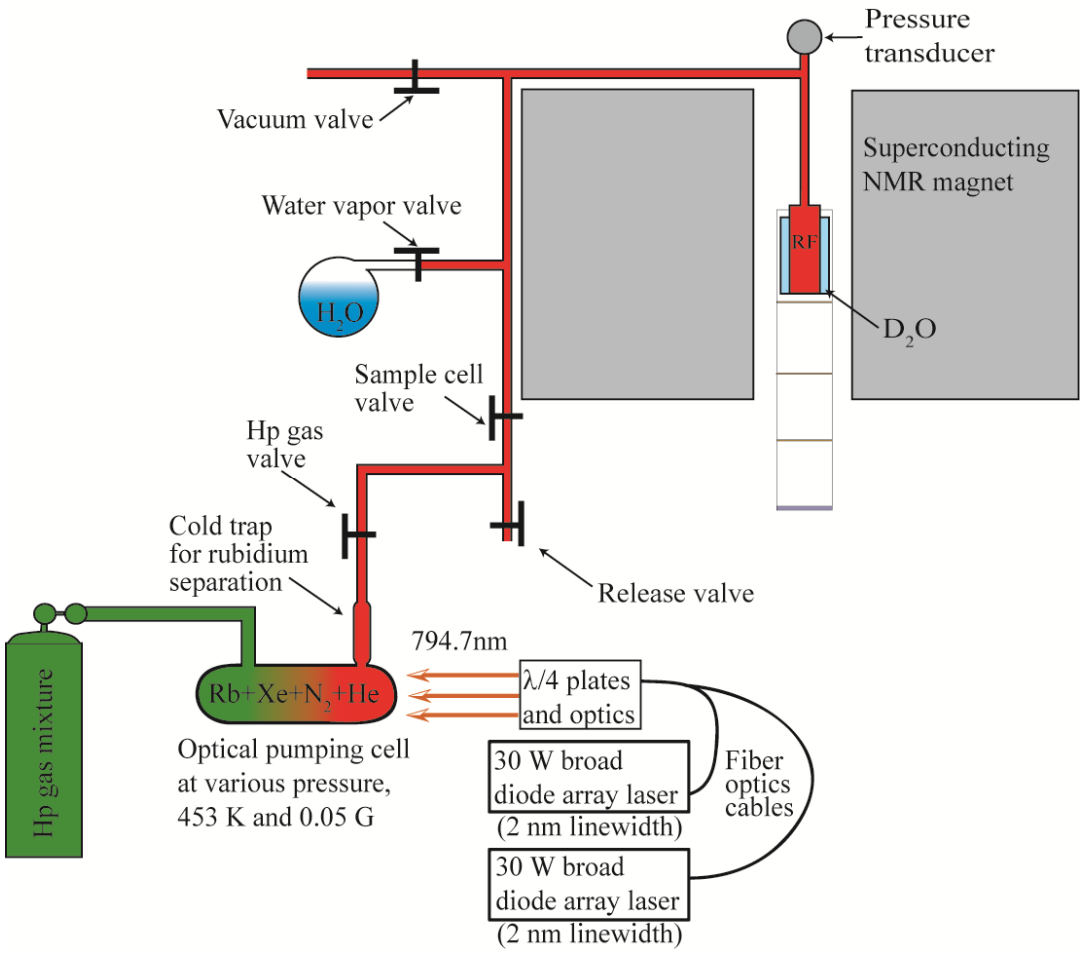

Fig. 3.1: Experimental setup for production and delivery of hp ^{131}Xe. Following polarization build up in the SEOP cell, the hp gas valve is opened allowing hp ^{131}Xe to follow into a two valve section that releases some hp gas to ensure only polarized gas goes to the sample region. After releasing the un-polarized gas, the vacuum valve is closed and the sample cell valve is opened to allow hp ^{131}Xe to be shuttled by pressure equalization into the sample cell for detection. After detection the vacuum valve is opened to re-evacuate the detection cell to < 10 Pa.

wool filters in the transfer line can be applied to remove the alkali metal vapor from the hp ^{131}Xe. For experiments that involve water vapor, two systems were employed. At 9.4 T, hp ^{131}Xe was streamed over 3 mL of water in a storage vessel prior to entering the detection cell. At 14.1 T, a container of water was placed in the system at a junction; this vessel was filled with 10 mL of water, placed under vacuum, and closed off from the rest of the system. After the rest of the system was evacuated following the previous discussed stopped-flow method, the water vessel was opened and allowed the system to be filled with ~3.2 kPa of water vapor, compared to the 1.9 kPa of water vapor for saturation at ambient temperature. The vessel was then closed again and delivery of hp ^{131}Xe gas was carried out.

3.2.2. NMR measurements

Experiments are performed at three field strengths, i.e. at 9.4 T using a Chemagnetics CMX II spectrometer, at 11.7 T with a Varian INNOVA spectrometer, and at 14.1 T with a Chemagnetics Infinity spectrometer. The 11.7 T and 14.1 T systems used a commercial 10 mm broadband probe tuned to ^{131}Xe frequency (41.23 MHz and 49.47 MHz, respectively). Both 11.7 T and 14.1 T were shimmed using an external D_2O standard, also used for the field lock. The D_2O is located between the walls of the outer tube (10.0 mm OD, 9.1 mm ID; Wilmad-LabGlass, Vineland, NJ) and the inner detection tube (Custom-built medium wall NMR 8 mm OD for 11.7 T; 5 mm OD, 4.2 mm ID for 14.1 T; Wilmad-LabGlass, Vineland, NJ) that contains the hp gas. The polarization build up curves and relaxation measurements were collected at 9.4 T in a custom built flow probe tuned to the ^{131}Xe frequency at 32.81 MHz using a 15 mm O.D., 12.6 mm I.D.

Pyrex glass sample tube with no external D_2O for shimming since the quadrupolar splitting did not need to be resolved for this purpose.

T_1 values for hp ^{131}Xe are calculated by nonlinear least-squares fitting of the ^{131}Xe signal intensity as a function of time and number of applied medium flip angle (12.3°) radiofrequency (RF) pulses. All T_1 data are the averages of four replicate measurements and the errors reported are the standard deviations resulting from those replicate measurements. The signal enhancements for hp ^{131}Xe are referenced to the thermal signal obtained from a sample containing 810 kPa of natural abundance Xe at the corresponding field strengths. Quadrupolar splittings, $2\upsilon_Q$, are obtained from the difference of peak position of the satalite transitions obtained by deconvolution of the ^{131}Xe NMR spectrum by multi-peak fittings. Additional parameters obtained from deconvolution are full-width, half-height (FWHH) and peak height. Deconvolution allows for these parameters to be determined without the influence of the other peaks in the spectrum.

3.3. Results and discussion

Fig. 3.2 shows the spectra of ^{131}Xe and ^{129}Xe obtained from thermally polarized and hyperpolarized (hp) samples for comparison. Some differences between the two xenon isotopes become immediately apparent. First, the NMR spectra of the quadrupolar spin I = 3/2 isotope ^{131}Xe display a clear triplet caused by quadrupolar interactions. This is the case for either thermally polarized ^{131}Xe or hp ^{131}Xe spectra, whereas NMR spectra of the spin I = 1/2 ^{129}Xe isotope both result to the expected singlet. The remarkable appearance of a ^{131}Xe triplet in the gas phase is discussed in the introduction and in more detail examined below (see section 3.3.5). A further difference

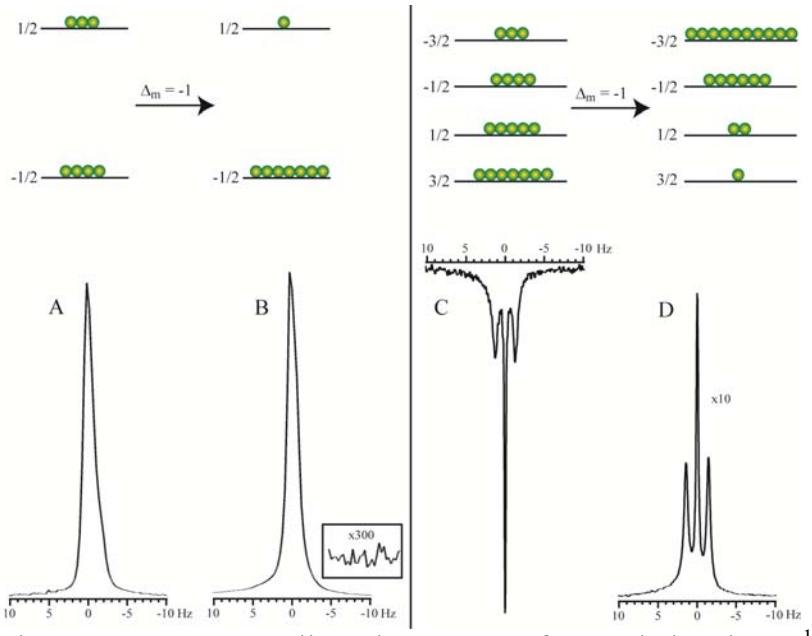

Fig. 3.2: Gas phase NMR spectra collected at 11.7 T of natural abundance ^{129}Xe (A and B) and ^{131}Xe (C and D) with their associated energy levels at thermal, high temperature equilibrium (A and C) and after optical pumping using transition $\Delta_m = -1$ (B and D). (A) ^{129}Xe NMR spectrum of natural abundance xenon at 400 kPa partial pressure of pure xenon and 100 kPa (partial pressure) oxygen using 250 transients; (B) hyperpolarized ^{129}Xe NMR spectrum with 10 kPa (partial pressure) xenon from a 200 kPa, 5% xenon gas mixture after a single stopped-flow delivery; (C) thermal ^{131}Xe NMR spectrum after 1260 transients with a partial pressure of 93 kPa of xenon from a 100 kPa, 93% xenon gas mixture; and (D) hyperpolarized ^{131}Xe NMR spectrum after a single stopped-flow delivery using 10 kPa xenon partial pressure of a 200 kPa, 5% xenon gas mixture. All hyperpolarized spectra are collected with one transient. When correcting for xenon partial pressures and number of transients, enhancements of 33,000 and 1,500 were achieved for ^{129}Xe and ^{131}Xe, respectively. Enhancements of up to 5000 have been observed in other hp ^{131}Xe spectra. The differences in the relative phase are discussed in section 3.3.2.

between the two noble gas spectra shown in Fig. 3.2 is that thermally polarized ^{131}Xe and hp ^{131}Xe are 180° out of phase with respect to each other while both ^{129}Xe spectra posses the same phase. The discrepancy in the relative phases for the two isotopes is caused by the absolute signs of the respective gyromagnetic ratios and explained in section 3.3.2 below. Finally, as discussed in the following section 3.3.1, the linewidth of the ^{131}Xe center transition is substantially narrower than its differentially broadened satellite transitions and the line width found in the ^{129}Xe spectra.

3.3.1. Linewidth of the ^{131}Xe Triplet

A 3.4 fold linewidth ratio is expected from the difference in the gyromagnetic ratios γ for the two xenon isotopes if the dominating cause for linewidth was magnetic field inhomogeneity. The observed linewidth for the ^{131}Xe center transition was 0.3 Hz full width, half height (FWHH), while 1.8 Hz FWHH was observed for the ^{129}Xe spectra. The 0.3 Hz FWHH of the center transition for ^{131}Xe is approximately constant for all the pressures used in this work. For all experiments in Fig. 3.2 the same detection (glass) cell was used and the applied B_0-field shimming (using an external D_2O container) was very similar for all measurements but was not quantified.

Quadrupolar interactions are likely to be responsible for the observed ^{131}Xe differential line broadening of 0.6 Hz FWHH between the ^{131}Xe center transition and the satellite transitions with 0.8 Hz and 0.6 Hz, respectively at higher and lower Hz values (as shown in Fig. 3.2D). Unlike the center transition, the FWHH of the satellite transitions broadens as the pressure increases. Differential broadening of this type can be produced by different relaxation rates for the satellite transition compared to the center

transition [62]. However, this necessitates that the extreme narrowing condition $(\tau_c \omega_0)^2 << 1$ is no longer fulfilled and thus requires long correlation times $\tau_c \geq 10^{-9}$ s that are not expected in the gas phase. Binary collisions in the gas phase are on the order of a few picoseconds and short-lived Xe-Xe van der Waals molecules have life times around 10^{-10} s at 1 amagat xenon density [63]. The correlation times of interactions at the surface are dictated by the averaged adsorption time, τ_a, that is approximately 10^{-10} s for xenon atoms on glass surfaces at 300 K. This value is obtained using $\tau_a = \tau_0 \exp(E / k_B T)$ with the desorption activation energy E = 0.12 eV of xenon on borosilicate glasses [37] and assuming $\tau_0 = 10^{-12}$ s. Although none of the correlation times associated with these events are long enough to cause biexponential relaxation, it is possible however that strong xenon adsorption sites are present on the Pyrex surface. The prolonged correlation times at these locations may lead to a violation of the extreme narrowing condition and thus to differential linebroadening.

An additional hint for surface interactions as the source for the satellite broadening is the differential broadening between the two satellite transitions. Such differential broadening may be the result of paramagnetic – quadrupolar cross correlation that was observed recently by Jerschow and co-workers by ^{23}Na NMR in the presence of paramagnetic contrast agents [64]. The only source for paramagnetism for the spectra in Fig. 3.2 is on the Pyrex surface. Further causes may be CSA-quadrupolar cross-correlation effects during prolonged surface adsorption. Alternatively, the lineshape may be inhomogeneously broadened by differences in EFG experienced by the xenon atoms in various parts of the container that are not averaged by gas diffusion at the gas pressures used.

Although the precise mechanism of the satellite broadening remains speculative thus far, it most likely originates from interaction with the Pyrex surface that are scaled down by exchange with the gas phase where the NMR signal is observed. Note that the scaling also takes place for quadrupolar splitting that is on the order of 6 MHz on a Pyrex surface [65] but that is observed as a few Hz splitting in the gas phase. As discussed in section 3.3.5, the line width and the quadrupolar splitting are significantly affected by the gas composition and overall pressure.

3.3.2. Relative phase and the sign of γ

The 180° phase difference found between the thermally and the hp ^{131}Xe spectra warrants a more detailed explanation. ^{131}Xe is unique among the stable (i.e. non-radioactive) noble gas isotopes because it is the only isotope with a positive gyromagnetic ratio γ. Therefore, according to $E_m = -\gamma m_z \hbar B_0$, the energy level E_m with the highest possible positive *z*-quantum number, i.e. $m_z = + 3/2$, constitutes the ground state for ^{131}Xe, whereas $m_z = - 1/2$ is the ground state for the ^{129}Xe isotope. Indeed, with the exception of ^{131}Xe all NMR active and stable noble gas isotopes, namely ^{3}He, ^{21}Ne, ^{83}Kr and ^{129}Xe have negative gyromagnetic ratios and the respective ground state is the one with the most negative m_z quantum number. The sign of the coherence generated by a 90° pulse ($\hat{H}_{\text{rf-pulse},x} = -\gamma B_0 \hat{I}_x$) depends on the sign of γ and can be important in magnetization transfer or coherence transfer NMR experiments. However the appearance of single-pulse NMR spectra is not affected by the sign of γ except for a 180° phase difference that is difficult to detect between nuclei with different resonance frequencies. However, in SEOP experiments, the relative sign of γ determines how the energy levels

are being pumped by either σ^- or σ^+ circular polarized light. Therefore, it has consequences even for the outcome of a 1-pulse NMR experiments because the γ -sign affects the spin population before the RF-pulse is applied. This effect is depicted in Fig. 3.2 where the energy levels and the spin population are sketched for the two isotopes. In SEOP the sign of Δ_m in the nuclear spin transitions depends only on the choice of either σ^- or σ^+ circular polarized light for the pumping process and is independent of the sign of γ. Although the sign of γ does not affect Δ_m itself, it still has consequences on the population of the energy levels. For ^{129}Xe, the optical pumping transition Δ_m= -1 pumps the higher energy spin state ($m_z = +1/2$) down to the lower energy spin state ($m_z = -1/2$) and thereby causes a reduction in the spin-temperature. In contrast, the same optical pumping transition, $\Delta_m = -1$, pumps low energy spin states in the ^{131}Xe system into higher energy spin states leading to an inverted spin population distribution. The phase difference between the thermally polarized spectrum and the hp spectrum of either isotope is straightforward to compare. When using $\Delta_m = -1$ optical pumping, no phase difference is observed for ^{129}Xe whereas a 180° relative phase shift is observed for ^{131}Xe.

3.3.3. Polarization in spin I > 1/2 nuclei

A general definition of the nuclear spin polarization P is given by Wenckebach [66]:

$$P = Z^{-1}\frac{1}{\hbar I}\left|Tr\left\{\rho\hat{I}_z\right\}\right| \qquad \text{[Eq. 3.1]}$$

written here in slightly different form where Z^{-1} the inverse partition function for the spin *I* system that normalizes its density matrix ρ. The polarization P in Eq. 3.1 is obtained

from the magnetization $|M_z|$ normalized through its maximum possible value of $|M_z| = \hbar I$ at the theoretical limit of T = 0 *K*.

To obtain a simple to use equation for the polarization P, Eq. 3.1 is rewritten as:

$$P_{B_0,T} = \frac{\left| \sum_{m=-I}^{+I} \left(m \cdot e^{m\gamma\hbar B_0 / k_B T} \right) \right|}{\hbar I \cdot \sum_{m=-I}^{+I} e^{m\gamma\hbar B_0 / k_B T}} \qquad \text{[Eq. 3.2]}$$

For $T >> |\gamma| \hbar B_0 / k_B$, the polarization simplifies to:

$$P_{T>>|\gamma|\hbar B_0/k_B} = \frac{|\gamma| \hbar B_0}{3 k_B T} (I+1) \qquad \text{[Eq. 3.3]}$$

The polarization P of a thermally polarized spin I ≥ 1/2 system can be readily calculated using Eq. 3.3 that transforms into the well-known equation $P_{B_0,T}^{I=1/2} = |\gamma| \hbar B_0 / 2 k_B T$ for spin I = 1/2 systems. However, the definition of polarization P is only useful if P is linearly dependent upon the observed signal intensity at any temperature. For instance, this is not the case if one defines the spin polarization of a spin I > 1 systems through the sum of the population differences between two adjacent energy levels [67]. The signal intensity $S_{tp}^{B_0,T}$ caused by thermal polarization (i.e. Boltzmann polarization) of the sample at temperature T and magnetic field B_0 is determined by:

$$S_{tp}^{B_0,T} = A\gamma^2 B_0 \frac{\sum_{m=-I}^{I} \left(C_{I,m}^{+} \right)^2 \left(e^{(m+1)\gamma\hbar B_0 / k_B T} - e^{m\gamma\hbar B_0 / k_B T} \right)}{\sum_{m=-I}^{I} e^{\gamma m \hbar B_0 / k_B T}} \qquad \text{[Eq. 3.4]}$$

with *m* as the z-quantum number of spin *I* and k_B as the Boltzmann constant. Note that Eq. 3.4 describes total integrated signal intensity – i.e. obtained from the sum of all

integrated peaks if a spitting is present. Eq. 3.4 is allowed to depend on the sign of the gyromagnetic ratio in order to accommodate the absolute phase of the signal discussed in section 3.3.2. The transition matrix elements

$$\left(C_{I,m}^{+}\right)^2 = \left|\left\langle I, m+1 \middle| \hat{I}_{+} \middle| I, m \right\rangle\right|^2 \qquad \text{[Eq. 3.5]}$$

are obtained from

$$\hat{I}_{+} \left| I, m \right\rangle = \hbar\sqrt{I\left(I+1\right) - m\left(m+1\right)} \left| I, m+1 \right\rangle \qquad \text{[Eq. 3.6]}$$

All contributions to the signal intensity other than γ, B_0, and the populations of the various quantum states are combined in the coefficient A. At ambient temperatures (i.e. $T >> \left|\gamma\right| \hbar B_0 / k_B$), Eq. 3.4 can be simplified to:

$$S_{tp,\,\text{high T}}^{B_0,T} = \frac{2}{3} \frac{A\gamma^3 \hbar {B_0}^2}{k_B T} \cdot I\left(I+1\right) \qquad \text{[Eq. 3.7]}$$

where the intensity has been allowed once again to be phase sensitive to the sign of γ. Using the signal intensity $S_{tp}^{B_0,T}$ from Eqs. 3.4 or 3.7, the maximum enhancement can be defined as:

$$f_{\max}^{B_0,T} = S_{tp}^{B_0,T \to 0K} \Big/ S_{tp}^{B_0,T} \qquad \text{[Eq. 3.8]}$$

where $S_{tp}^{B_0,T \to 0K}$ is the maximum possible (thermal) signal intensity expected at T = 0 K (phase sensitive):

$$S_{tp}^{B_0,T \to 0K} = A\frac{\gamma^3}{\left|\gamma\right|} B_0 \left(C_{I,m=+I}^{+}\right)^2 = A\frac{\gamma^3}{\left|\gamma\right|} B_0 2I \qquad \text{[Eq. 3.9]}$$

Using Eqs. 3.7, 3.8, and 3.9, the maximum enhancement factor from hyperpolarization (assuming non-thermal equilibrium but still Boltzmann type of population distribution) compared to a thermal signal at ambient temperature is [67]:

$$f_{\max}^{B_0,T>>|\gamma|\hbar B_0/k_B} = \frac{3k_B T}{|\gamma|\hbar B_0 (I+1)} \qquad \text{[Eq. 3.10]}$$

The maximum enhancement factor $f_{\max}^{B_0,T}$ in Eq. 3.10 is the inverse of the polarization P at high temperatures given in Eq. 3.3. Further, $f_{\max}^{B_0,T}$ in Eq. 8 (inserting Eqs. 3.4 and 3.9) is the inverse to the polarization P in Eq. 3.2 at any temperature. As a practical consequence, the polarization P of a hyperpolarized system with arbitrary spin $I \geq 1/2$ can be calculated from the polarization of the thermally polarized system using Eq. 3.3 multiplied with the enhancement factor of the hp signal over the thermal signal.

The thermal polarization for ^{131}Xe at 9.4 T magnetic field strength and 300 K is $P_{9.4T,300K}^{^{131}Xe} = 4.4\times10^{-6}$ and therefore a signal enhancement of $f_{\max}^{9.4T,300K} = 2.27\times10^{5}$ times the thermal equilibrium signal at 9.4 T and 300 K corresponds to 100% polarization. For comparison, the thermal polarization for ^{83}Kr is $P_{9.4T,300K}^{^{83}Kr} = 4.4\times10^{-6}$ ($f_{\max}^{9.4T,300K} = 2.21\times10^{5}$) and for ^{129}Xe is $P_{9.4T,300K}^{^{129}Xe} = 8.9\times10^{-6}$ ($f_{\max}^{9.4T,300K} = 1.12\times10^{5}$).

Fig. 3.3A shows the thermal polarization P (or $\left(f_{\max}^{B_0,T}\right)^{-1}$) at 9.4 T field strength as a function of the temperature T (i.e. spin temperature) for all stable, NMR active noble gas isotopes. Remarkably, the spin temperature dependence of the polarization P is almost identical for all three quadrupolar noble gas isotopes. This is not very surprising in the case of ^{131}Xe and ^{21}Ne since both isotopes have the same spin and similar gyromagnetic ratios. However, in the case of ^{83}Kr the effect of the smaller gyromagnetic ratio (compared to ^{131}Xe and ^{21}Ne) is compensated by the higher spin I = 9/2.

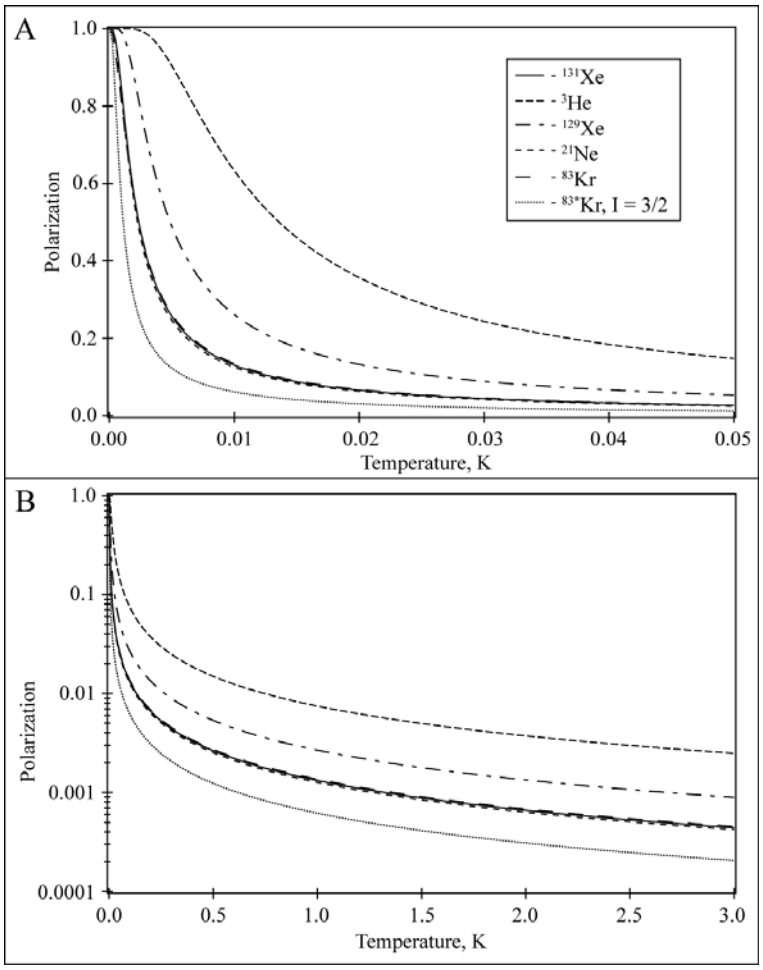

Fig. 3.3: Semi-logarithmic plots of normalized polarization versus temperature obtained from Eq. 2 for the spin active noble gas nuclei and a theoretical Kr isotope with spin I = 3/2. A) Normalized polarization curves as a function of temperature are displayed at temperatures up to 0.05 K, highlighting the deviations in polarization curves at very low temperatures. B) Normalized polarization curves as a function of temperature extended out to 3 K. To reach 1% polarization, the following polarization enhancement compared to the samples at 300 K and 9.4 T needed for each nuclei: 410 for ^{3}He; 1123 for ^{129}Xe; 2373 for ^{21}Ne; 2206 for ^{83}Kr; 2273 for ^{131}Xe; and 4855 for the theoretical Kr isotope For the three quadrupolar isotopes (^{21}Ne, ^{83}Kr, ^{131}Xe) nearly identical polarization curves arise - see section 3.3.3 for details.

3.3.4. Polarization buildup of ^{131}Xe

Using the stopped-flow optical pumping method, ^{131}Xe signal enhancements on the order of 5000 times greater than thermal signal at B_0 = 9.4 T, 150 kPa and 297 K are achieved (approximately 2.2% spin polarization) when using a 5% mixture of xenon (mixture I). The ^{131}Xe polarization build up reaches a steady state relatively quickly compared to other isotopes (^{3}He, ^{129}Xe, ^{83}Kr) due to very short ^{131}Xe T_1 times. Therefore, the fast longitudinal relaxation is not only problematic because of the decay of hyperpolarization but it also limits the spin polarization obtained from the SEOP process.

The time dependence for the hp ^{131}Xe polarization buildup is shown in Fig. 3.4 for the three different mixtures (5, 20, 93% Xe) under 20 W of circularly polarized 794.7 nm laser light. To monitor the ^{131}Xe polarization build-up the magnetic field at the SEOP cell remains switched off initially and the cell is maintained under constant laser illumination at a constant temperature (453 K) and pressure (150 kPa). This procedure allows for a 'starting point' with little or no ^{131}Xe spin polarization present. The magnetic field of a pair of Helmholtz coils was then turned on for incremented time period, t_p, after which the hp ^{131}Xe was transferred to the sample cell where it is detected. At the longest optical pumping times (on the order of several minutes) used for the experiments, mixture I (5% Xe) produced a polarization of 2.19%, mixture II (20% Xe) produced a polarization of 0.45%, and mixture III (93% Xe) produced a polarization of 0.04%.

The time dependent build-up of hyperpolarization is described as [61]:

$$P_{SEOP}^{^{131}Xe} = \frac{\gamma_{se}}{\gamma_{se} + |\Gamma|} \cdot \frac{\gamma_{op(z)}}{\gamma_{op(z)} + \sum_i \kappa_{sd}^i [M_i]} \left(1 - e^{-(\gamma_{se}+\Gamma)t_p}\right) \qquad \text{[Eq. 3.11]}$$

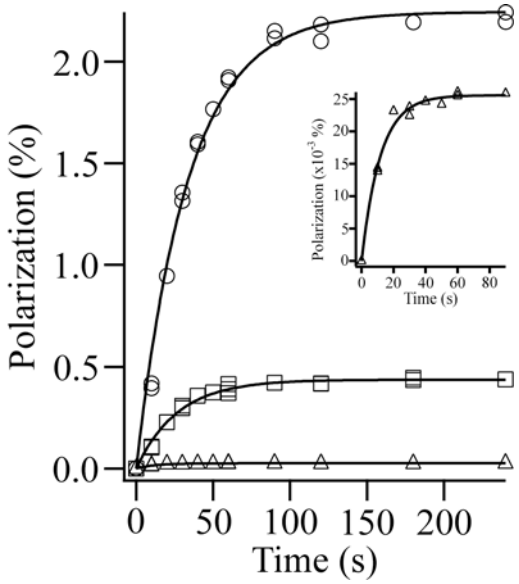

Fig. 3.4: Polarization of hp ^{131}Xe as a function of polarization time t. Optical pumping was carried out for mixtures I (5% xenon, open circle), II (20% xenon, open square), and III (93% xenon, open triangle) under 20 W laser illumination in a pair of Helmholtz coils. Data was collected at 9.4 T after a stopped-flow delivery cycle of duration t. The theoretical curves are obtained by fitting the data to Eq. 3.12. Values for the exponential term, B, for the three mixtures are as follows: mixture I, 0.030 ± 0.001; mixture II, 0.037 ± 0.002; mixture III, 0.085 ± 0.006. Inset: Magnification of polarization versus time plot for mixture III.

where γ_{se} is the Rb–Xe spin exchange rate and Γ the quadrupolar driven fast self-relaxation rate of ^{131}Xe that cannot be treated as negligible as is the case for ^{129}Xe optical pumping [61]. The destruction of Rb spin polarization by collisions with inert gas atoms is described by the sum of the products of the rate constants, κ_{sd}^{i}, with their corresponding gas atom number densities $\left[M_i\right]$. The optical pumping rate per Rb atom, $\gamma_{op}\left(z\right)$, depends on experimental parameters such as laser power, SEOP cell design, and SEOP temperature that are kept constant for all build up experiments reported here. However only a comparison of a reduced form of Eq. 11 was used for fitting of the experimental data since γ_{se}, Γ, and κ_{sd}^{i} are unknown under the SEOP conditions used in this work:

$$P_{SEOP}^{^{131}Xe}\left(t\right) = A\left(1-e^{-Bt_p}\right) \qquad \text{[Eq. 3.12]}$$

The lower the xenon concentration in the gas mixture, the larger the pre-exponential parameter A. The value obtained for A with mixture I is 5 times greater than the value of mixture II and 86 times greater than the value obtained for mixture III. This effect reflects mainly the increased ^{131}Xe self relaxation Γ at higher densities caused by ^{131}Xe-Xe collisions [10; 11]. In comparison, ^{131}Xe-He collisions are much less efficient contributors to the ^{131}Xe self-relaxation. Xenon density dependent changes are also observed in the exponential factor B where mixture III provides the greatest value and is about 3 times greater than mixture I and 2 times greater than mixture II. Again, this can be explained by the increase in the self-relaxation rate constant Γ for the increasing xenon concentrations. The general xenon-density dependence follows that of ^{129}Xe SEOP curves [68] but is much more amplified for ^{131}Xe because of the quadrupolar driven

relaxation. The consequences of these effects on hp ^{131}Xe spectra can also be seen in Fig. 3.5. A distinct decrease in optical pumping efficiency was observed in mixture II and mixture III as the pressure was increased. At 100 kPa pressure only 0.03% polarization was generated for mixture III and the signal was barely observable at higher pressures. At the lowest xenon concentration (mixture I), the pressure had a negligible effect on the SEOP conditions, The likely source for this behavior is that the accelerated relaxation at increasing pressure was compensated by increasing SEOP efficiency due to improvement of $\gamma_{op(z)}$ caused by broadening of the rubidium adsorption line width.

3.3.5. Influence of pressure and concentration on quadrupolar splitting of ^{131}Xe

A dependence of the quadrupolar splitting on both the total pressure of the sample and the gas composition at a field strength of 11.7 T was observed with hp ^{131}Xe. In Fig. 3.5 the hp ^{31}Xe spectra are shown for mixtures I and II with pressures ranging from 100 to 400 kpa and for mixture III with pressures ranging from 25 to 100 kPa. Higher pressures for mixture III could only be detected using signal averaged thermally polarized ^{131}Xe NMR the temperature conditions that would likely differ compared to stopped-flow SEOP experiments and that have not been attempted.

The quadrupolar splitting varies from the smallest observed value of 2.40 Hz at 400 kPa in mixture II to the largest value of 3.05 Hz at 100 kPa of mixture I. The quadrupolar splitting of ^{131}Xe observed in mixture I decreases slightly over the pressure range of 100 to 400 kPa. At 100 kPa the quadrupolar splitting is 3.05 Hz and it decreases to 2.71 Hz at 400 kPa, a change of 0.34 Hz. Mixture II has a greater decrease in

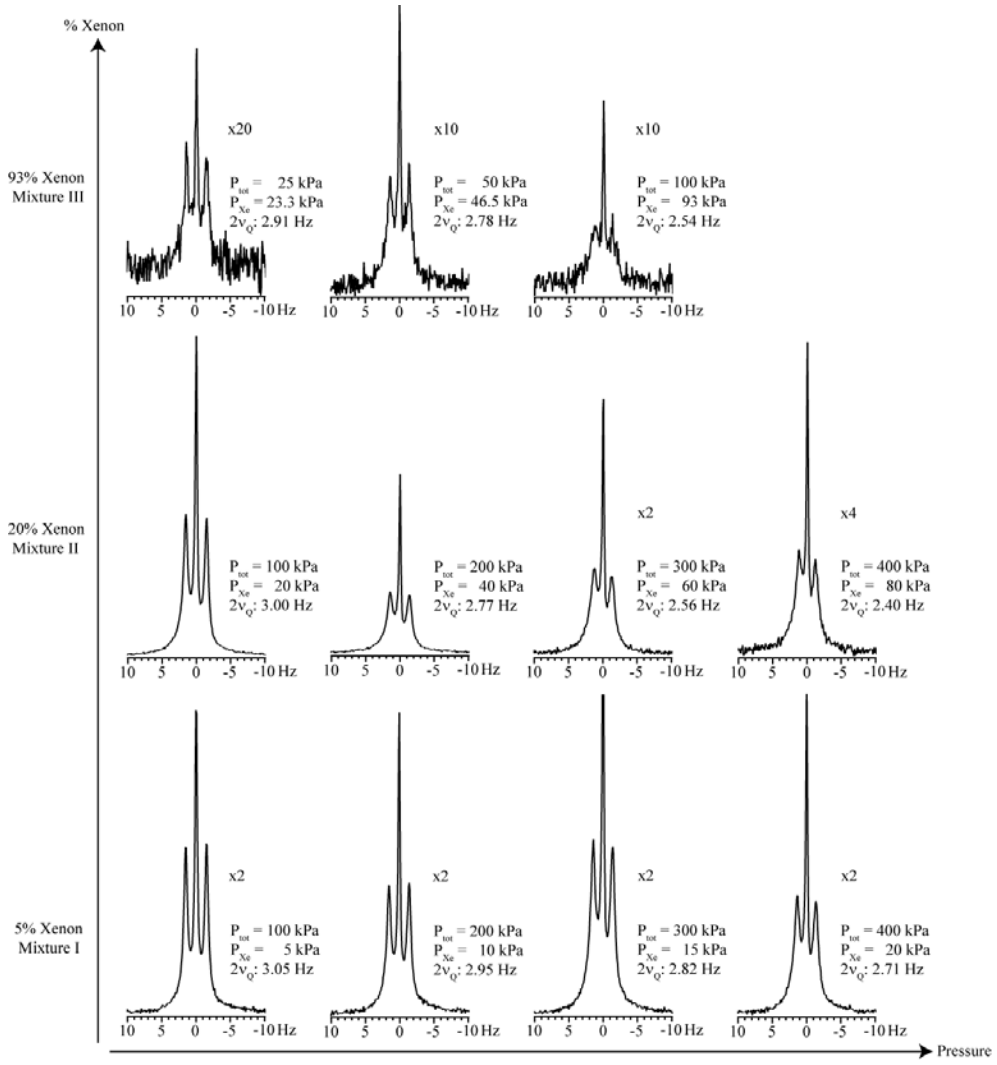

Fig. 3.5: Hp-^{131}Xe gas phase NMR spectra at various compositions and pressures. Hp-^{131}Xe gas was contained in an 8 mm plain NMR tube at 11.7 T field strength and 289 K. Mixtures I, II, and III are represented with associated percentages of xenon along the y-axis and the pressure of the sample cell at the time of detection along the x-axis. Magnification factors are presented beside each spectrum. Mixture I and II (5% and 20% xenon, respectively) are shown from 100 to 400 kPa while mixture III (93% xenon) is shown from 25 to 100 kPa. Pressures (P_{tot}: total pressure, P_{Xe}: xenon partial pressure) are denoted beside each spectrum along with the associated quadrupolar splitting.

quadrupolar splitting than was observed in mixture I over the same pressure range. The quadrupolar splitting was 3.00 Hz at 100 kPa and 2.40 Hz at 400 kPa, for an overall change of 0.60 Hz, almost double the change observed in mixture I. The quadrupolar splitting observed in mixture III decreases from 2.91 Hz at 25 kPa to 2.54 Hz at 100 kPa, a change of 0.37 Hz over the pressure range.

The pressure dependence of the appearance of the ^{131}Xe spectra could be caused by changes in quadrupolar splitting arising from the interactions with the glass surface. Noble gases at ambient temperature will exhibit a very low surface coverage rate, θ, that is dependent on xenon density [Xe] as described by the Henry isotherm. This would predict a constant θ/[Xe] and hence alternating xenon densities will not affect the splitting observed in the gas phase. However, this picture would change in the presence of strong xenon adsorption sites caused by defects on the surface that may experience xenon coverage rates close to saturation under the used pressure conditions. As noted above, strong adsorption sites may also be a possible explanation of the observed differential line broadening.

3.3.6. The effect of H_2O vapor on ^{131}Xe relaxation and quadrupolar splitting.

The addition of co-adsorbing molecules can be used to demonstrate that the gas phase quadrupolar splitting is indeed influenced by changing surface interactions. It was previously shown [28] that the adsorption of water onto an aerogel surface changes the spin-spin relaxation, an effect that was used for MRI contrast. The addition of water vapor had a clear effect on the ^{131}Xe NMR spectra. The ^{131}Xe quadrupolar splitting observed at 14.1 T in a 5 mm NMR tube at 100 kPa and 290 K without the presence of

water vapor is 5.24 Hz (see Fig. 3.6A). Upon the addition of 3.2 Pa of water vapor as described in the experimental section, the splitting is reduced to 4.46 Hz as shown in Fig. 3.6B. The influence of the water vapor is be removed from by evacuating the NMR tube and flushing with dry nitrogen at least three times. Following this treatment, quadrupolar splittings within 0.2 Hz of the values obtained prior to addition of water vapor are observed. The effect that water vapor reduces the xenon interactions with the NMR tube glass wall can also be observed from the ^{131}Xe T_1 relaxation time. The three gas mixtures (I, II, and III) were optically pumped and spin-lattice relaxation times for each mixture were collected in a 15 mm OD Pyrex sample tube at a field strength of 9.4 T and a temperature of 290 K. These data are presented in Table 1 and demonstrates the reduced ^{131}Xe relaxation in the presence of water vapor where the relaxation time (T_1 = 14.0 ± 0.2 s) is extended by almost 50% compared to the dry gas mixture (T_1 = 9.9 ± 0.1 s). The effect of water vapor on ^{83}Kr relaxation was previously demonstrated to have a similar tendency as observed with ^{131}Xe in this work [12; 69; 70; 71].

3.4. Conclusion

Alkali metal vapor free hp ^{131}Xe was generated with a signal enhancement up of 5000 times the thermal equilibrium polarization at 9.4 T field strength and ambient temperatures for dilute xenon mixture. A general equation was derived to describe the thermal spin polarization P at high temperatures for nuclei with any spin I value (Eq. 3). Like in spin I = 1/2 systems, the polarization of hp noble gases with spin I > 1/2 can be calculated by simple multiplication of the thermal high temperature polarization with the

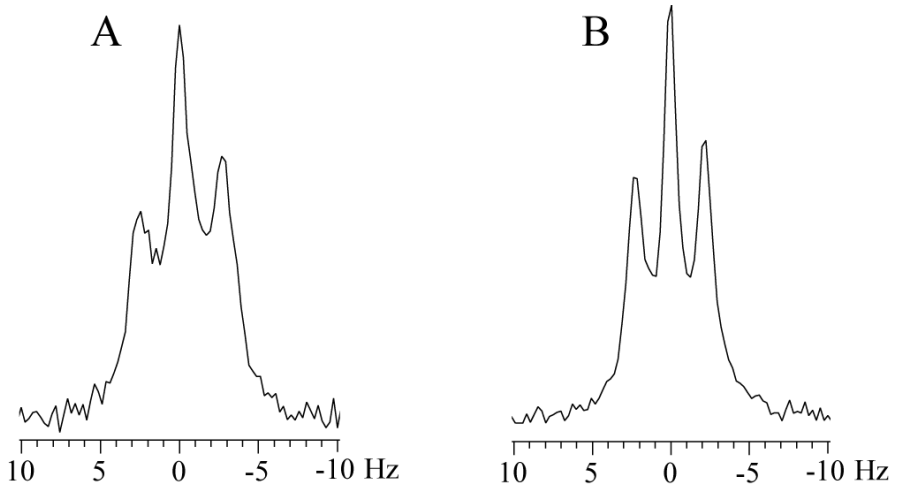

Fig. 3.6: NMR spectra of hp ^{131}Xe (A) and hp ^{131}Xe with water vapor (B) in a 5 mm plain NMR tube. Both spectra were collected at a pressure of 100 kPa of mixture I (5 % xenon). A: The measured quadrupolar splitting is 5.24 Hz in the plain NMR tube. B: The measured quadrupolar splitting is 4.46 Hz under conditions identical to A except for the admission of water vapor (3.2 Pa) prior to hp ^{131}Xe delivery. The data were collected at 14.1 T with ^{131}Xe frequency of 49.47 Hz.

Dehydrated glass tube 5% Xe	Dehydrated glass tube 20% Xe	Dehydrated glass tube 93% Xe	Hydrated glass tube 20% Xe
19.3 ± 0.3 s	9.9 ± 0.1 s	4.7 ± 0.1 s	14.0 ± 0.2 s

Table 3.1: T_1 values for hp ^{131}Xe with various gas compositions on surfaces

T_1 values measured for hp ^{131}Xe at 140 kPa and 9.4 T for gas mixtures I, II, and III. The values reported are the mean and standard deviation of four replicate T_1 measurements.

enhancement factor of the hp signal over the thermal high temperature NMR signal. The maximum ^{131}Xe enhancement obtained in this work corresponds to 2.2 % spin polarization. Because of its positive gyromagnetic ratio, unique for ^{131}Xe among all stable noble gas isotopes, the relative phase between thermal signal and hp signal is opposite to that of any other noble gas isotope. The time dependence of the polarization build up accelerated and the maximum polarization value decreases with increasing xenon partial pressure. Because of xenon partial pressure dependent quadrupolar relaxation, this effect is much more pronounced with ^{131}Xe than with ^{129}Xe. The obtained hp ^{131}Xe signal displays a quadrupolar splitting that is known to be magnetic field - and surface interaction dependent. In this work, an additional xenon partial pressure dependence upon the splitting was found. A possible explanation may be the effects arising from strong adsorption sites on the surface that may also be responsible for the observed differential line broadening between center and satellite transitions. Finally, it was found that the presence of water vapor significantly reduces the observed ^{131}Xe quadrupolar splitting.

The fast ^{131}Xe T_1 relaxation in porous media caused even by only moderate surface to volume ratios makes widespread applications of hp ^{131}Xe NMR spectroscopy and imaging unlikely. However, the quadrupolar splitting in the gas phase is uniquely observed thus far with ^{131}Xe NMR spectroscopy. The disagreement in theoretical work makes the experimental study of the magnetic field dependent contribution to the quadrupolar splitting important. However, the investigation of this effect is masked by surface interactions and by the newly found xenon partial pressure dependence of the quadrupolar splitting. Hp ^{131}Xe may provide better insights into the surface relaxation

processes including those that produce higher rank tensor elements [22] and that may interfere with the observed coherent processes [22; 40]. Further, hp ^{131}Xe may help to provide insights into another probe system, i.e. hp ^{83}Kr (I = 9/2), that has recently been explored as a new MRI contrast agent with potential applications for pulmonary studies [53; 56; 67; 72].

3.5. Acknowledgements

The authors would like to thank Clifford Russell Bowers for stimulating discussions, Michael D. Olsen and Elden G. Burk for sample preparation and construction of experimental apparatus. We also thank Gary E. Maciel and Chris D. Rithner for time on their respective spectrometers used for this work. This materials is based upon work supported by the National Science Foundation under Grant No. CHE-0719423.

References:

[1] C. Dybowski, N. Bansal, and T.M. Duncan, Nmr-Spectroscopy of Xenon in Confined Spaces - Clathrates, Intercalates, and Zeolites. Annual Review of Physical Chemistry 42 (1991) 433-464.

[2] P.J. Barrie, and J. Klinowski, ^{129}Xe NMR as a Probe for the study of microporous solids: a critical review. Progress in NMR Spectroscopy 24 (1992) 91-108.

[3] C.I. Ratcliffe, Xenon NMR. Annual Reports on NMR Spectroscopy 36 (1998) 123-221.

[4] B.M. Goodson, Nuclear magnetic resonance of laser-polarized noble gases in molecules, materials, and organisms. Journal of Magnetic Resonance 155 (2002) 157-216.

[5] D. Raftery, Xenon NMR Spectroscopy. Annual Reports on NMR Spectroscopy 57 (2006) 205-271.

[6] E.J. Ruiz, D.N. Sears, A. Pines, and C.J. Jameson, Diastereomeric Xe chemical shifts in tethered cryptophane cages. Journal of the American Chemical Society 128 (2006) 16980-16988.

[7] M. Hanni, P. Lantto, and J. Vaara, Pairwise additivity in the nuclear magnetic resonance interactions of atomic xenon. Physical Chemistry Chemical Physics 11 (2009) 2485-2496.

[8] E. Brun, J. Oeser, H.H. Staub, and C.G. Telschow, The Nuclear Magnetic Moments of Xe-129 and Xe-131. Physical Review 93 (1954) 904-904.

[9] V. Kello, P. Pyykko, and A.J. Sadlej, Nuclear quadrupole moments of Kr and Xe from molecular data. Chemical Physics Letters 346 (2001) 155-159.

[10] H.H. Staub, Helvetica Physica Acta 29 (1956) 246.

[11] D. Brinkmann, E. Brun, and H.H. Staub, Kernresonanz Im Gasformigen Xenon. Helvetica Physica Acta 35 (1962) 431-436.

[12] W.W. Warren, and R.E. Norberg, Nuclear Quadrupole Relaxation and Chemical Shift of ^{131}Xe in Liquid and Solid Xenon. Physical Review 148 (1966) 402-412.

[13] W.W. Warren, and R.E. Norberg, Multiple-Pulse Nuclear-Magnetic-Resonance Transients of ^{129}Xe and ^{131}Xein Solid Xenon. Physical Review 154 (1967) 277-&.

[14] T. Meersmann, and M. Haake, Magnetic field dependent xenon-131 quadrupolar splitting in gas and liquid phase NMR. Physical Review Letters 81 (1998) 1211-1214.

[15] M. Luhmer, and J. Reisse, Quadrupole NMR relaxation of the noble gases dissolved in simple liquids and solutions - A critical review of experimental data in the light of computer simulation results. Progress in Nuclear Magnetic Resonance Spectroscopy 33 (1998) 57-76.

[16] J. Jokisaari, Nmr of Noble-Gases Dissolved in Isotropic and Anisotropic Liquids. Progress in Nuclear Magnetic Resonance Spectroscopy 26 (1994) 1-26.

[17] H.W. Long, M. Luzar, H.C. Gaede, R.G. Larsen, J. Kritzenberger, A. Pines, and G.P. Crawford, Xenon Nmr-Study of a Nematic Liquid-Crystal Confined to Cylindrical Submicron Cavities. Journal of Physical Chemistry 99 (1995) 11989-11993.

[18] X.X. Li, C. Newberry, I. Saha, P. Nikolaou, N. Whiting, and B.M. Goodson, Interactions between xenon and phospholipid bicelles studied by H-2/Xe-129/Xe-131 NMR and optical pumping of nuclear spins. Chemical Physics Letters 419 (2006) 233-239.

[19] G. Cho, L.B. Moran, and J.P. Yesinowski, Xe-129 and Xe-131 Nmr of Xenon on Silica Surfaces at 77 K. Applied Magnetic Resonance 8 (1995) 549-572.

[20] Y. Millot, P.P. Man, M.A. Springuel-Huet, and J. Fraissard, Quantification of electric-field gradient in the supercage of Y zeolites by comparing the chemicl shifts of Xe-131 (I=3/2) NMR. Studies in Surface Sciences and Catalysis 135 (2001).

[21] I.L. Moudrakovski, C.I. Ratcliffe, and J.A. Ripmeester, Xe-131, a new NMR probe of void space in solids. Journal of the American Chemical Society 123 (2001) 2066-2067.

[22] T. Meersmann, M. Deschamps, and G. Bodenhausen, Probing aerogels by multiple quantum filtered Xe-131 NMR spectroscopy. Journal of the American Chemical Society 123 (2001) 941-945.

[23] Y. Millot, P.P. Man, M. Springuel-Huet, and J. Fraissard, Quantification of Electric-Field Gradients in the Supercage of HY, Steam-Dealuminated Y and Lanthanum-Exchanged Y Zeolites by ^{129}Xe and ^{131}Xe NMR of Physisorbed Xenon Gas. Studies in Surface Science and Catalysis 154 (2004) 1400-1406.

[24] C.F.M. Clewett, and T. Pietrass, Xe-129 and Xe-131 NMR of gas adsorption on single- and multi-walled carbon nanotubes. Journal of Physical Chemistry B 109 (2005) 17907-17912.

[25] G. Saba, M. Casu, and A. Lai, Application of quadrupolar Xe-131-NMR relaxation to the study of macromolecular systems. International Journal of Quantum Chemistry 59 (1996) 343-348.

[26] M. Gerken, and G.J. Schrobilgen, Solution multi-NMR and Raman spectroscopic studies of thermodynamically unstable XeO_4. The first Xe-131 NMR study of a chemically bound xenon species. Inorganic Chemistry 41 (2002) 198-204.

[27] M.A.M. Forgeron, R.E. Wasylishen, M. Gerken, and G.J. Schrobilgen, Solid-state Xe-129 and Xe-131 NMR study of the perxenate anion XeO64-. Inorganic Chemistry 46 (2007) 3585-3592.

[28] G. Pavlovskaya, A.K. Blue, S.J. Gibbs, M. Haake, F. Cros, L. Malier, and T. Meersmann, Xenon-131 surface sensitive imaging of aerogels in liquid xenon near the critical point. Journal of Magnetic Resonance 137 (1999) 258-264.

[29] W. Happer, Optical-Pumping. Reviews of Modern Physics 44 (1972) 169-&.

[30] T.G. Walker, and W. Happer, Spin-exchange optical pumping of noble-gas nuclei. Review of Modern Physics 69 (1997) 629-642.

[31] C.H. Volk, T.M. Kwon, J.G. Mark, Y.B. Kim, and J.C. Woo, Measurement of the Rb-Xe-131 Spin-Exchange Cross-Section in Xe-131 Relaxation Studies. Physical Review Letters 44 (1980) 136-139.

[32] T.M. Kwon, J.G. Mark, and C.H. Volk, Quadrupole Nuclear-Spin Relaxation of Xe-131 in the Presence of Rubidium Vapor. Physical Review A 24 (1981) 1894-1903.

[33] Z. Wu, W. Happer, and J.M. Daniels, Coherent Nuclear-Spin Interaction of Adsorbed ^{131}Xe Gas with Surfaces. Phys. Rev. Lett. 59 (1987) 1480-1483.

[34] Z. Wu, S. Schaefer, G.D. Cates, and W. Happer, Coherent interactions of polarized nuclear spins of gaseous atoms with container walls. Physical Review A 37 (1988) 1161-1175.

[35] Z. Wu, W. Happer, M. Kitano, and J. Daniels, Experimental Studies of Wall Interactions of Adsorbed Spin-Polarized Xe-131 Nuclei. Physical Review A 42 (1990) 2774-2784.

[36] D. Raftery, H.W. Long, D. Shykind, P.J. Grandinetti, and A. Pines, Multiple-Pulse Nuclear-Magnetic-Resonance of Optically Pumped Xenon in a Low Magnetic-Field. Physical Review A 50 (1994) 567-574.

[37] R. Butscher, G. Wäckerle, and M. Mehring, Nuclear quadrupole interaction of highly polarized gas phase ^{131}Xe with a glass surface. Journal of Chemical Physics 100 (1994) 6923-6933.

[38] J. Luo, X. Mao, J. Chen, S. Wang, M. Zhao, L. Fu, and X. Zeng, Frequency-selective laser optical pumping and spin exchange of cesium with Xe-129 and Xe-131 in a high magnetic field. Applied Magnetic Resonance 17 (1999) 587-595.

[39] T. Meersmann, S.A. Smith, and G. Bodenhausen, Multiple-quantum filtered xenon-131 NMR as a surface probe. Physical Review Letters 80 (1998) 1398-1401.

[40] M. Deschamps, I. Burghardt, C. Derouet, G. Bodenhausen, and D. Belkic, Nuclear magnetic resonance study of xenon-131 interacting with surfaces: Effective Liouvillian and spectral analysis. Journal of Chemical Physics 113 (2000) 1630-1640.

[41] S. Appelt, G. Wackerle, and M. Mehring, Deviation from Berry Adiabatic Geometric Phase in a Xe-131 Nuclear Gyroscope. Physical Review Letters 72 (1994) 3921-3924.

[42] S. Appelt, G. Wackerle, and M. Mehring, A Magnetic-Resonance Study of Nonadiabatic Evolution of Spin Quantum States. Zeitschrift Fur Physik D-Atoms Molecules and Clusters 34 (1995) 75-85.

[43] G. Wackerle, S. Appelt, and M. Mehring, Spin-polarized noble gases: A playground for geometric quantum-phase studies in magnetic resonance. Nuclear Instruments &

Methods in Physics Research Section a-Accelerators Spectrometers Detectors and Associated Equipment 402 (1998) 464-472.

[44] J.A. Jones, and A. Pines, Berry dephasing due to diffusion in nuclear quadrupole resonance. Chemical Physics Letters 247 (1995) 215-220.

[45] J.A. Jones, and A. Pines, Geometric dephasing in zero-field magnetic resonance. Journal of Chemical Physics 106 (1997) 3007-3016.

[46] J. F. R. Salsbury, and R.A. Harris, The origin of the magnetic-field dependent quadrupolar splitting. JCP 109 (1998) 8338-8341.

[47] J. Vaara, and P. Pyykko, Magnetic-field-induced quadrupole splitting in gaseous and liquid Xe-131 NMR: Quadratic and quartic field dependence. Physical Review Letters 86 (2001) 3268-3271.

[48] J.R. MacFall, H.C. Charles, R.D. Black, H. Middleton, J.C. Swartz, B. Saam, B. Driehuys, C. Erickson, W. Happer, G.D. Cates, G.A. Johnson, and C.E. Ravin, Human lung air spaces: Potential for MR imaging with hyperpolarized He-3. Radiology 200 (1996) 553-558.

[49] J.P. Mugler, B. Driehuys, J.R. Brookeman, G.D. Cates, S.S. Berr, R.G. Bryant, T.M. Daniel, E.E. deLange, J.H. Downs, C.J. Erickson, W. Happer, D.P. Hinton, N.F. Kassel, T. Maier, C.D. Phillips, B.T. Saam, K.L. Sauer, and M.E. Wagshul, MR imaging and spectroscopy using hyperpolarized Xe-129 gas: Preliminary human results. Magnetic Resonance in Medicine 37 (1997) 809-815.

[50] H. Middleton, R.D. Black, B. Saam, G.D. Cates, G.P. Cofer, R. Guenther, W. Happer, L.W. Hedlund, G.A. Johnson, K. Juvan, and J. Swartz, Mr-Imaging with Hyperpolarized He-3 Gas. Magnetic Resonance in Medicine 33 (1995) 271-275.

[51] H.U. Kauczor, R. Surkau, and T. Roberts, MRI using hyperpolarized noble gases. European Radiology 8 (1998) 820-827.

[52] S. Anala, G.E. Pavlovskaya, P. Pichumani, T.J. Dieken, M.D. Olsen, and T. Meersmann, In situ NMR spectroscopy of combustion. Journal of the American Chemical Society 125 (2003) 13298-13302.

[53] Z.I. Cleveland, K.F. Stupic, G.E. Pavlovskaya, J.E. Repine, J.B. Wooten, and T. Meersmann, Hyperpolarized ^{83}Kr and ^{129}Xe NMR Relaxation Measurements of Hydrated Surfaces: Implications for Materials Science and Pulmonary Diagnostics. Journal of the American Chemical Society 129 (2007) 1784-1792.

[54] Z.I. Cleveland, G.E. Pavlovskaya, K.F. Stupic, C.F. LeNoir, and T. Meersmann, Exploring hyperpolarized ^{83}Kr by remotely detected NMR relaxometry. Journal of Chemical Physics 124 (2006) 044312.

[55] K.F. Stupic, Z.I. Cleveland, G.E. Pavlovskaya, and T. Meersmann, Quadrupolar Relaxation of Hyperpolarized Krypton-83 as a Probe for Surfaces. Solid State Nuclear Magnetic Resonance 29 (2006) 79-84.

[56] G.E. Pavlovskaya, Z.I. Cleveland, K.F. Stupic, and T. Meersmann, Hyperpolarized Krypton-83 as a New Contrast Agent for Magnetic Resonance Imaging. Proceedings of the National Academy of Sciences of the United States of America 102 (2005) 18275-18279.

[57] X. Zeng, E. Miron, W.A. Vanwijngaarden, D. Schreiber, and W. Happer, Wall Relaxation of Spin Polarized Xe-129 Nuclei. Physics Letters A 96 (1983) 191-194.

[58] Z.I. Cleveland, and T. Meersmann, Density-independent contributions to longitudinal relaxation in Kr-83. ChemPhysChem 9 (2008) 1375-1379.

[59] Z.I. Cleveland, and T. Meersmann, Binary-collision-induced longitudinal relaxation in gas-phase Kr-83. Journal of Chemical Physics 129 (2008) 6.

[60] G.D. Cates, D.R. Benton, M. Gatzke, W. Happer, K.C. Hasson, and N.R. Newbury, Laser Production of Large Nuclear-Spin Polarization in Frozen Xenon. Physical Review Letters 65 (1990) 2591-2594.

[61] B. Driehuys, G.D. Cates, E. Miron, K. Sauer, D.K. Walter, and W. Happer, High-volume production of laser-polarized Xe-129. Applied Physics Letters 69 (1996) 1668-1670.

[62] G. Jaccard, S. Wimperis, and G. Bodenhausen, multiple quantum NMR spectroscopy of S=3/2 spins in isotropic phase: A new probe for multiexponential relaxation. Journal of Chemical Physics 85 (1986) 6282-6293.

[63] B.N. Berry-Pusey, B.C. Anger, G. Laicher, and B. Saam, Nuclear spin relaxation of Xe-129 due to persistent xenon dimers. Physical Review A 74 (2006) 063408.

[64] W. Ling, and A. Jerschow, Relaxation-allowed nuclear magnetic resonance transitions by interference between the quadrupolar coupling and the paramagnetic interaction. Journal of Chemical Physics 126 (2007).

[65] R. Butscher, G. Wackerle, and M. Mehring, Nuclear-Quadrupole Interaction of Highly Polarized Gas-Phase Xe-131 with a Glass-Surface (Vol 100, Pg 6923, 1994). Journal of Chemical Physics 102 (1995) 8681-8681.

[66] W.T. Wenckebach, The solid effect. Applied Magnetic Resonance 34 (2008) 227-235.

[67] Z.I. Cleveland, G.E. Pavlovskaya, N.D. Elkins, K.F. Stupic, J.E. Repine, and T. Meersmann, Hyperpolarized Kr-83 MRI of lungs. Journal of Magnetic Resonance 195 (2008) 232-237.

[68] M.G. Mortuza, S. Anala, G.E. Pavlovskaya, T.J. Dieken, and T. Meersmann, Spin-exchange optical pumping of high-density xenon-129. Journal of Chemical Physics 118 (2003) 1581-1584.

[69] D.F. Cowgill, and R.E. Norberg, Spin-Lattice Relaxation and Chemical-Shift of Kr-83 in Solid and Liquid Krypton. Physical Review B 8 (1973) 4966-4974.

[70] D.F. Cowgill, and R.E. Norberg, Pulsed Nmr-Studies of Self-Diffusion and Defect Structure in Liquid and Solid Krypton. Physical Review B 13 (1976) 2773-2781.

[71] D. Brinkmann, and D. Kuhn, Nuclear Magnetic-Relaxation of Kr-83 in Krypton Gas. Physical Review A 21 (1980) 163-167.

[72] Z.I. Cleveland, G.E. Pavlovskaya, K.F. Stupic, J.B. Wooten, J.E. Repine, and T. Meersmann, Detection of Tobacco Smoke Deposition by Hyperpolarized Krypton-83 MRI. Magnetic Resonance Imaging 26 (2008).

CHAPTER 4

Understanding the Influence of High Magnetic Field Strength and Pressure on the Quadrupolar Splitting of ^{131}Xe

This chapter contains data that were collected by Karl F. Stupic at both Colorado State University and Environmental Molecular Sciences Laboratory at Pacific Northwest National Laboratory. Proposals for time and subsequent renewals were written by Karl F. Stupic and edited by Thomas Meersmann. Karl F. Stupic designed and executed the experiments as detailed in those proposals. This chapter was written by Karl F. Stupic and edited by Thomas Meersmann.

4.1. Introduction

Of the many isotopes of the noble gas xenon, only two isotopes are stable, non-radioactive, and observable by nuclear magnetic resonance (NMR) spectroscopy. These two isotopes ^{129}Xe and ^{131}Xe have different nuclear spin states of I = 1/2 and I = 3/2, respectively. Only citing a small portion of the literature, ^{129}Xe has been studied extensively for its use in material [1; 2; 3; 4; 5], medical [6; 7; 8; 9; 10] and fundamental physics [11; 12]; however, ^{131}Xe has been studied to a much lesser extent [13; 14; 15]. A comparison of natural abundances (^{129}Xe: 26.44%, ^{131}Xe: 21.18) and gyromagnetic ratios (^{129}Xe 27.81% of ^{1}H, ^{131}Xe: 8.25% of ^{1}H) shows that ^{131}Xe is a less favorable nuclei for studies involving NMR spectroscopy and imaging. Due to its quadrupolar nuclear spin (I > 1/2), the nucleus of ^{131}Xe has a non-spherical nuclear charge distribution which can be extremely sensitive to electric field gradients (EFGs) caused by adsorption onto surfaces and pore structures in materials, making ^{131}Xe a feasible probe.

Previous work with ^{131}Xe has shown that its properties can be used as a probe for surfaces [13; 14] with examples including studying hydration [15], orientation of surfaces and anisotropic media [16; 17; 18], and temperature [19]. The non-spherical charge distribution of the ^{131}Xe nucleus results in an electric nuclear quadrupolar moment that will interact with EFGs produced by the surrounding electron cloud. Hence, for surfaces, this interaction between the quadrupolar moment and the EFG can lead to an observable splitting of an NMR signal. This splitting is caused by a shifting of the four possible nuclear energy levels (assigned by their respective m_z values 3/2, 1/2, -1/2, -3/2) that breaks the equally spaced separation of the energy levels thus producing three different energy transitions [20; 21]. It is possible to observe in the gas phase the quadrupolar

splitting that was induced by surface absorption of the xenon atom because of exchange between the surface and bulk gas phase over the course of an NMR experiment [13; 19; 22; 23; 24; 25].

The quadrupolar splitting ($2\nu_Q$) of ^{131}Xe also has been observed in the gas phase where the magnetic field strength alone can induce an EFG in the xenon electron cloud that is easy to distort due to its large size. This effect has only been observed with ^{131}Xe thus far as originally reported by Meersmann and Haake [26]. In the original study [26], it was shown that the observed quadrupolar splitting seen in a single 90º pulse is correlated to coherence described by the second ($T_{2\pm1}$) rank element in irreducible tensor representation. This coherence that is reminiscent to anti-phase coherence in scalar coupled spin I =1/2 systems; it is not directly observable, but its effect can be seen indirectly by monitoring the observable coherence described by a first rank ($T_{1\pm1}$) tensor element (reminiscent to 'inphase' coherence). However, small splittings are often masked by line broadening cannot be seen in single pulse experiments. Small splittings can, however, by studied through double quantum filtered (DQF) experiment [26]. By watching the changing in peak intensity throughout a DQF experiment, splitting that would otherwise be obscured by the line width is obtained using sinusoidal fittings. Further, it was shown [26] that even in situations where surface to volume was increased by the addition of capillaries into the sample tube, thereby increasing the surface area and hence the observed quadrupolar splitting arising from the surface, the difference in the observed splitting ($\Delta 2\nu_Q$) at different magnetic fields B_0 was approximately the same as the $\Delta 2\nu_Q$ for sample tubes without capillaries. Therefore, while the splitting, $2\nu_Q$, itself was dependent of the surface area, the surface dependence was not affected by the field

strength. It was therefore concluded that two effects contributed to the observed splitting in the gas phase: (1) a field independent surface induced splitting and (2) a surface independent magnetic field dependent splitting. The latter contribution was considered to be induced by the magnetic field in the gas phase. When considering $2\nu_Q$ as a function of the magnetic field strength, any changes in the observed overall quadrupolar splitting are solely due to the magnetic field induced splitting.

From the data of Meersmann and Haake [26], two theoretical models have been developed for the dependence of the field dependent field induced quadrupolar splitting, one by Salsbury and Harris [27] and another by Vaara and Pyykkö [28]. Both of these models have a similar base assumption, that the quadrupolar splitting dependence on the applied magnetic field has at least a quadratic term based on the quadratic Zeeman effect. This is manifested from diamagnetic interaction of the electronic Hamiltonian for an atom in a magnetic field and in the presence of a nuclear quadrupole. However, the similarities for the two models end at the quadratic term. Salsbury and Harris [27] introduce a linear term for the dependence of the quadrupolar splitting on magnetic field into their model, accounting for coupling of the magnetic field to the nuclear spin. As such, a reduced equation of the model proposed by Salsbury and Harris follows:

$$2\nu_Q \propto aB + cB^2 \qquad \text{[Eq. 4.1]}$$

Salsbury and Harris [27] compare their theory only to the data from liquefied xenon of Meersmann and Haake [26]. Provided the information stated above is accurate, that the surface contribution does not have a field dependence, the theory put forth by Salsbury and Harris [27] would be extendable to all phases of xenon.

Vaara and Pyykkö [28] do not include the linear term used by Salsbury and Harris [27]; instead they include a residual constant contribution from the surface. A reduced equation of the model proposed by Vaara and Pyykkö follows:

$$2\nu_Q \propto aB^2 + C \qquad \text{[Eq. 4.2]}$$

However, this residual constant contribution means that even at zero field strength a quadrupolar splitting would be observed. Additionally Vaara and Pyykkö do not consider the zero field point from Butscher *et al.* [22] for xenon in their model [28], despite Meersmann and Haake utilizing it in their model [26].

In this study, we revisit the aspects of the quadrupolar splitting of ^{131}Xe in the presence of high magnetic fields in an effort to better model interactions of quadrupolar noble gases. Additionally, we explore the dependence of the quadrupolar splitting and other dependences, namely $2\nu_Q$ as a function of pressure. Previously, no dependence of $2\nu_Q$ on pressure dependence was found [26]; however, this contribution has found clear differences in $2\nu_Q$ between pressures varying from 100 to 400 kPa for the container surfaces used in this work. This difference in findings indicates that the pressure dependence may be caused by the surface induced contribution to the quadrupolar splitting. The goal of this research is to show experimental results supporting one of the two previous theories [27; 28]. These pursuits are of particular interest not only for the fundamental understanding of quadrupolar nuclei but also as this understanding could easily be applied to more complex spin systems, such as ^{83}Kr (I = 9/2). In these more complex spin systems the quadrupolar splitting has not yet been observed in the gas

phase, yet the effects may still exist that can be observed using various experiments such as a multiple quantum filtered spectroscopy.

4.2. Methods and Materials

4.2.1. NMR instrumentation and methods

4.2.1.1. Experiments carried out at EMSL/PNNL

Experiments performed at EMSL/PNNL were carried out on a variety of instruments ranging from 11.7 T to 18.8 T. The 11.7 T is a narrow bore magnet (52 mm) equipped with a Varian Infinity CMX console and operated at the ^{131}Xe resonant frequency of 41.23 MHz. The 14.1 T is a narrow bore magnet (52 mm) equipped with a Varian Unity console and operated at the ^{131}Xe resonant frequency of 49.47 MHz. The 17.6 T is a narrow bore magnet (52 mm) equipped with a Varian Inova console and operated at the ^{131}Xe resonant frequency of 61.84 MHz. The 18.8 T is a medium bore magnet (65 mm) equipped with a Varian Inova console, which was operated at the ^{131}Xe 65.96 MHz. All spectra were collected using a single 90° pulse sequence with each spectrum collected with a minimum of 100 transients. All NMR measurements were conducted with the magnet temperature stabilized to 303 K for at least one hour prior to data collection. To ensure the magnet was temperature stabilized, the chemical shift separation of ethylene glycol peaks were observed and temperature was calculated from that separation [29]. To remove any magnetic drifting, the 4 mm OD sample NMR tube containing the xenon gas (described in more detail below) was inserted into an ultra-thin walled 5 mm OD NMR tube (Wilmad-LabGlass, Vineland, NJ) with D_2O to provide the ^{2}D reference signal for the magnetic field lock channel. D_2O also served as a sample to

shim the magnetic field homogeneity to a high enough degree to resolve the ^{131}Xe splitting.

4.2.1.2. Experiments carried out at Colorado State University

Experiments performed at Colorado State University were carried out on a 11.7 T narrow bore magnet (52 mm) equipped with a Varian Inova console and operated at the ^{131}Xe resonant frequency of 41.23 MHz. All spectra were collected using a single 90° pulse sequence and a minimum of 100 transients were collected. Procedures for temperature stability and deuterium lock were carried out at CSU as described in the previous section.

4.2.2. Sample cell preparation

4.2.2.1. Single pressure sample cells

Sample cells for single pressure measurements were prepared by evacuation of a 4 mm NMR tube (Wilmad-LabGlass, Vineland, NJ) at an elevated temperature of 400 K for a minimum of 8 hours. After evacuation the sample containers were filled with research grade Xe gas (99.995%, Airgas, Radnor, PA), which is 21.18% ^{131}Xe by natural abundance. The samples were then pressurized based on a pressure calculated by ideal gas laws to account for differences in ambient temperature at the time of gas filling. These tubs were then frozen in liquid nitrogen and flame sealed to prevent any chance of leaking.

4.2.2.2. Variable pressure sample cells

Sample cells for variable pressure measurements were prepared identically to single pressure sample cells with the exception that instead of being flame sealed these tubes had a stop-cock valve built onto the top of the 4 mm NMR tube that was capable of handling both high and low pressure experiments (ranging from ~ 15 kPa to greater than 400 kPa). Between spectra each sample cell was re-evacuated for 8 hours to maintain sample cell purity.

4.3. Results and discussion

4.3.1. Quadrupolar splitting as a function of magnetic field strength

Individual single pressure NMR samples were placed in up to four different high magnetic field strengths ranging from 11.7 to 18.8 T. As seen in a previous study [26], the quadrupolar splitting ($2\nu_Q$) of ^{131}Xe is observable in the NMR spectrum where the only anisotropy is the container walls of the NMR tube. This contribution can be estimated from [26], by comparison of plain versus capillary filled NMR tubes, to be about 1.5 Hz in 8mm O.D. NMR tubes. This can be seen in Fig. 4.1 where each of the four pressures investigated in this report (101, 202, 306, 402 kPa) are displayed for three different field strengths (14.1, 17.6, 18.8 T). Deconvolution of the quadrupolar splitting present in spectra, collected at each field strength, is presented in Table 4.1.

The data presented in Table 4.1 were collected solely at the EMSL/PNNL facility. When possible each sample cell was observed at each magnet field strength and some sample cells were observed multiple times to ensure reproducibility after ejection and insertion, thereby ensuring minimal error in the measurement. Additionally before and

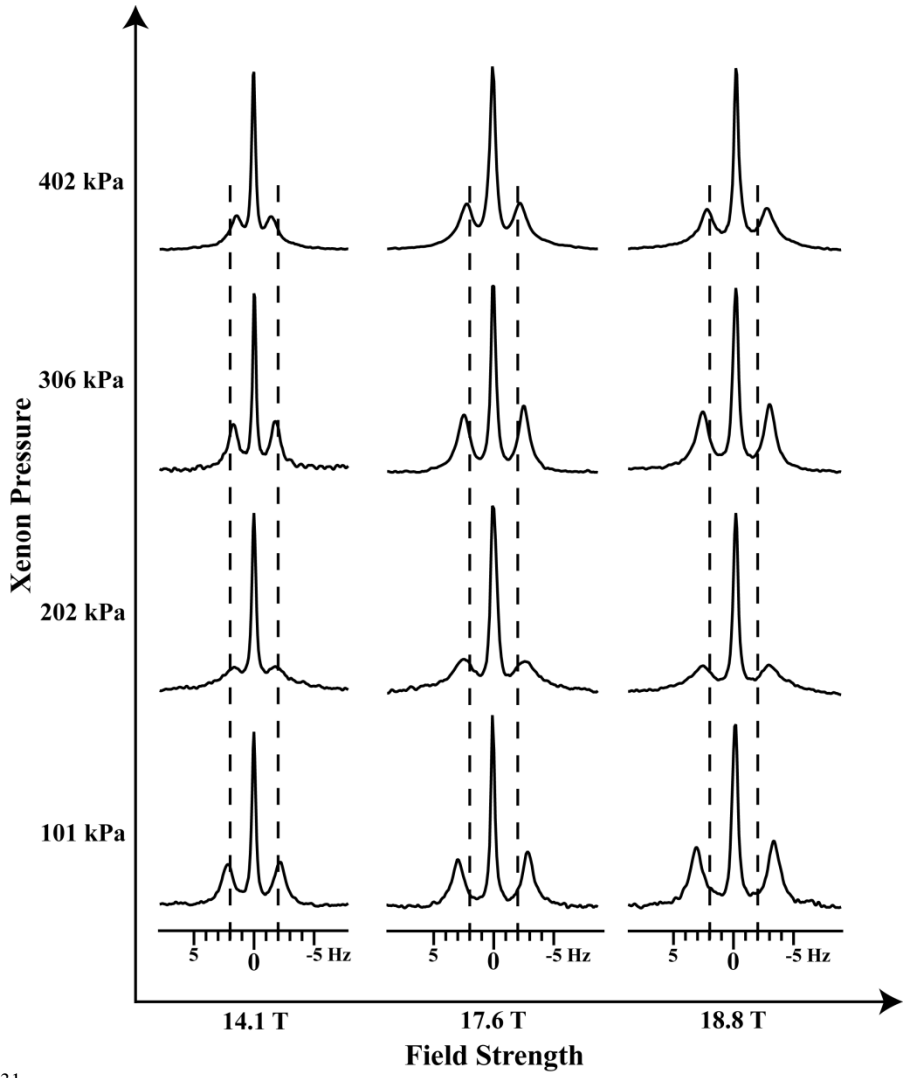

Fig. 4.1: ^{131}Xe spectra for four pressures (101 to 402 kPa) at three different field strengths (14.1, 17.6, and 18.8 T). A dashed line at four Hz spacing is provided as guidance for the eyes to illustrate the effect of pressure and magnetic field on the quadrupolar splitting.

	Field Strengths			
Pressure (Tube #)	11.7 T	14.1 T	17.6 T	18.8 T
101 kPa (1)	3.59 Hz	4.36 Hz	5.85 Hz	6.48 Hz
101 kPa (2)	4.42 Hz	5.10 Hz	6.55 Hz	7.26 Hz
202 kPa (3)	2.53 Hz	3.76 Hz 3.71 Hz	5.41 Hz	5.85 Hz
202 kPa (4)	2.34 Hz	3.55 Hz 3.60 Hz	5.16 Hz	5.68 Hz
306 kPa (5)		3.53 Hz	5.05 Hz	5.64 Hz
306 kPa (6)		3.29 Hz	4.82 Hz	5.51 Hz
306 kPa (7)		3.58 Hz	5.07 Hz	5.52 Hz 5.56 Hz
402 kPa (8)		3.11 Hz	4.61 Hz	5.15 Hz
402 kPa (9)	2.19 Hz	3.01 Hz	4.57 Hz	5.03 Hz 5.08 Hz
402 kPa (10)	2.41 Hz	3.26 Hz 3.25 Hz	4.77 Hz	5.36 Hz
402 kPa (11)		3.24 Hz		

Table 4.1: Quadrupolar splittings of ^{131}Xe in sealed NMR tubes at various field strengths and pressures at 303 K. For samples with replicate runs, both values are reported in the same block. Quadrupolar splitting values are found by a multi-peak deconvolution to extract the center of each satellite peak in a ^{131}Xe NMR spectrum.

after each sample is used, a ^{1}H reference spectrum is collected of ethylene glycol to ensure temperature stability during the measurement [29]. The quadrupolar splitting presented in Table 4.1 is a multi-peak deconvolution to determine the precise position of the center for each satellite peak and thereby the difference in the obtained positions gives the splitting. The data from Table 4.1 and Fig. 4.1 show a decreasing $2\nu_Q$ with decreasing field strength from 18.8 to 11.7 T. Fig. 4.2 illustrates the $2\nu_Q$ based on a single pressure sample (403 kPa, tube #9) and plots it against field strength. The fittings displayed in Fig. 4.2 are taken from the two conflicting theoretically proposed models, using Equ. 4.1 and 4.2 [27; 28]. However, due to the close range of magnetic fields that have been explored to this point, our data do not invalidate either model.

At the present time, there are pending proposals to continue this work and extend the range of magnetic fields down to 7.05 T as well as up to 21.1 T. With the extension of the magnetic field range to these field strengths, it should be possible to better discriminate between the two models. Additionally each model is considered to have a constant included in the fitting to represent the quadrupolar splitting that arises from ^{131}Xe atoms interacting with the surface. This term would be constant in each experiment as the surface induced splitting is field independent and pressure is static inside the sample container (i.e. sealed). It should be noted that the same single pressure sample cell could not be used for variable pressure experiments because it is made from sealed glass tubes. Therefore, data obtained at different pressures are taken from different NMR tubes that may have different surfaces. However as high-resolution NMR tubes are produced with high precision, we assume to a first approximation that the surfaces of all

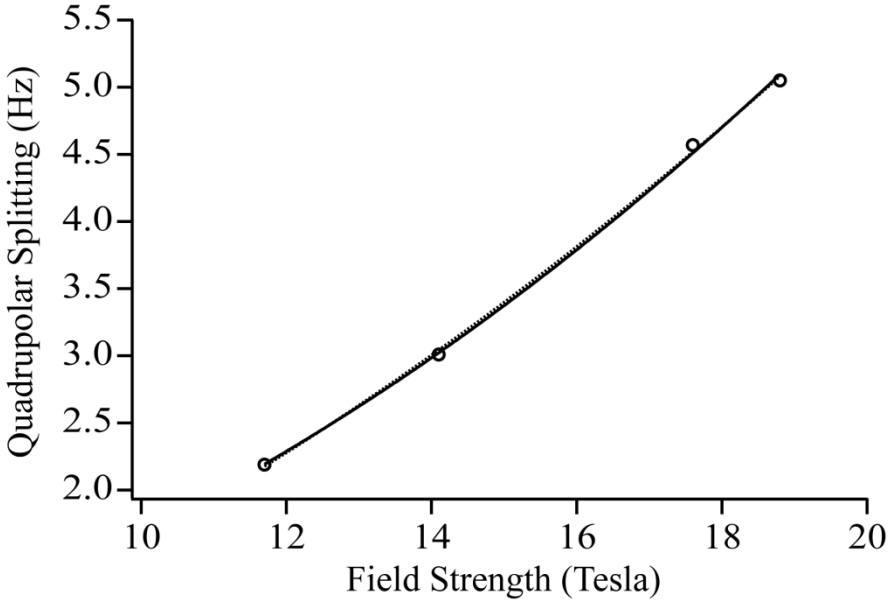

Fig. 4.2: A plot of quadrupolar splitting for sample #9 versus field strength. The solid line is a fitting function consisting only of a quadratic term plus a constant. A dashed line (not visible here due to near perfect overlap) is a fitting function consisting of a quadratic term, a linear term, and a constant. The two fittings are the theoretically proposed models, Equ. 4.1 and 4.2 [27; 28], for the quadrupolar splitting of ^{131}Xe. The constant term is used for the quadrupolar splitting resulting from the surface; this remains constant due to the use of constant pressure over the course of the experiment.

the NMR tubes are similar, thus providing a similar surface induced quadrupolar splitting.

4.3.2. Quadrupolar splitting as a function of pressure

Although the effect of magnetic field on the quadrupolar splitting of ^{131}Xe was expected [26], one unexpected finding is the influence of pressure on the quadrupolar splitting. Careful examination of the position of the outer peaks to the four Hz reference lines displayed in Fig. 4.1 at any field strength shows a distinct trend of greater quadrupolar splitting at lower pressures. Additional analysis of the data in Table 4.1 shows that the pressure of the sample has a distinct influence on the quadrupolar splitting (i.e. at 18.8 T, $2\nu_Q$ for 202 kPa is approximately 5.7 Hz while at 402 kPa $2\nu_Q$ is approximately 5.1 Hz depending on the sample). This influence was not expected and previous literature [26] did not report a pressure dependence.

By plotting the data from Table 4.1 as a function of $2\nu_Q$ versus pressure, one observes that $2\nu_Q$ decreases with increasing pressure (see Fig. 4.3). In Fig. 4.3, a linear fitting has been applied to each field strength data set. Based on the fitting, with allowances for error in measurements, we find that the slope for each line is nearly identical in value and there are significant differences in the intercepts. Below are the equations of fit for each line:

18.8 T: $6.672 - 0.00371 * X$ 17.6 T: $6.123 - 0.00366 * X$ [Eq. 4.3, Eq. 4.4]

14.1 T: $4.539 - 0.00351 * X$ 11.7 T: $3.424 - 0.00311 * X$ [Eq. 4.5, Eq. 4.6]

One immediate issue arises from the data collected at EMSL/PNNL that each NMR tube used, while precision manufactured, could contain different surface defects, anomalies,

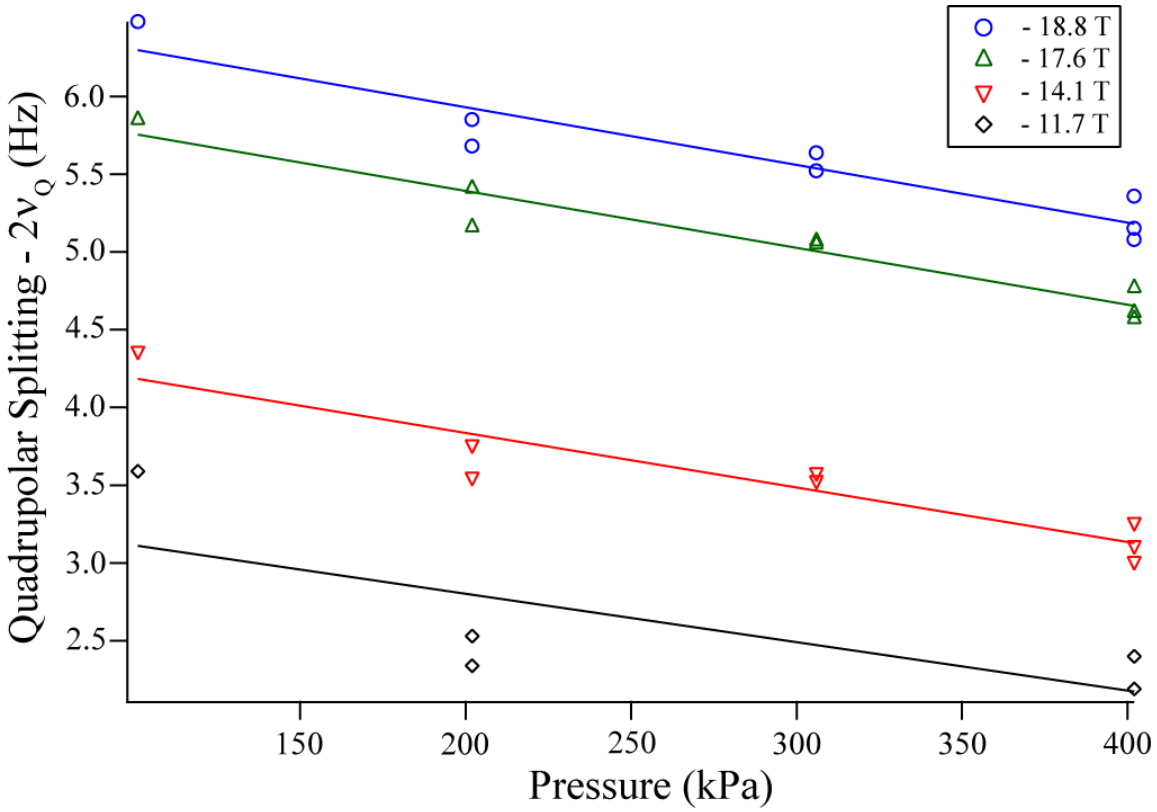

Fig. 4.3: A plot of of data presented in Table 1 with each field strength shown as a function of pressure. Linear fittings were applied to each field strength and displayed as Eq. 4.3 – 4.6 in the text.

and variations. This could lead to each tube having a different quadrupolar surface splitting. A variable pressure sample tube is used at CSU, whereby the surface can be kept constant over the entire pressure range of the experiment. These data are presented in Fig. 4.4 with $2\nu_Q$ plotted against pressure at a field strength of 11.7 T, currently the highest field strength, high resolution NMR spectrometer available at CSU. The linear trend observed in Fig. 4.3 is not observed in Fig. 4.4. It should be noted that the experiments that make up Fig. 4.3 are all single pressure, sealed NMR tubes while the experiments that comprise Fig. 4.4 are from a variable pressure NMR tube. As these are two different tubes, $2\nu_Q$ from the surface of each tube could be different. The influence of the $2\nu_Q$ from the surface could be different at different pressures therefore observation of similar $2\nu_Q$ at high pressures while very different $2\nu_Q$ at lower pressures. A fitting is not applied to Fig. 4.4 as the field strength of 11.7 T is not sufficiently high enough to induce strong quadrupolar splittings at high pressures. However, in Fig. 4.3 a linear fitting is applied to the 11.7 T field strength data based on the observed trend seen in the other field strengths (14.1, 17.6, and 18.8 T). The low splitting values obtained by deconvolution of the spectra at higher pressures contain larger uncertainties and these experiments are worth repeating at higher field strengths such as those available at EMSL/PNNL when resources and time permit.

One way around the low sensitivity and need for signal averaging is to use a non-equilibrium system such as spin-exchange optical pumping whereby high polarization is achieved and can simplify these experiments down to a single acquisition. Previous work (Chapter 3 of this dissertation) has presented data for hyperpolarized (hp) ^{131}Xe produced

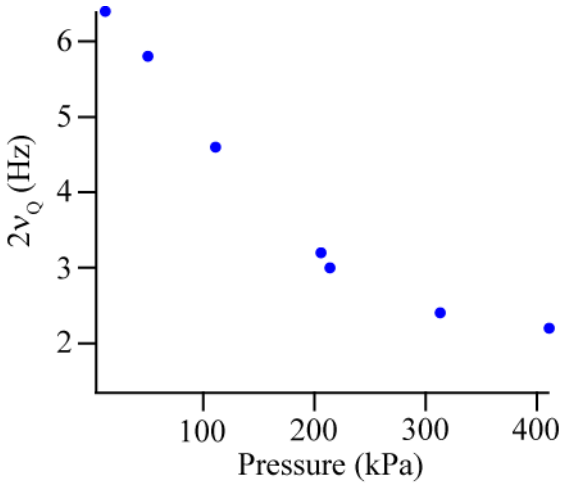

Fig. 4.4: A plot of quadrupolar splitting for ^{131}Xe at 11.7 T recorded at Colorado State University (CSU) as a function of pressure.

by spin-exchange optical pumping, and by plotting $2\nu_Q$ versus total pressure with three different Xe mixtures for a single field strength we obtain Fig. 4.5. A linear dependence of the quadrupolar splitting as a function of pressure is obtained from the fittings of the data presented in Fig 4.5. However, the fittings in Fig. 4.5 are different from the varying field fittings (see Fig. 4.3). Unlike in Fig. 4.3, where each field showed similar slopes with differing intercepts, these data show varying slopes but similar intercepts. The fittings for these three different xenon mixtures are presented below:

$$5\%\ \text{Xe},\ 5\%\ N_2,\ 90\%\ \text{He}:\ 3.1725 - 0.11625 * X \qquad \text{[Eq. 4.7]}$$

$$20\%\ \text{Xe},\ 5\%\ N_2,\ 75\%\ \text{He}:\ 3.1907 - 0.20222 * X \qquad \text{[Eq. 4.8]}$$

$$93\%\ \text{Xe},\ 7\%\ N_2,\ \ 0\%\ \text{He}:\ 3.0313 - 0.49214 * X \qquad \text{[Eq. 4.9]}$$

In considering the equations of fit presented in Eq. 4.3 – 4.9, Eq. 4.7 – 4.9 represent three different xenon concentrations (5, 20, and 93% Xe) at the same field strength (11.7 T). In these three equations of fit, the intercepts are similar in value while the slopes of the lines are different values. Additionally, comparing the intercepts of Eq. 4.7 – 4.9 to Eq. 4.6, data from 11.7 T at PNNL, the intercept found with pure xenon is similar in value to the intercept values of Eq. 4.7 – 4.9. A complication in this similarity is that the NMR tubes used in the two different locations, CSU and PNNL, are different inner dimensions (CSU: 6.4 mm, PNNL: 3.2 mm). This could account for the intercepts not matching to a higher degree. By making the assumption that the observed quadrupolar splitting from the high magnetic field is independent of pressure, this indicates that information regarding this interaction could be contained in the intercept. This assumption is reinforced by the different intercepts obtained in the equations of fit

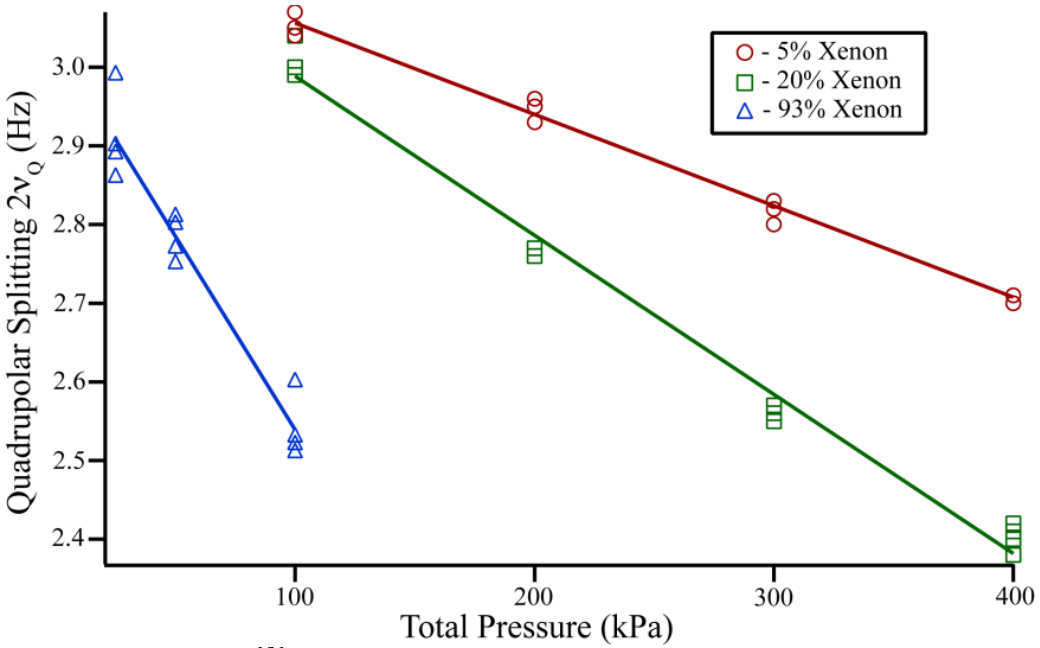

Fig. 4.5: A plot of hp ^{131}Xe gas phase quadrupolar splitting as a function of various compositions and pressures. Hp ^{131}Xe gas was contained in an 8 mm plain NMR tube at 11.7 T field strength and 289 K. Each gas composition is plotted separately and a linear fit was applied to each composition with equations of fit displayed at Eq. 4.7 – 4.9.

for Eq. 4.3 – 4.6 over the four different field strengths (11.7, 14.1, 17.6, and 18.8 T) used in this work.

Using similar reasoning, the change in slope that is observed in Eq. 4.7 – 4.9 for the three different xenon concentrations and the similar values of the slope observed in Eq. 4.3 – 4.6, could provide information regarding interactions of ^{131}Xe on the surface. If the assumption that the observed quadrupolar splitting from the surface is dependent on the xenon concentration; then the slopes of these equations of fit could contain the quadrupolar splitting contribution of ^{131}Xe adsorbed onto the surface. This argument is reinforced by the slope of the lines in Eq. 4.3 – 4.6, which are similar in value over four different magnetic field strengths. The samples used for these experiments are sealed, therefore the surface contribution is held constant with the constant pressure while the magnetic field strength changes. Additionally, as slopes of Eq. 4.3 – 4.6 do not show any dependence on field strength, any information about the magnetic field dependent splitting must not be contained in the slope.

These assumptions should be considered only a first approximation as more data will be needed to fully understand how the contributions from field dependent and surface induced quadrupolar splitting can be studied by plots similar to those of Fig. 4.3 and Fig. 4.5 which plot quadrupolar splitting as a function of pressure. In addition, the $2\nu_Q$ obtained from hp ^{131}Xe requires verification with thermal samples of identical pressures and gas composition as variables such as gas temperature and equalized pressure in the sample region are ignored in this discussion. While more work is needed to verify these hypotheses, the ability to distinguish between interactions on the surface

and in the bulk gas phase, can be used for developing a surface sensitive probe for the fields of material science and material characterization.

4.3.3. Possible model for quadrupolar splitting as a function of pressure

While the data at various pressures, collected from both EMSL/PNNL and CSU (including data from hp ^{131}Xe), have shown that $2\nu_Q$ is a function of pressure, currently there is not a good model to describe the exact mechanism for how the quadrupolar splitting is influenced by pressure. Insight into the behavior of ^{131}Xe at the sample cell walls is provided by Song *et al.* [30] who demonstrated partially restricted diffusion at the sample boundaries using hp ^{129}Xe MRI. This behavior has also been observed in hp ^{3}He [31] and ^{1}H [32; 33; 34]. The restricted diffusion means that atoms on the surface of the container walls may not diffuse back into the center of the sample over the course of the NMR experiment. As seen in the images of [30], the boundary region of the container provides a different signal strength compared to that of the rest of the sample. For ^{131}Xe, this restricted diffusion could be expressed by changes in the quadrupolar splitting. As diffusion is a function of pressure [35], this would change the relative contributions observed from the high field splitting and the surface splitting. For this restricted diffusion to be applicible, the root-mean-squared (RMS) displacement of Xe would have to be smaller than the ID of the sample container. RMS displacement is defined by the equation:

$$X_{RMS} = \sqrt{2D_{Xe}t} \qquad \text{[Eq. 4.10]}$$

Our system X_{RMS} is the RMS displacement in a single dimension, D_{Xe} is the self-diffusion constant for Xe (as given by [35]), and t is the time of the NMR experiment

(500 ms) defined by the Nyquist condition (considered here to be $1/(2*2\nu_Q)$. For reference, the ID of the 4 mm OD NMR tube is 3.2 mm for all experiments done at EMSL/PNNL. A 101 kPa sample, with a corresponding D_{Xe} of 0.0565 cm^2/s given by [30; 35], the RMS displacement is 2.4 mm. This value could be sufficient to average the interactions of the high field and surface splitting in the 4 mm NMR tube, but it could also be partially restrictive.

Using information about the RMS of Xe and partially restricted diffusion, we construct an initial model system to describe the magnetic field dependent ($2\nu_{Q\text{-}HF}$) and the surface induced ($2\nu_{Q\text{-}S}$) quadrupolar splittings broken into two separate contributions. In Fig. 4.6, the contribution from the surface at the lowest pressure (Fig 4.6A) is considered to be everywhere in the sample tube, if the RMS displacement of the Xe atoms is on the order of the tube diameter. Therefore, this considers the splitting in Fig. 4.6A to be the result of the sum from both the surface and the high-field effect splittings. The observed splitting could also have been the difference of the two splittings. This is apparently not the case for the given orientation of the NMR tube surface normal with respect to the magnetic field. However, if the surface normal would be parallel with the magnetic field the sign of the surface splitting would change and would therefore be opposite to the high field splitting. For the moderate pressure (Fig 4.6B), the contribution of the surface is limited to a region closer to the surface as the RMS displacement is significantly less than the diameter of the tube. In this regime, the surface contribution is broadened due to quadrupolar broadening from increased time on the surface or increased surface collisions. For the largest pressure (Fig 4.6C), the main contribution to the observed splitting is from the high field as the surface contribution is significantly

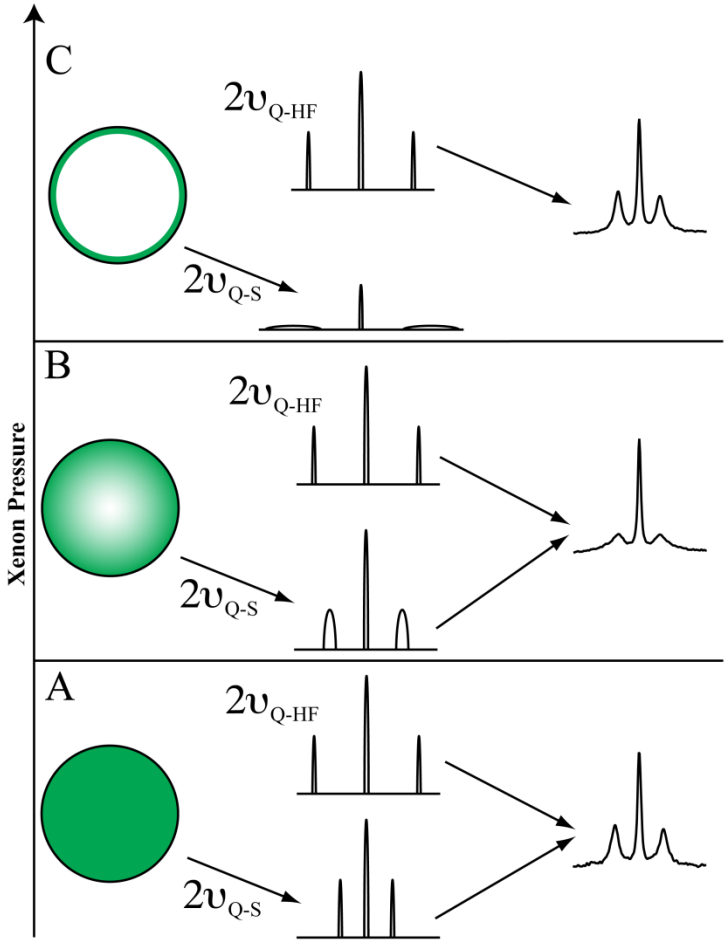

Fig. 4.6: Graphical representation of quadrupolar splitting contributions from the high magnetic field (represented by $2\upsilon_{Q\text{-}HF}$) and the surface (represented by $2\upsilon_{Q\text{-}S}$) with the xenon pressures as follows: (A) low, (B) intermediate, and (C) high (see [30] for restricted diffusion observed by hp ^{129}Xe MRI). For all pressures, the contribution from the high magnetic field is considered to be constant.

suppressed due to broadening. The RMS displacement in these pressure regimes would be small, perhaps 10 % of the diameter or less. Note that the overall splitting observed from xenon in the bulk of the gas phase is no longer the sum of the splitting caused by the field effect and the surface induced splitting. This is because the xenon atoms in contact with the surface do not exchange any longer with the bulk of the gas phase. Any contribution to the observed surface splitting is broadened to a degree that would be hard to detect in the NMR spectrum.

Currently, this is only a hypothetical model and requires further testing. It is worth mentioning that our model ignores the presence of persistent Xe dimers, which could be contributing to the quadrupolar splitting. Work by Saam and coworkers [12; 36] concerning ^{129}Xe relaxation has shown that Xe-Xe dimers are created through a three-body collision and allows for the dimer to survive until a third body contacts and separates them (a van der Waals molecule). Xe-Xe dimers have a lifetime of approximately 115 ps [12] and Chann *et al.* [37] found the persistent dimer concentration to be 1.2% for one amagat of xenon. Given the small concentration and short lifetime of the Xe-Xe dimer, any influence on the quadrupolar splitting of ^{131}Xe should be negligible compared to interactions arising from the surface, the magnetic field strength, and the pressure.

4.4. Conclusion

In this work, we examine several experimental conditions that influence the quadrupolar splitting of ^{131}Xe in the presence of sample container walls. These results are encouraging for furthering development of models that describe quadrupolar noble

gas atom interactions on surfaces. ^{131}Xe (I = 3/2) is the only noble gas nuclei with an observable quadrupolar splitting, which is sensitive to changes in its surrounding environment. Our new model for understanding ^{131}Xe could be applied to other types of spin systems and be applied toward the development of higher order spin systems, such as ^{83}Kr, for use in medical [38; 39; 40] and material science [41; 42] fields. Considering the significant signal enhancements achieved by spin-exchange optical pumping, one application would be the use of DQF MRI with hp ^{83}Kr in lungs, similar to the work of Keinan-Adamsky et al. with ^{2}D in cartilage [43].

4.5. Acknowledgements

This work was funded by the National Science Foundation under Grant No.: CHE-0135082 and CHE-0719423. The authors wish to thank Michael Olsen for construction specialized glassware and used in these experiment, Dr. Christopher Rithner for time on his spectrometer used for this work, as well as Jesse Sears, Dr. Sarah Burton, Dr. Joseph Ford, Dr. Nancy Isern, and Dr. David Hoyt of the Environmental Molecular Sciences Laboratory at Pacific Northwest National Laboratory for the use of their instruments and discussions of the data.

References:

[1] D. Raftery, and B.F. Chmelka, Xenon NMR Spectroscopy. NMR Basic Principles and Progress 30 (1994) 111-158.

[2] D. Raftery, Xenon NMR Spectroscopy. Annual Reports on NMR Spectroscopy 57 (2006) 205-271.

[3] C.I. Ratcliffe, Xenon NMR. Annual Reports on NMR Spectroscopy 36 (1998) 123-221.

[4] C. Dybowski, Zeolite-Included Molecules Studied by Nmr. Journal of Inclusion Phenomena and Molecular Recognition in Chemistry 21 (1995) 113-136.

[5] C.J. Jameson, A.K. Jameson, R.E. Gerald, and H.M. Lim, Anisotropic Xe chemical shifts in zeolites. The role of intra- and intercrystallite diffusion. Journal of Physical Chemistry B 101 (1997) 8418-8437.

[6] B.M. Goodson, Nuclear magnetic resonance of laser-polarized noble gases in molecules, materials, and organisms. Journal of Magnetic Resonance 155 (2002) 157-216.

[7] B.M. Goodson, Using injectable carriers of laser-polarized noble gases for enhancing NMR and MRI. Concepts in Magnetic Resonance 11 (1999) 203-223.

[8] B. Driehuys, G.P. Cofer, J. Pollaro, J.B. Mackel, L.W. Hedlund, and G.A. Johnson, Imaging alveolar-capillary gas transfer using hyperpolarized Xe-129 MRI. Proceedings of the National Academy of Sciences of the United States of America 103 (2006) 18278-18283.

[9] K. Ruppert, J.R. Brookeman, K.D. Hagspiel, and J.P. Mugler, Probing lung physiology with xenon polarization transfer contrast (XTC). Magnetic Resonance in Medicine 44 (2000) 349-357.

[10] A. Cherubini, and A. Bifone, Hyperpolarised xenon in biology. Progress in Nuclear Magnetic Resonance Spectroscopy 42 (2003) 1-30.

[11] G.D. Cates, R.J. Fitzgerald, A.S. Barton, P. Bogorad, M. Gatzke, N.R. Newbury, and B. Saam, Rb Xe-129 Spin-Exchange Rates Due to Binary and 3-Body Collisions at High Xe Pressures. Physical Review A 45 (1992) 4631-4639.

[12] B.N. Berry-Pusey, B.C. Anger, G. Laicher, and B. Saam, Nuclear spin relaxation of Xe-129 due to persistent xenon dimers. Physical Review A 74 (2006) 063408.

[13] T. Meersmann, S.A. Smith, and G. Bodenhausen, Multiple-quantum filtered xenon-131 NMR as a surface probe. Physical Review Letters 80 (1998) 1398-1401.

[14] T. Meersmann, M. Deschamps, and G. Bodenhausen, Probing aerogels by multiple quantum filtered Xe-131 NMR spectroscopy. Journal of the American Chemical Society 123 (2001) 941-945.

[15] G. Pavlovskaya, A.K. Blue, S.J. Gibbs, M. Haake, F. Cros, L. Malier, and T. Meersmann, Xenon-131 surface sensitive imaging of aerogels in liquid xenon near the critical point. Journal of Magnetic Resonance 137 (1999) 258-264.

[16] P. Ingman, J. Jokisaari, and P. Diehl, Kr-83 and Xe-131-Nmr of the Noble-Gases Dissolved in Nematic Liquid-Crystals - Determination of Quadrupole Couplings and Electric-Field Gradients. Journal of Magnetic Resonance 92 (1991) 163-169.

[17] J. Jokisaari, P. Ingman, J. Lounila, O. Pukkinen, P. Diehl, and O. Muenster, Electric-Field Gradients Experienced by the Noble-Gas Isotopes Ne-21, Kr-83 and Xe-131 in Thermotropic Liquid-Crystals. Molecular Physics 78 (1993) 41-54.

[18] H.W. Long, M. Luzar, H.C. Gaede, R.G. Larsen, J. Kritzenberger, A. Pines, and G.P. Crawford, Xenon Nmr-Study of a Nematic Liquid-Crystal Confined to Cylindrical Submicron Cavities. Journal of Physical Chemistry 99 (1995) 11989-11993.

[19] M. Deschamps, I. Burghardt, C. Derouet, G. Bodenhausen, and D. Belkic, Nuclear magnetic resonance study of xenon-131 interacting with surfaces: Effective Liouvillian and spectral analysis. Journal of Chemical Physics 113 (2000) 1630-1640.

[20] A. Abragam, The Principles of Nuclear Magnetism, Oxford University Press, Oxford, UK, 1961.

[21] C.P. Slichter, Principles of Magnetic Resonance, Heidelberg, 1963.

[22] R. Butscher, G. Wäckerle, and M. Mehring, Nuclear quadrupole interaction of highly polarized gas phase 131Xe with a glass surface. Journal of Chemical Physics 100 (1994) 6923-6933.

[23] Z. Wu, W. Happer, and J.M. Daniels, Coherent Nuclear-Spin Interaction of Adsorbed 131Xe Gas with Surfaces. Phys. Rev. Lett. 59 (1987) 1480-1483.

[24] D. Raftery, H. Long, T. Meersmann, P.J. Grandinetti, L. Reven, and A. Pines, High-Field NMR of Adsorbed Xenon Polarized by Laser Pumping. Physical Review Letters 66 (1991) 584-587.

[25] T.M. Kwon, J.G. Mark, and C.H. Volk, Quadrupole Nuclear-Spin Relaxation of Xe-131 in the Presence of Rubidium Vapor. Physical Review A 24 (1981) 1894-1903.

[26] T. Meersmann, and M. Haake, Magnetic field dependent xenon-131 quadrupolar splitting in gas and liquid phase NMR. Physical Review Letters 81 (1998) 1211-1214.

[27] J. F. R. Salsbury, and R.A. Harris, The origin of the magnetic-field dependent quadrupolar splitting. JCP 109 (1998) 8338-8341.

[28] J. Vaara, and P. Pyykko, Magnetic-field-induced quadrupole splitting in gaseous and liquid Xe-131 NMR: Quadratic and quartic field dependence. Physical Review Letters 86 (2001) 3268-3271.

[29] S. Berger, and S. Braun, 200 and more NMR Experiments: A Practical Course, Wiley-VCH, 2004.

[30] Y.-Q. Song, B.M. Goodson, B. Sheridan, T.M.d. Swiet, and A. Pines, Journal of Chemical Physics 108 (1998) 6233-6239.

[31] B. Saam, N. Drukker, and W. Happer, Edge enhancement observed with hyperpolarized He-3. Chemical Physics Letters 263 (1996) 481-487.

[32] P.T. Callaghan, A. Coy, L.C. Forde, and C.J. Rofe, Diffusive Relaxation and Edge Enhancement in NMR Microscopy. Journal of Magnetic Resonance Series A 101 (1993) 347-350.

[33] T.M. Deswiet, and P.N. Sen, Decay of Nuclear Magnetization by Bounded Diffusion in a Constant Field Gradient. Journal of Chemical Physics 100 (1994) 5597-5604.

[34] T.M. Deswiet, Diffusive Edge Enhancement in Imaging. Journal of Magnetic Resonance Series B 109 (1995) 12-18.

[35] P.W.E. Peereboom, H. Luigjes, and K.O. Prins, An NMR Spin-Echo Study of Self-Diffusion in Xenon. Physica A 156 (1989) 260-276.

[36] B.C. Anger, G. Schrank, A. Schoeck, K.A. Butler, M.S. Solum, R.J. Pugmire, and B. Saam, Gas-phase spin relaxation of Xe-129. Physical Review A 78 (2008).

[37] B. Chann, I.A. Nelson, L.W. Anderson, B. Driehuys, and T.G. Walker, Xe-129-Xe molecular spin relaxation. Physical Review Letters 88 (2002) 113201.

[38] Z.I. Cleveland, K.F. Stupic, G.E. Pavlovskaya, J.E. Repine, J.B. Wooten, and T. Meersmann, Hyperpolarized ^{83}Kr and ^{129}Xe NMR Relaxation Measurements of Hydrated Surfaces: Implications for Materials Science and Pulmonary Diagnostics. Journal of the American Chemical Society 129 (2007) 1784-1792.

[39] Z.I. Cleveland, G.E. Pavlovskaya, K.F. Stupic, J.B. Wooten, J.E. Repine, and T. Meersmann, Detection of Tobacco Smoke Deposition by Hyperpolarized Krypton-83 MRI. Magnetic Resonance Imaging 26 (2008).

[40] Z.I. Cleveland, G.E. Pavlovskaya, N.D. Elkins, K.F. Stupic, J.E. Repine, and T. Meersmann, Hyperpolarized Kr-83 MRI of lungs. Journal of Magnetic Resonance 195 (2008) 232-237.

[41] K.F. Stupic, Z.I. Cleveland, G.E. Pavlovskaya, and T. Meersmann, Quadrupolar Relaxation of Hyperpolarized Krypton-83 as a Probe for Surfaces. Solid State Nuclear Magnetic Resonance 29 (2006) 79-84.

[42] Z.I. Cleveland, G.E. Pavlovskaya, K.F. Stupic, C.F. LeNoir, and T. Meersmann, Exploring hyperpolarized ^{83}Kr by remotely detected NMR relaxometry. Journal of Chemical Physics 124 (2006) 044312.

[43] K. Keinan-Adamsky, H. Shinar, and G. Navon, The effect of decalcification on the microstructure of articular cartilage assessed by H-2 double quantum filtered spectroscopic MRI. Magnetic Resonance Materials in Physics Biology and Medicine 18 (2005) 231-237.

CHAPTER 5

Magnetic Field Dependence of Hyperpolarized ^{129}Xe and ^{83}Kr Longitudinal Relaxation in the Presence of Metal Surfaces and Oxygen.

The results presented in this chapter are being prepared for publication as a journal article. Karl F. Stupic conducted all experiments presented in this chapter along with experimental setup construction at Colorado State University. Karl F. Stupic wrote the manuscript and Thomas Meersmann edited it.

5.1 Introduction

Since its first report five years ago [1], hyperpolarized (hp) ^{83}Kr has been utilized in a variety of nuclear magnetic resonance (NMR) and magnetic resonance imaging (MRI) applications. Hp ^{83}Kr has been applied to studies of materials and surface chemistry/composition [2; 3; 4], gas phase relaxation [5], and to imaging of tobacco smoke deposition [6] and small animal lungs [7]. These studies are possible because the high spin polarization generated through alkali metal spin-exchange optical pumping (SEOP) leads to many orders of magnitude increase in signal enhancement [8; 9] compared to thermal polarization. A disadvantage of ^{83}Kr (I = 9/2) is that it possesses a nuclear electric quadrupole moment that dominates the longitudinal relaxation (T_1). During gas phase collisions and surface interactions, distortions in the electron cloud generate electric field gradients (EFGs) which couple to the quadrupole moment causing the relaxation. Thus, the relaxation times observed in ^{83}Kr [2; 3; 10] are in general shorter than relaxation times observed for I = 1/2 noble gas nuclei, ^{3}He and ^{129}Xe [11; 12; 13; 14; 15], in the gas phase.

^{3}He and ^{129}Xe have long relaxation times in the gas phase, on the order of hours. However, in the presence of paramagnetic species (e.g. oxygen), these relaxation times are reduced to tens of seconds [16; 17; 18; 19]. The sensitivity of ^{3}He and ^{129}Xe T_1 values to oxygen has been exploited to study oxygen partial pressures [20] and blood oxygenation levels [21; 22]. Whereas the sensitivity to oxygen of ^{3}He and ^{129}Xe is useful, it also obscures surface sensitive relaxation in studies conducted in the presence of oxygen (i.e. *in vivo* lung tissue). ^{129}Xe has a large chemical shift range (≈300 ppm) that is sensitive to its environment and provides information on changes in surface chemistry

or structure. ^{3}He possesses no chemical shift range, but its resonant frequency is higher than ^{129}Xe and ^{83}Kr, providing better resolution in imaging experiments. ^{83}Kr, with its quadrupolar interaction dominated relaxation, does not experience the same reduction in T_1 as ^{3}He and ^{129}Xe in the presence of oxygen. A 16% reduction in T_1 for ^{83}Kr in the presence of oxygen and canine lung tissues has been observed [1]. The weak interaction of ^{83}Kr when in the presence of oxygen still allows the relaxation to be dominated by adsorption on surfaces. Therefore ^{83}Kr can provide surface sensitive information in the presence of oxygen that would be obscured in ^{3}He and ^{129}Xe studies, making hp ^{83}Kr a complementary tool to I = 1/2 nuclei.

In this work, the relaxation behavior of hp ^{129}Xe and ^{83}Kr, generated by SEOP, is studied in the presence of metal surfaces and oxygen at various magnetic field strengths. These data will be useful in developing storage and transport systems for hp noble gases, as prolonged relaxation is desired in these systems. Additionally, understanding relaxation on paramagnetic surfaces is important when administering hp noble gases for *in vivo* studies. Because radiofrequencies (RF) cannot penetrate metal, we employ remote NMR detection, a tool that allows for the spatial and temporal separation of the system of interest from the detection coil of the NMR probe. To achieve this we use rapid pressure equalization to move hp noble gases from the SEOP cell to the storage cell (i.e. the system of interest). This allows relaxation to occur for a predetermined period of time, and then allows the detection coil to observe the different decayed signals as a function of storage time. Similar procedures have been used previously [8; 23] and allow for a unique opportunity to study materials that otherwise would not be accessible by standard NMR methodologies. This remote NMR detection methodology can be

extended to non-magnetic metal samples and to oxygen/hp noble gas mixtures used to explore relaxation behavior. The latter is applicable to *in vivo* studies of living animals where oxygen must be supplied with the hp gas.

In this work, measured T_1 values for ^{129}Xe and ^{83}Kr range from as short as 14 s for ^{129}Xe with oxygen to as long as 178 s for ^{83}Kr on an untreated glass surface, depending on the surface or presence of oxygen. On stainless steel surfaces, the T_1 times of ^{129}Xe are 40 – 60 % shorter than those of ^{83}Kr at various field strengths. In addition, the T_1 times for ^{83}Kr in the presence of a breathable mixture of oxygen (20 %) are found to be field dependent (92 – 130 s) over the magnetic field strengths explored in this work, whereas the T_1 of ^{129}Xe is found to be field independent and approximately an order of magnitude shorter than the T_1 of ^{83}Kr.

5.2 Methods and materials

5.2.1 Spin-exchange optical pumping of noble gases

Spin-exchange optical pumping (SEOP) of ^{129}Xe and ^{83}Kr is performed in untreated, cylindrical Pyrex cells (ID = 24 mm, length = 125 mm) as described previously [3; 8; 24]. The three gas mixtures used in this work are composed of research grade gases (Airgas, Randor, PA). Each mixture contains either 5% Xe (99.995% pure), 5% Kr (99.995% pure) or 20% Kr, with 5% N_2 (99.9997% pure) and a balance of helium (99.9999% pure). Each SEOP cell contains ~1 g of rubidium (99.75% pure, Alfa Aesar, Ward Hill, MA), and is housed in a quartz and aluminum oven to maintain a constant temperature across the cell (393 ± 5 K for ^{129}Xe, 438 ± 5 K for ^{83}Kr). Unpolarized light generated by two fiber coupled Coherent FAP diode-array laser systems (2 nm linewidth, 30 W each; Santa Clara, Ca, USA), passes through polarization optics targeting the front

of the SEOP cell with a final power of approximately 42 W. A second laser system, a Spectra-Physics Comet diode array laser module (0.2 nm linewidth, 35 W; Santa Clara, Ca, USA), passes through polarization and telescoping optics, targeting the back of the SEOP cell with a final power of approximately 27 W. The magnetic field needed for SEOP is provided by the fringe field of a superconducting magnet, ~ 0.05 T across the SEOP cell. Pressure in the SEOP cell is maintained between 255 – 260 kPa for measurements on all surfaces with the exception of a pressure between 215 – 220 kPa for measurements with molecular oxygen already in the storage volume. Rb vapor is separated from hp gas mixtures by an air-cooled trap situated at the outlet of the SEOP cell, providing Rb free hp gas to the detection and storage cells.

5.2.2 NMR measurements

Experiments are performed at 15.4 MHz with a Chemagnetics CMX II spectrometer and a 9.4 T wide-bore (89 mm) superconducting magnet for detection. A wide-bore (89 mm) magnet (capable of 4.7 T) is used to produce varying field strengths of 0.5, 1.0, 2.0, and 3.0 T, which is directly measured by a gauss meter to ensure less than 3% deviation in the magnetic field over a region greater than the storage cell. Fig. 5.1A shows the experimental setup for all remotely detected NMR measurements in this work. Displayed in Fig. 5.1B is the experimental sequence used for all measurements, where the hp gas is delivered by pressure equalization to both the detection cell and the storage cell. The storage cell had a target pressure of 125 kPa for all experiments in this work. A 90º RF pulse provides a calibration measurement to ensure any change in SEOP efficiency is accounted for, shown as t = 0 s in Fig. 5.2A. Immediately after the calibration

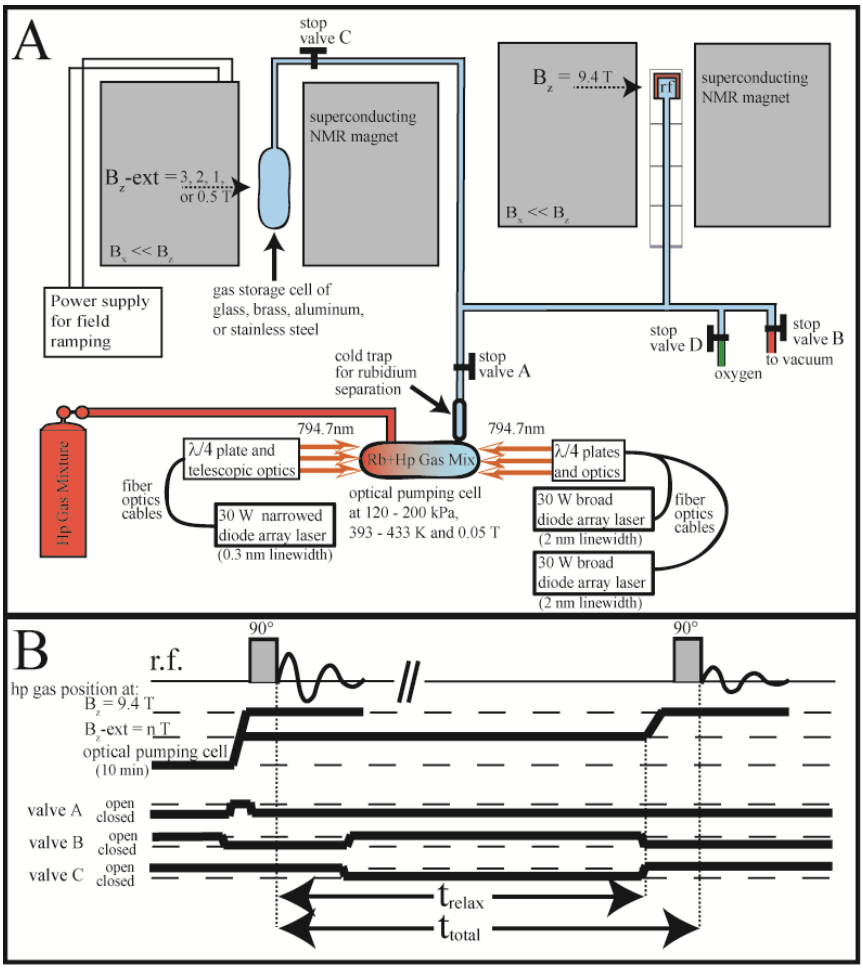

Fig. 5.1: Experimental system and procedure used for production and delivery of hp noble gases. A) Drawing of the experimental system used in a stopped-flow configuration for remotely detected relaxometry with various magnetic field strengths. B) Diagram of stopped-flow experiment used for remotely detected relaxometry with a second superconducting magnet providing the field strength being studied. Hp noble gas is moved between the storage cell and the detection cell via pressure equalization. Shown is the RF pulse sequence, the position of the hp noble gas within the different magnetic fields, and the status of the gas valves. Not shown is the introduction of molecular oxygen to the storage cell prior to hp gas delivery; this is described in the methods and materials section.

measurement, a valve (Valve C in Fig. 5.1A) separates the storage cell from the detection cell so the detection cell can be cleared and placed under vacuum. Following an incremented length of time, t, the vacuum system clearing the detection cell is separated by a valve (Valve B in Fig. 5.1A) and the valve between the detection and storage cell (Valve C in Fig. 5.1A) is opened, delivering hp gas back to the detection volume. This hp gas is in contact with a number of different materials or additional gaseous species and experiences a degree of decay observed in the second RF pulse, shown as t = 120 s in Fig. 5.2A. A pressure gauge (DV100, Vacuum Research, Pittsburgh, Pa, USA) monitors the pressure at all times in the detection cell for both calibration and decay measurement pulses. Prior to data fitting, the integrated signal intensity of the decay measurement is corrected by factors, including pressure and SEOP efficiency, before being normalized to the shortest time data were collected for. The shortest time, t, in each experiment is then defined at t = 0 s for all data fittings. Data collected using this experimental scheme are then plotted as normalized intensity versus time (t) and fit to mono-exponential functions to obtain longitudinal relaxation times (T_1), see Fig. 5.2B.

5.2.3 Detection and storage cell preparation

The detection cell used for all measurements was constructed of Pyrex and built to fully fill the detection coil. Storage cells are composed of different materials (glass, brass alloy 260, aluminum 6061, and stainless steel 304); each of these is used as received from the supplier, after cleaning the surface to ensure no contamination was present. Cells had similar, but not identical, inner diameters, 21.2 mm (stainless steel and aluminum), 22.1 mm (brass), and 21.5 mm (glass). All cells have glass tops and bottoms

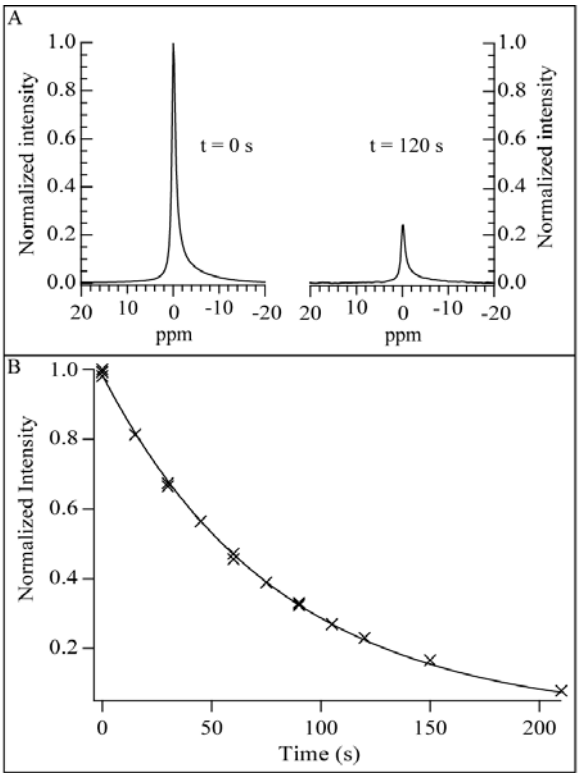

Fig. 5.2: Spectra and relaxation curve for hp ^{83}Kr on a material surface (stainless steel shown at 3 T). Similar spectra and curves are observed for both nuclei with all materials. A) Typical result from the RF pulse sequence is described in the methods and materials section with two resulting spectra per pulse sequence. The first spectrum (denoted as t = 0 s) is the calibration spectrum from the delivery of hp gas to both the storage and detection cell. This pulse gives the relative efficiency of the optical pumping during the course of the experimental series. The second spectrum (denoted as t = 120 s) is the relaxation decayed spectrum of the hp gas delivered from the storage cell to the detection cell. B) Relaxation curve of the corrected and normalized intensities from a series of experiments for a surface at one field strength. The functional form of the curve is based on a monoexponential function. Due to the time required for the collection of a complete T_1, the replication of time points instead of the entire experiment were used to ensure reproducibility and provide a gauge of experimental error.

attached to provide connections to the rest of the delivery system. The use of glass avoids the deposition of magnetic particles onto the surface. Additionally, the volume of the gas mixture in the glass connections is small compared to the storage cell containing the surface of interest, so it has a minimal contribution to the signal. Each cell is evacuated and flushed with dry N_2 gas at least three times and left under vacuum conditions for one hour prior to any experiments. For experiments where oxygen is mixed with hp noble gases to study relaxation behavior, the glass storage cell is used and evacuated (<10 Pa). Then, 25 – 26 kPa of O_2 is introduced into the cell and the cell is sealed from the system by "Valve C" in Fig 5.1A until delivery of hp gas.

5.3 Results and discussion

5.3.1. Requirements for field dependent longitudinal relaxation

For T_1 to be dependent on the magnetic field strength, the correlation time (τ_c) must be on the inverse order of the larmor frequency (ω_0) for the nucleus of interest (i.e. 10 ns for 100 MHz). This arises from the spectral density function $J(\omega)$:

$$J(\omega) = \frac{\tau_c}{1 + \omega_0^2 \tau_c^2} \qquad \text{[Eq. 5.1]}$$

where τ_c is the correlation time, and ω_0 is the larmor frequency. Each relaxation mechanism depends on the normalized spectral density, and the interaction responsible for the magnetic field fluctuations defines the exact functional dependence of the longitudinal relaxation on $J(\omega)$. A general mathematical expression describes the relationship between T_1 and $J(\omega)$ [25]:

$$1/T_1 = \gamma^2 \left[B_{xL}^0 \right]^2 J(\omega_0) = \gamma^2 \left[B_{xL}^0 \right]^2 \frac{2\tau_c}{1+\omega_0^2\tau_c^2} \qquad \text{[Eq. 5.2]}$$

where γ is the gyromagnetic ratio and $\left[B_{xL}^0 \right]^2$ is the root mean squared fluctuations in the x-component of the magnetic field. The extreme narrowing condition, which occurs when $\tau_c << 1/\omega_0$, is applied to Eq. 5.2:

$$1/T_1 = 2\gamma^2 \left[B_{xL}^0 \right]^2 \tau_c \qquad \text{[Eq. 5.3]}$$

From Eq. 5.3, T_1 is field independent in this regime as ω_0 is the only field dependent variable. Applying the extreme narrowing condition to Eq. 5.1 removes all field dependence in the normalized spectral density equation. Thus, under the extreme narrowing condition, field independent relaxation can be expected. It should be noted that depending on the functional form of $\left[B_{xL}^0 \right]$, for a given relaxation mechanism, a field dependence could still be observed.

It is only in the aforementioned regime, $\tau_c \approx 1/\omega_0$, that field dependent T_1 times are expected. However, the long correlation times needed to observe field dependent relaxation, $\tau_c \approx 10$ ns, are not expected in the gas phase where binary collisions are on the order of a few picoseconds and short-lived van der Waals molecules have life times around 10^{-10} s (Xe-Xe at 1 amagat xenon density, where 1 amagat is the density of the gas under standard conditions [14]). Average adsorption times on surfaces are expected to be on the order of 10^{-10} s, based on work with xenon on borosilicate glasses at room temperature [26]. Whereas the correlation times from these events are not long enough to produce field dependent T_1 times, strong adsorption sites on the surfaces could lead to

correlations times long enough for field dependent relaxation. In this work, the temperature is held constant for all experiments. Note that the correlation time can be influenced by temperature and therefore temperature changes could satisfy the condition of $\tau_c \approx 1/\omega_0$, to make T_1 field dependent.

5.3.2. Behavior of longitudinal relaxation on surfaces at differing field strengths

There have been extensive studies [12; 27; 28; 29; 30] to find the ideal conditions to store the hp noble gas isotopes ^{3}He and ^{129}Xe, i.e. the factors for the slowest relaxing system. For these two nuclei, the main source of relaxation is paramagnetic centers on the surface of the storage container that can relax the hp gas even during brief periods of adsorption. Variables considered for storage of hp noble gases include the material for storing the gas [12; 27; 28] and the cryogenic temperature used for storage [29; 30]. Care is also taken with these nuclei to ensure that paramagnetic oxygen does not contaminate the storage cell. For hp ^{83}Kr, there is relaxation data pertaining to various surface modifications of glass [2] as well as relaxation behavior at low temperatures [31].

Fig. 5.3 and Fig. 5.4 display T_1 times as a function of field strengths for hp ^{83}Kr and hp ^{129}Xe, respectively. Numerical values for each data point are presented in Table 5.1. Previous reports of hp ^{83}Kr relaxation [2; 8] have shown that the longest relaxation times are for untreated glass, which is also observed here, see Fig. 5.3. In addition to glass having the longest relaxation for ^{83}Kr, it also displays a strong field dependent relaxation as the field increases from 0.5 to 3 T. While there appears to be a less

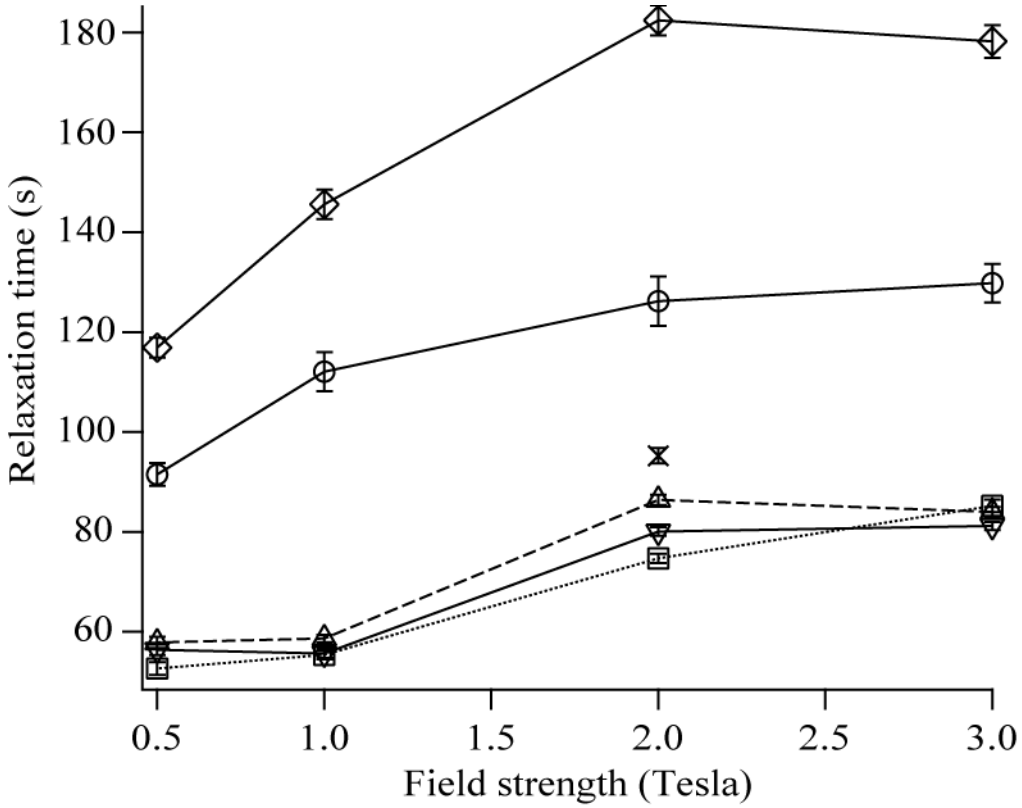

Fig. 5.3: Longitudinal relaxation times of hp ^{83}Kr in different materials plotted against field strength, with each material shown as a different symbol. 20% hp ^{83}Kr is shown stored in glass (open diamond and solid line), glass with 20% molecular oxygen (open circle and solid line), aluminum (open triangle, pointing up, and dashed line), stainless steel (open triangle, pointing down, and solid line), and brass (open square, and dotted line). 5% hp ^{83}Kr is shown only for stainless steel at 2T field strength (diagonal cross). Error bars represent the error from fitting the data and include replicate data points at certain time points. The pressure in the storage cell for all measurements was 125 kPa ± 1 kPa, including the 20% oxygen added for certain experiments.

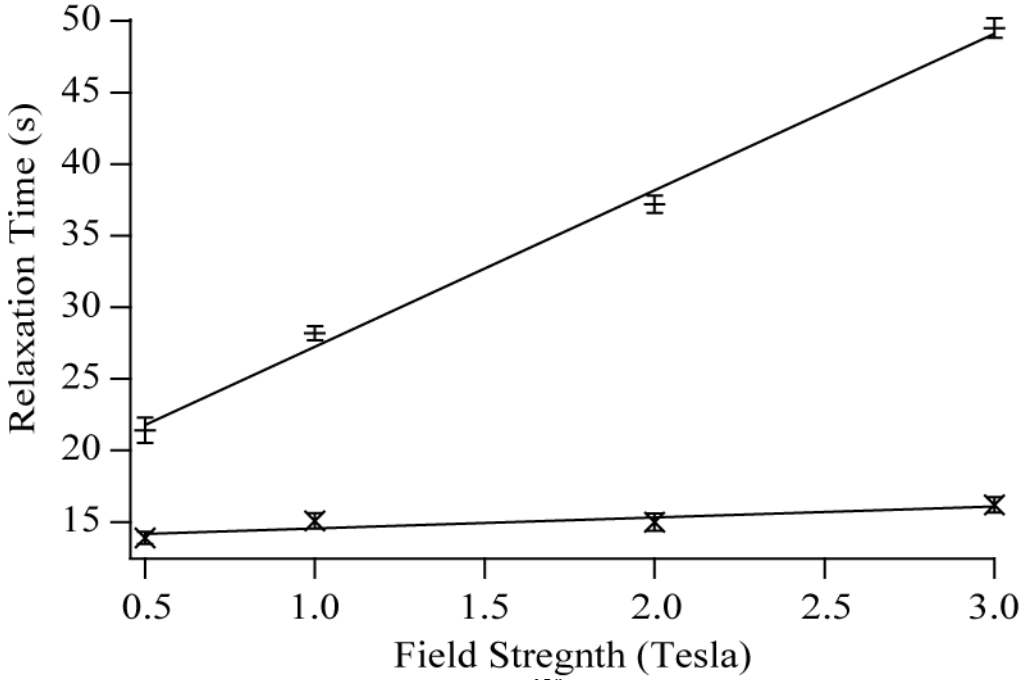

Fig. 5.4: Longitudinal relaxation times of hp ^{129}Xe in different materials plotted against field strength, with each material shown as a different symbol. 5% hp ^{129}Xe is shown stored in glass with 20% molecular oxygen (diagonal cross) and stainless steel (horizontal line marker). Error bars show the error from fitting the data and include replicate data points at certain time points. The storage pressure for all measurements was 125 kPa ± 1 kPa, including the 20% oxygen added for certain experiments.

Field strength (Tesla)	Relaxation times (s) on material surfaces: 5% hp ^{129}Xe		20% hp ^{83}Kr					5% hp ^{83}Kr
	Stainless steel	Glass with 20% oxygen	Glass	Glass with 20% oxygen	Stainless steel	Brass	Aluminum	Stainless steel
3.0	49.5 ± 0.7	16.2 ± 0.5	178 ± 3	130 ± 4	81.2 ± 0.8	85 ± 1	84 ± 1	
2.0	37.2 ± 0.6	15.0 ± 0.6	182 ± 3	126 ± 5	80.1 ± 0.9	74.7 ± 0.9	86 ± 1	95 ± 2
1.0	28.2 ± 0.5	15.1 ± 0.5	146 ± 3	112 ± 4	55.7 ± 0.9	55.4 ± 0.9	58.7 ± 0.7	
0.5	21.4 ± 0.9	13.9 ± 0.4	117 ± 3	92 ± 2	56 ± 1	53 ± 1	58 ± 1	

Table 5.1: T_1 relaxation times on material surfaces at different magnetic field strengths.

T_1 values were measured by remotely detected relaxometry for hp ^{129}Xe and ^{83}Kr on various material surfaces at differing field strengths. The uncertainties are the error from the fitting of the data including replicated time points providing error in reproduced measurements. The storage pressure of all measurements was 125 kPa ± 1 kPa, including the 20% oxygen added for certain experiments.

pronounced changing in the relaxation curve for glass as it approaches 3 T, a previous report for hp ^{83}Kr [8] reported longer relaxation times in a glass sample cell at a higher field strength of 9.4 T. From [8], T_1 of hp ^{83}Kr relaxation observed in a glass cell was found to be ~120 s at 3 T field strength compared to 178 s at 3 T reported here. ^{83}Kr relaxation has been shown to be very sensitive to surface-to-volume ratios, and the glass cell used by [8] had an I.D. of 12.5 mm compared to the I.D. of 21.5 mm used in this work. The difference in cell I.D. can account for the different T_1 times observed when comparing [8] and this work. Additionally, the less pronounced change in T_1 times could be due to the changes in ω_0 as the field increases, thereby changing from a field dependent regime to a field independent regime. This would be the expected trend as the field dependence of T_1 would be most sensitive where $\tau_c \approx 1/\omega_0$, and as ω_0 increases with increasing field, this condition is no longer valid.

Fig. 5.3 shows the relaxation of hp ^{83}Kr on non-magnetic metals: brass, aluminum, and stainless steel. For each of these three metals, the T_1 for ^{83}Kr is shorter than that of glass for all field strengths examined in this work. The relaxation behavior for ^{83}Kr in these metallic cells does not follow the same pattern observed in glass cells. The relaxation behavior is not a well-described function (i.e. linear, exponential), instead it appears to be a step function. To fully understand ^{83}Kr relaxation on these surfaces, more field strengths need to be explored to determine if the flat behavior observed from 0.5 to 1 T and from 2 to 3 T is continued at lower and higher fields, respectively. One similarity between all the measurements, for glass and metals, is that the reduction in T_1 time from 3 to 0.5 T is very similar. The reduction in T_1 for glass is 34%, similar to the 31% reduction observed in aluminum and stainless. Brass has the largest reduction for T_1

of ^{83}Kr of 38%. Relaxation behavior of ^{83}Kr on these metal surfaces indicates that the relaxation induced by paramagnetic centers (present on stainless steel) does not accelerate the T_1 times beyond that of the quadrupolar interactions on a non-magnetic surface (such as aluminum). This indicates that the while the presence of a metal is destructive to the polarization of hp ^{83}Kr, the composition of the metal is not of particular concern to the ^{83}Kr nucleus.

For comparison, hp ^{129}Xe gas is studied in the stainless steel cell where the T_1 times are found to be very dependent on field strength, ranging from 49.5 ± 0.7 s for 3 T down to 21.4 ± 0.9 s for 0.5 T. This represents a reduction in T_1 times of 57 %, the largest reduction observed in this work. Interestingly, with the increased relaxation time of hp ^{129}Xe on stainless steel, it is plausible that for systems such as a canula (used for attachment to the trachea of small animals to carry out lung studies), minimal relaxation should be expected from the stainless steel construction in the high field region of a superconducting magnet. However, these data also indicate that at low field systems [32; 33], or even near earth-field systems [34], the presence of stainless steel between the SEOP cell and the detection region could depolarize the hp ^{129}Xe. Remarkably, the T_1 times for hp ^{129}Xe are always shorter on stainless steel than those for hp ^{83}Kr on stainless steel, due to its larger gyromagnetic ratio.[6] Therefore, the relaxation mechanism of ^{129}Xe is primarily through interactions with local paramagnetic regimes on the surface of the metal, even if the overall metal sample is considered non-magnetic.

Although each of these metals can be considered as a homogenous system, the surface of these metals will contain oxides and could have exposed paramagnetic sites. These paramagnetic species could be the primary source of relaxation for hp noble gases

and cannot be removed without special treatment of the surface (i.e. machining or coating), which could induce larger variations. It should be noted that while care is taken to minimize the volume of hp gas contained in transfer lines and connections between the delivery system and the storage cells, this volume cannot be eliminated. Therefore, the T_1 values obtained from this experimental setup should be considered as the upper limit due to signal that might survive in the connections.

5.3.3. Longitudinal relaxation in the presence of oxygen at various field strengths

Hp ^{129}Xe and hp ^{83}Kr were each mixed with a breathable mixture of oxygen (approximately 20%, the necessary amount for *in vivo* studies). T_1 times are obtained to provide insight into the relaxation behavior of hp gases and how they change as a function of field strength. Previous studies [17; 35; 36] have shown that the long T_1 of ^{129}Xe in the gas phase (typically on the order of hours) is reduced to between 10 – 20 s in the presence of oxygen. Jameson *et al.* [18] previously studied the effect of oxygen on the relaxation of ^{129}Xe; the xenon partial pressure used for the studies in [18] was 5 amagat with 9 - 33 amagat of oxygen partial pressure. These mixtures contain greater than the 20% oxygen required for *in* vivo studies and the pressures far exceed ambient. ^{83}Kr T_1 time studies have shown reductions of approximately 18% in the presence of oxygen in canine lung tissue [1], from 10.5 to 8.6 s. It should be noted that an initial study of hp ^{83}Kr T_1 times conducted in *ex vivo* rat lungs (Chapter 6) has shown no reduction of T_1 times in the presence of oxygen.

A field dependence in T_1 is observed for hp ^{83}Kr gas in the presence of a breathable mixture of oxygen (Fig. 5.3, open circles). Compared to the T_1 of ^{83}Kr in the

same glass cell at 3 T (178 ± 3 s), the T_1 for ^{83}Kr mixed with oxygen is reduced to 130 ± 4 s, a reduction of 27%. This reduction is very similar to that at the lowest field, 0.5 T, where T_1 of ^{83}Kr in the gas phase is 117 ± 2 s, compared to 92 ± 2 s when mixed with oxygen, a reduction of 21%. By comparing the two extremes for both gas mixtures, a reduction in T_1 time for ^{83}Kr in the presence of oxygen from 3 to 0.5 T, corresponding to 29%, is very similar to the reduction of T_1 times observed by ^{83}Kr in the same glass cell without oxygen (34% reduction in T_1 times). Considering the relevance of this T_1 behavior to *in vivo* MRI, the T_1 reduction represents a loss in useable signal; however, the reduced T_1 time for ^{83}Kr is still longer than T_1 times for ^{83}Kr obtained on other surfaces (brass, aluminum, stainless steel). This indicates that the ^{83}Kr T_1 times are still sensitive to surfaces, even in the presence of oxygen. Also the T_1 of ^{83}Kr still exceeds one minute when mixed with oxygen; this suggests that hp ^{83}Kr can be premixed with oxygen in a storage container before being administered to a subject, provided that inhalation follows soon after (within 10-15 s). A similar slowing of changes in the T_1 of ^{83}Kr, as observed on glass, is also observed in the presence of oxygen on glass. Although the presence of oxygen has reduced the T_1 of ^{83}Kr, relaxation on the surface is still the dominant mechanism. Therefore it is expected that a slowing of change in T_1 would be present as observed on glass. The correlation time for ^{83}Kr with the oxygen could also be influencing the change in T_1 time; however, further experiments would be needed to separate the correlation time for the surface from the correlation time with the oxygen.

While the ^{83}Kr T_1 has a field dependence in the presence of oxygen, ^{129}Xe T_1 does not under similar conditions. Fig. 5.4 and Table 5.1 show the T_1 times collected for hp ^{129}Xe in the presence of 20% oxygen for magnetic field strength ranging from 0.5 – 3 T.

The T_1 times for ^{129}Xe are reduced from hours in the absence of oxygen [17; 35; 36] to 13 – 16 s when mixed with oxygen, and the magnetic field shows little influence on the T_1 times. It is likely that in the presence of oxygen in the gas phase, extremely short correlation times maintain the $\tau_c << 1/\omega_0$ condition, therefore T_1 is field independent in the presence of oxygen. It can also be concluded that, due to the shortening of T_1 for hp ^{129}Xe in the presence of oxygen, it is unlikely that surface sensitive relaxation would be observed. However, it should be noted that chemical shift data would still be accessible for *in vivo* MRI using ^{129}Xe mixed with oxygen. For this reason, hp ^{83}Kr can provide very complimentary data to hp ^{129}Xe as ^{83}Kr retains its surface sensitive characteristics even in the presence of oxygen. While these data would suggest premixing hp ^{129}Xe and oxygen would relax most of the polarization, this is typically bypassed for hp ^{129}Xe *in vivo* studies where mixing with oxygen is done as close to the subject as possible [37]. This prevents depolarization of the hp ^{129}Xe gas prior to inhalation, thereby providing the largest signal enhancement possible. For hp ^{83}Kr, the ability to mix the hp gas with oxygen allows for large quantities of gas to be inhaled for *in vivo* studies. This may be necessary due to the lower polarization of hp ^{83}Kr produced compared to that of hp ^{129}Xe. Additionally krypton gas does not have the anesthetic properties of xenon gas [38]; therefore high concentrations of krypton could be higher than the concentrations useable by xenon without causing anesthetic effects [38; 39].

5.4 Conclusion

A survey of ^{83}Kr and ^{129}Xe relaxation in the presence of metal surfaces and oxygen is presented in this work. The longest relaxation times for both nuclei are in systems with minimal concentration of paramagnetic species (i.e. glass), although it is possible to measure relaxation times for paramagnetic systems (i.e. oxygen and stainless steel). For ^{83}Kr, relaxation times of as long as 180 s were found for an untreated glass container at 3 T, while for metal surfaces relaxation times of approximately 80 s were found. In untreated glass, ^{83}Kr relaxation is found to be field dependent with relaxation times as short as 120 s at 0.5 T. Relaxation on metal surfaces is not well defined as a function of magnetic field strength and requires further investigation at this time. When compared to ^{129}Xe, ^{83}Kr relaxation is found to be longer on the stainless steel surface in all magnetic field strengths explored thus far. This is partially due to the smaller gyromagnetic ratio of ^{83}Kr compared to that of ^{129}Xe as well as the quadrupolar interactions, which is the dominant relaxation pathway over that of paramagnetic interactions. For all surfaces studied, ^{83}Kr T_1 times ranged from 50 s (on brass, 0.5 T) to 180 s (on glass, 3T) while ^{129}Xe T_1 times ranged from 21 s to 49 s on stainless steel at 0.5 to 3 T, respectively. The relaxation data presented in this work will help to modify SEOP conditions by prolonging relaxation in cells by use of higher field strengths and may have implications for longer term storage of hp ^{83}Kr.

In addition to metal surfaces, the behavior of relaxation for ^{129}Xe and ^{83}Kr in the presence of oxygen is also reported. A reduction in the relaxation times for both nuclei is observed, although the behavior at various field strengths is quite different. For ^{129}Xe, T_1 is found to range from 13.9 to 16.2 s at magnetic field strengths of 0.5 to 3 T in the

presence of oxygen. These, mostly field independent, T_1 times are significantly reduced from a T_1 of hours for ^{129}Xe in the gas phase [17; 35; 36]. For ^{83}Kr the general behavior of relaxation time in the presence of oxygen is similar to the behavior of ^{83}Kr on glass without oxygen; however, T_1 is reduced by approximately 30 %. ^{83}Kr T_1 times with oxygen present range from 92 to 130 s at magnetic field strengths of 0.5 to 3 T, compared to 117 to 178 s without oxygen on the same glass surface and field strengths. Measurements for ^{83}Kr indicate that while a reduction in T_1 will occur in the presence of oxygen and at lower fields, hp ^{83}Kr and oxygen mixtures potentially have a long enough T_1 to be inhaled by small animals [7], and eventually humans, for *in vivo* studies. Even though the T_1 of ^{83}Kr is reduced, the reduction is not as severe as for ^{129}Xe, and therefore should still provide surface sensitive relaxation, even in *in vivo* systems such as lungs. This surface sensitive relaxation of hp ^{83}Kr could be utilized as a relaxation based contrast agent for *in vivo* imaging.

5.5. Acknowledgements

This work was funded by the National Science Foundation under Grant No.: CHE-0135082 and CHE-0719423. The authors wish to thank Michael Olsen, Tom Frederick, and James Shorkey for construction of the specialized glassware and equipment used in these experiments, as well as Dr. Michael Barlow and Dr. Zackary Cleveland for discussions regarding relaxation of ^{129}Xe.

References:

[1] G.E. Pavlovskaya, Z.I. Cleveland, K.F. Stupic, and T. Meersmann, Hyperpolarized Krypton-83 as a New Contrast Agent for Magnetic Resonance Imaging. Proceedings of the National Academy of Sciences of the United States of America 102 (2005) 18275-18279.

[2] K.F. Stupic, Z.I. Cleveland, G.E. Pavlovskaya, and T. Meersmann, Quadrupolar Relaxation of Hyperpolarized Krypton-83 as a Probe for Surfaces. Solid State Nuclear Magnetic Resonance 29 (2006) 79-84.

[3] Z.I. Cleveland, K.F. Stupic, G.E. Pavlovskaya, J.E. Repine, J.B. Wooten, and T. Meersmann, Hyperpolarized Kr-83 and Xe-129 NMR relaxation measurements of hydrated surfaces: Implications for materials science and pulmonary diagnostics. Journal of the American Chemical Society 129 (2007) 1784-1792.

[4] Z.I. Cleveland, and T. Meersmann, Studying porous materials with krypton-83 NMR spectroscopy. Magnetic Resonance in Chemistry 45 (2007) S12-S23

[5] Z.I. Cleveland, and T. Meersmann, Density-independent contributions to longitudinal relaxation in Kr-83. Chemphyschem 9 (2008) 1375-1379.

[6] Z.I. Cleveland, G.E. Pavlovskaya, K.F. Stupic, J.B. Wooten, J.E. Repine, and T. Meersmann, Detection of Tobacco Smoke Deposition by Hyperpolarized Krypton-83 MRI. Magnetic Resonance Imaging 26 (2008).

[7] Z.I. Cleveland, G.E. Pavlovskaya, N.D. Elkins, K.F. Stupic, J.E. Repine, and T. Meersmann, Hyperpolarized Kr-83 MRI of lungs. Journal of Magnetic Resonance 195 (2008) 232-237.

[8] Z.I. Cleveland, G.E. Pavlovskaya, K.F. Stupic, C.F. LeNoir, and T. Meersmann, Exploring hyperpolarized 83Kr by remotely detected NMR relaxometry. Journal of Chemical Physics 124 (2006) 044312.

[9] T.G. Walker, and W. Happer, Spin-exchange optical pumping of noble-gas nuclei. Review of Modern Physics 69 (1997) 629-642.

[10] Z.I. Cleveland, and T. Meersmann, Binary-collision-induced longitudinal relaxation in gas-phase Kr-83. Journal of Chemical Physics 129 (2008) 6.

[11] A. Deninger, W. Heil, E.W. Otten, M. Wolf, R.K. Kremer, and A. Simon, Paramagnetic relaxation of spin polarized He-3 at coated glass walls Part II. European Physical Journal D 38 (2006) 439-443.

[12] M.F. Hsu, G.D. Cates, I. Kominis, I.A. Aksay, and D.M. Dabbs, Sol-gel coated glass cells for spin-exchange polarized He-3. Applied Physics Letters 77 (2000) 2069-2071.

[13] B.C. Anger, G. Schrank, A. Schoeck, K.A. Butler, M.S. Solum, R.J. Pugmire, and B. Saam, Gas-phase spin relaxation of Xe-129. Physical Review A 78 (2008).

[14] B.N. Berry-Pusey, B.C. Anger, G. Laicher, and B. Saam, Nuclear spin relaxation of Xe-129 due to persistent xenon dimers. Physical Review A 74 (2006) 063408.

[15] B. Driehuys, G.D. Cates, E. Miron, K. Sauer, D.K. Walter, and W. Happer, High-volume production of laser-polarized Xe-129. Applied Physics Letters 69 (1996) 1668-1670.

[16] B.M. Goodson, Using injectable carriers of laser-polarized noble gases for enhancing NMR and MRI. Concepts in Magnetic Resonance 11 (1999) 203-223.

[17] B.M. Goodson, Nuclear magnetic resonance of laser-polarized noble gases in molecules, materials, and organisms. Journal of Magnetic Resonance 155 (2002) 157-216.

[18] C.J. Jameson, A.K. Jameson, and J.K. Hwang, Nuclear-Spin Relaxation by Intermolecular Magnetic Dipole Coupling in the Gas-Phase Xe-129 in Oxygen. Journal of Chemical Physics 89 (1988) 4074-4081.

[19] B. Saam, W. Happer, and H. Middleton, Nuclear-Relaxation of He-3 in the Presence of O-2. Physical Review A 52 (1995) 862-865.

[20] M.C. Fischer, S. Kadlecek, J.S. Yu, M. Ishii, K. Emami, V. Vahdat, D.A. Lipson, and R.R. Rizi, Measurements of regional alveolar oxygen pressure using hyperpolarized He-3 MRI. Academic Radiology 12 (2005) 1430-1439.

[21] J. Wolber, A. Cherubini, M.O. Leach, and A. Bifone, Hyperpolarized Xe-129 NMR as a probe for blood oxygenation. Magnetic Resonance in Medicine 43 (2000) 491-496.

[22] J. Wolber, A. Cherubini, M.O. Leach, and A. Bifone, On the oxygenation-dependent Xe-129 T-1 in blood. Nmr in Biomedicine 13 (2000) 234-237.

[23] A.J. Moule, M.M. Spence, S.I. Han, J.A. Seeley, K.L. Pierce, S. Saxena, and A. Pines, Amplification of xenon NMR and MRI by remote detection. Proceedings of the National Academy of Sciences of the United States of America 100 (2003) 9122-9127.

[24] M.G. Mortuza, S. Anala, G.E. Pavlovskaya, T.J. Dieken, and T. Meersmann, Spin-exchange optical pumping of high-density xenon-129. Journal of Chemical Physics 118 (2003) 1581-1584.

[25] R.K. Harris, Nuclear Magnteic Resonance Spectroscopy, Pitman, London, 1983.

[26] R. Butscher, G. Wäckerle, and M. Mehring, Nuclear quadrupole interaction of highly polarized gas phase 131Xe with a glass surface. Journal of Chemical Physics 100 (1994) 6923-6933.

[27] S.R. Breeze, S. Lang, I. Moudrakovski, C.I. Ratcliffe, J.A. Ripmeester, G. Santyr, B. Simard, and I. Zuger, Coatings for optical pumping cells and short-term storage of hyperpolarized xenon. Journal of Applied Physics 87 (2000) 8013-8017.

[28] R.E. Jacob, B. Driehuys, and B. Saam, Fundamental mechanisms of He-3 relaxation on glass. Chemical Physics Letters 370 (2003) 261-267.

[29] G. Cho, L.B. Moran, and J.P. Yesinowski, Xe-129 and Xe-131 Nmr of Xenon on Silica Surfaces at 77 K. Applied Magnetic Resonance 8 (1995) 549-572.

[30] S. Lang, I.L. Moudrakovski, C.I. Ratcliffe, J.A. Ripmeester, and G. Santyr, Increasing the spin-lattice relaxation time of hyperpolarized xenon ice at 4.2 K. Applied Physics Letters 80 (2002) 886-887.

[31] D.F. Cowgill, and R.E. Norberg, Spin-Lattice Relaxation and Chemical-Shift of Kr-83 in Solid and Liquid Krypton. Physical Review B 8 (1973) 4966-4974.

[32] R.W. Mair, M.I. Hrovat, S. Patz, M.S. Rosen, I.C. Ruset, G.P. Topulos, L.L. Tsai, J.P. Butler, F.W. Hersman, and R.L. Walsworth, He-3 lung imaging in an open access, very-low-field human magnetic resonance imaging system. Magnetic Resonance in Medicine 53 (2005) 745-749.

[33] C.H. Tseng, G.P. Wong, V.R. Pomeroy, R.W. Mair, D.P. Hinton, D. Hoffmann, R.E. Stoner, F.W. Hersman, D.G. Cory, and R.L. Walsworth, Low-field MRI of laser polarized noble gas. Physical Review Letters 81 (1998) 3785-3788.

[34] S. Appelt, F.W. Hasing, H. Kuhn, J. Perlo, and B. Blumich, Mobile high resolution xenon nuclear magnetic resonance spectroscopy in the earth's magnetic field. Physical Review Letters 94 (2005) 197602.

[35] M.S. Albert, G.D. Cates, B. Driehuys, W. Happer, B. Saam, C.S. Springer, and A. Wishnia, Biological Magnetic-Resonance-Imaging Using Laser Polarized Xe-129. Nature 370 (1994) 199-201.

[36] H.E. Moller, X.J. Chen, B. Saam, K.D. Hagspiel, G.A. Johnson, T.A. Altes, E.E. de Lange, and H.U. Kauczor, MRI of the lungs using hyperpolarized noble gases. Magnetic Resonance in Medicine 47 (2002) 1029-1051.

[37] B. Driehuys, J. Pollaro, and G.P. Cofer, In vivo MRI using real-time production of hyperpolarized Xe-129. Magnetic Resonance in Medicine 60 (2008) 14-20.

[38] S.C. Cullen, and E.G. Gross, The Anesthetic Properties of Xenon in Animals and Human Beings, with Additional Observations on Krypton. Science 113 (1951) 580-582.

[39] M.P. Ramirez, K.C.E. Sigaloff, L.V. Kubatina, M.A. Donahue, A.K. Venkatesh, and M.S. Albert, Physiological response of rats to delivery of helium and xenon: implications for hyperpolarized noble gas imaging. Nmr in Biomedicine 13 (2000) 253-264.

CHAPTER 6

Longitudinal Relaxation and Magnetic Resonance Imaging of Lungs with Hyperpolarized ^{83}Kr

The results presented in this chapter are being prepared for submission as a journal article with authorship as follows: Karl F. Stupic, Nancy D. Elkins, Galina E. Pavlovskaya, John E. Repine, and Thomas Meersmann. Karl F. Stupic and Thomas Meersmann wrote the submission with edits provided by John E. Repine, Nancy D. Elkins, and Galina E. Pavlovskaya. Nancy D. Elkins performed the lung extractions and prepared the lungs for experiments. Galina E. Pavlovskaya performed the MR imaging and processed the image data. Karl F. Stupic and Thomas Meersmann performed the hp ^{83}Kr gas delivery and lung inflation for imaging experiments and the relaxation measurements. Karl F. Stupic produced the hp ^{83}Kr, built the experimental setup, and processed all data from relaxation measurements.

6.1. Introduction

Since the first reported separation of highly polarized ^{129}Xe gas from the extremely reactive alkali metal spin-exchange agent [1], hyperpolarized (hp) noble gases are seen as a key diagnostic tool to the biomedical community for the lungs. A variety of biomedical applications (see reviews [2; 3; 4; 5]) are enabled due to the orders of magnitude increases in signal intensities achieved by spin-exchange optical pumping (SEOP) [6]. Since the first images with hp ^{129}Xe [7] and hp ^{3}He [8] were recorded 15 years ago, many different techniques have been developed using hp noble gas nuclei. Hp ^{3}He has found use in studies of oxygen partial pressure [9] and alveolar size [10; 11], while hp ^{129}Xe, with high tissue solubility and 300 ppm chemical shift range [3], has provided information about gas exchange in lungs [12; 13; 14]. Hp ^{129}Xe was also explored for molecular imaging using functionalized xenon biosensors [15; 16] and was infused directly into blood for MR imaging applications [17].

Hp ^{3}He and ^{129}Xe are the most well known noble gas nuclei and the only stable noble gas isotopes with spin I = 1/2. However, there are three more NMR active noble gas isotopes, namely ^{21}Ne (I = 3/2, natural abundance 0.27%), ^{83}Kr (spin I = 9/2, natural abundance 11.5%), and ^{131}Xe (spin I = 3/2, natural abundance 21.2%). Each of these nuclei possesses a nuclear electric quadrupolar moment and it is the quadrupolar interactions in these noble gas atoms that dominate spin relaxation and cause coherent spin evolution. These interactions were exploited in NMR measurements in the past [18; 19; 20; 21; 22; 23; 24] including MRI usage of thermally polarized, liquefied ^{131}Xe [25]. Sufficient signal strength was obtained through rapid signal averaging that is possible in micro porous materials with large surfaces areas that causes fast longitudinal relaxation

time (T_1) of quadrupolar noble gases. However, the signal intensity from thermally polarized gas phase atoms is too low for practical NMR spectroscopy and MRI application in materials with pore sizes above a hundred micrometer. Rapid data acquisition required for many *in vivo* studies does not allow for signal averaging at all and *in vivo* MR is therefore not feasible with thermally polarized noble gases. However, recent developments in hyperpolarization of ^{83}Kr allow for a host of new NMR and MRI studies [26; 27; 28]. Hp ^{83}Kr is achieved by SEOP similar to methodology developed for ^{129}Xe and ^{3}He [6], and while the T_1 of solid krypton does not allow for cryogenic accumulation [29], the gas phase T_1 is sufficiently long enough to achieve separation of the alkali metal vapor from the hp gas [26]. The gas phase T_1 of ^{83}Kr was found to be on the order of hundreds of seconds at atmospheric pressure [20; 30; 31]; however, in the presence of a surface, the T_1 of ^{83}Kr was found to be sensitive to surface chemistry[32; 33], surface hydration [34], surface temperature [26], and to the surface-to-volume ratio [32]. This sensitivity in T_1 of ^{83}Kr was shown to provide MRI contrast [27; 33] and could provide complimentary information to that obtained with hp ^{129}Xe, which has 300 ppm chemical shift range but no relaxation sensitivity, or ^{3}He, which has no chemical shift or relaxation sensitivity. With the large ^{83}Kr spin polarization produced through SEOP, rapid imaging sequences such as variable flip angle FLASH [35] can be used to acquire a full image from a single polarization period as shown with hp ^{83}Kr MRI detection of tobacco deposition on glass capillaries [33].

Previous reports with hp ^{83}Kr provide the proof-of-concept of ^{83}Kr relaxation as a surface sensitive contrast agent [27], feasibility of rapid imaging [33], and imaging of a rat lung [28], however a model for relaxation of ^{83}Kr in different regions of the

respiratory track (the trachea, the bronchi and bronchioles, and the alveoli) has yet to be developed. This work provides a first study of region specific hp ^{83}Kr relaxation in intact and freshly excised small animal (rat) lungs, using natural abundance krypton and an improved storage and delivery system for the hp ^{83}Kr gas. Additionally improved polarization from the use of two 35 W line-narrowed diode array lasers leads to better signal intensity for relaxation measurements as well as implementation of variable flip angle FLASH imaging sequence in a rat lung while achieving improved resolution over previous work with lungs [28].

6.2. Methods and materials

6.2.1. MR imaging

Experiments were performed on a Chemagnetics CMX II NMR spectrometer with a 9.4 T wide-bore (89 mm) superconducting magnet equipped with an imaging system (Resonance Research, Billerica, MA). The imaging system consists of triple axis gradient coils (100 G/cm x,y axes and 720 G/cm z axis) and low-noise linear gradient amplifiers. The custom built probe used for imaging was tuned to the 15.4 MHz ^{83}Kr resonance frequency. A variable flip angle FLASH imaging sequence [33; 35], comprised of 16 phase-encoding steps with no slice selection, was employed to fully utilize the non-Boltzmann polarization resulting from the ^{83}Kr hyperpolarization. The sequence [33; 35] increases the flip angles of subsequent RF pulses in accordance to the equation:

$$\theta_n = \tan^{-1}\left(\frac{1}{\sqrt{N-n}}\right) \qquad \text{[Eq. 6.1]}$$

where N is the total number of RF pulses applied, n is the acquisition increment, and θ_n is the flip angle of the n^{th} RF pulse. The last pulse in the sequence where N = n corresponds to a 90º pulse utilizing the remaining polarization. Such a manipulation of RF pulse lengths in the sequence insures that equal amounts of polarization were used to record each phase-encoding step. This technique is very effective under the assumption that T_1 relaxation in the system of interest (here, lung tissue) is negligible during image acquisition time. To increase the signal to noise ratio in the image shown in this work, the raw data from four images were added together (in the time domain) in MATLAB R2009b (maci64, Math-works, Natick, MA) with zero-filling from 32x16 (raw data) to 32x32 and apodized using a cosine function before Fourier transformation in both dimensions.

6.2.2. Longitudinal relaxation measurements

T_1 measurements were taken in a second custom built probe tuned to the 15.4 MHz ^{83}Kr resonance frequency at 9.4 T. The second probe was capable of holding inflation chambers up to a diameter of 40 mm, allowing for lung expansion without contacting the inflation chamber walls. A pulse sequence consisting of 32 small flip angle (12º) RF pulses spaced evenly in time at intervals of 0.2 s was used to collect a spectrum at each time interval. From this spectra set, data were taken for T_1 fittings that occurred 0.4 s after the maximum integrated intensity in the spectra (defined at t = 0 s). This data were the result from a linear fitting of the natural logarithm of the integrated signal as a function of time and corrected for the polarization destruction occurring from the 12º flip angle RF pulse, as shown in Eq. 6.2:

$$f(t) = \left({}^{1}\!/\!_{\tau} \ln\left(\cos(\theta_i)\right) - {}^{1}\!/\!_{T_1} \right) t \qquad \text{[Eq. 6.2]}$$

In Eq. 6.2, τ is the even time spacing of RF pulses, θ_i is the applied flip angle of the RF pulse, T_1 is the longitudinal relaxation time, and t is the experimental time [33; 36]. The natural log of the signal was normalized to its value at t = 0 s. The linear fitting was applied to data obtained between a t = 0 s up to t = 2.6 s. Non-linearity occurring after this time in all data sets did not allow for further fitting with Eq. 6.2 that assumes mono-exponential relaxation (discussed further in results and discussion).

6.2.3. Spin exchange optical pumping of ^{83}Kr

Hyperpolarized (hp) ^{83}Kr was produced with the use of two 35 W line-narrowed diode array lasers (Spectra Physics, Santa Clara, Ca) with a line width of 0.3 nm tuned to the Rb D1 transition at 794.7 nm. Lasers were oriented such that simultaneous illumination from the front and back of the cylindrical glass SEOP cell (Pyrex glass, no surface treatment, ID = 24 mm, length = 125 mm) was achieved. Stopped flow optical pumping was employed as previously described [28] with a pump cell pressure of 135 kPa. Polarization buildup of hp ^{83}Kr occurred in the SEOP cell for 10 – 20 min to produce proper polarization levels. Each SEOP cell was loaded with 1 g of Rb (99.75%; Alfa Aesar, Ward Hill, MA) and the krypton mixture was produced from research grade gases (Airgas, Radnor, PA) composed of 25% krypton (99.995% pure), 5% nitrogen (99.9997% pure), and 70% helium (99.9999% pure). During operation the SEOP cell containing the gas mixture was heated to 438 ± 5 K inside an aluminum and quartz oven to provide even heating across the cell. All SEOP operation took place in the fringe field of the superconducting magnet at approximately 0.05 T. An air-cooled condenser placed

at the outlet of the SEOP cell was used to separate the Rb vapor from the hp gas. The Rb free hp gas is then passed onto the lungs via storage units as described in section 6.2.5.

6.2.4. Animal care and usage

Following the University of Colorado Health Sciences Center approved protocol, 30 healthy, male Sprague-Dawley rats (Charles River Laboratories, Inc., Wilmington, MA) rats (175 – 400 g) at the time of lung excision were anesthetized with ketamine (80 mg/kg) (University of Colorado Hospital pharmacy) and xylazine (16 mg/kg) (MWT Veterinary Supply, Meridian, ID). 100 USP units heparin (American Pharmaceutical Partners, Inc., Schaumburg, IL) were allowed to circulate for 10-15 s before the lungs were placed on a ventilator. The lungs were perfused with 50 mL of Belzer-MPS solution (UW Kidney Preservation Solution, Trans-Med Corporation, Elk. River, MN) and the trachea was clamped at time of inhalation to avoid collapsing the airways while removing the heart and lungs *en bloc* from the chest cavity. The excised lungs were then cannulated with an adapter tube positioned 5 mm above the bifurcation of the lungs. Following excision, the lungs, with the heart still attached, were immediately transferred into a Pyrex ventilation chamber shown in Fig. 6.1(A-C) (for imaging: ID = 24 mm and height = 100 mm, for relaxation: ID = 34 mm and height = 100 mm) and immersed in ~60 mL of Belzer-MPS solution. The lungs were then inflated to 5-6 mL of air and transported to the imaging facility at a temperature of 277 K.

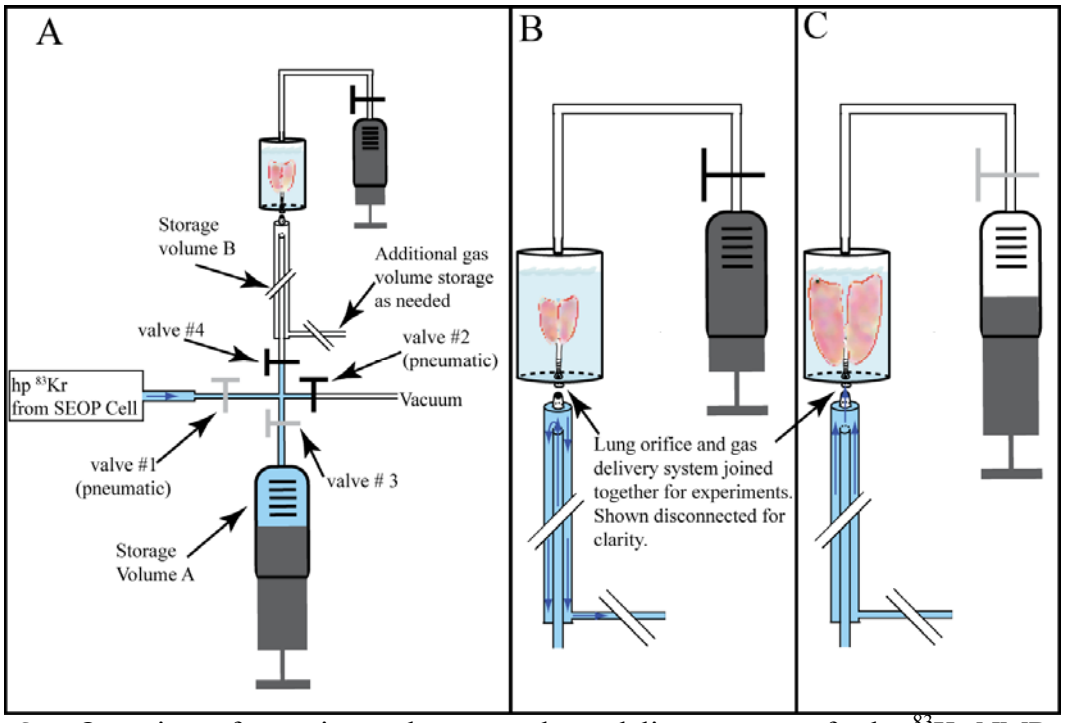

Fig. 6.1: Overview of experimental setup and gas delivery system for hp ^{83}Kr NMR and MRI. A) Experimental setup focusing on delivery of hp ^{83}Kr to the lung for detection. Hp ^{83}Kr flow is marked by arrows and valve status are shaded (dark/black: closed, lighter/gray: open) to indicate experimental procedure. Prior to hp ^{83}Kr delivery, the system up to valve 1 and 4 are closed to allow the system to be cleaned of any absorbed contaminants. Hp ^{83}Kr is first delivered to storage volume A where it is collected. Valve 1 is then closed and valve 4 is opened allowing for krypton to be delivered into storage volume B, where it is stored until the lung is inflated. As shown in the figure, the lungs were inverted (trachea pointing down) and fully immersed in Belzer-MPS solution (UW Kidney Preservation Solution). B) Expanded view of gas delivery to storage volume B. As hp ^{83}Kr pass by the lung orifice where the trachea is connected to the delivery system, the lung remains in a collapsed state. This prevents any lung expansion due to pressure preventing premature entry of hp ^{83}Kr into the lung. Also the volume of storage volume

B is expandable allowing for the volume of hp ^{83}Kr being delivered to the lung to be controlled precisely. Any excess hp ^{83}Kr delivered beyond the capacity of storage volume B is exhausted to open air. C) Delivery of hp ^{83}Kr to the lungs. After pressure has equilibrated in storage volume B, a syringe connected to the top of the *ex vivo* lung ventilation chamber pulls causing the solution level to rise inflating the lungs thereby pulling the hp ^{83}Kr gas into the lung for detection.

6.2.5. Lung ventilation

Prior to any experiments being carried out the lungs were inflated to check that no gas bubbling occurred from the adapter tube to the bottom of the inflation chamber, sutures connecting the trachea to the adapter tube, or from the lung itself. This ensured that any gas delivered to the lungs would not leak out thereby disrupting the data acquisition. After verification that leaking would not occur, all lungs were kept at 290 K which corresponded to the bore temperature of the superconducting magnet.

To avoid substantial relaxation of hp ^{83}Kr and to avoid causing any damage to the lung from risk of over pressurization a system was developed that is shown in Fig. 6.1. Following polarization buildup in the SEOP cell for 10 – 20 min, hp ^{83}Kr was delivered to a pre-evacuated (pressure < 10 Pa) 50 mL borosilicate glass syringe (Chemglass, Vineland, NJ) – i.e. "Storage Volume A" - by pressure equalization as shown in Fig. 6.1A. After delivery of approximately 50 mL of hp ^{83}Kr the valve between syringe and the SEOP cell was closed, while the valve between the syringe and the gas delivery manifold for the ventilation chamber – i.e. "Storage Volume B", - was opened. This allowed for the controlled injection of hp ^{83}Kr from the syringe into "Storage Volume B", until a selected volume of hp ^{83}Kr was delivered (see Fig. 6.1B). During the transfer process the lungs were not allowed to expand, thus preventing the premature entry of hp ^{83}Kr into the lung. The hp ^{83}Kr was transferred from "Storage Volume B" into the lung through inhalation. The inhalation was obtained through suction above the Belzer-MPS solution caused by a second syringe attached to the top of the inflation chamber. The applied suction allowed for inflation of the lung to the desire inflation volume (see Fig. 6.1C).

For measurements with a set of different preselected volumes of hp ^{83}Kr gas mixture, “Storage Volume B” was adapted to suit the necessary volume of gas needed. The outer glass tube of “Storage Volume B” had a determined volume of 6 mL and therefore additional glass pieces would be fitted to expand the volume as needed. However, the experimental setup also allowed for measurements where the lungs inhaled an initial volume of hp ^{83}Kr followed by a further volume of non-hp gas (‘dark’) gas. Vice versa, the lungs could also inhale non-hp gas followed by a selected volume of hp ^{83}Kr. In the case of measurements where molecular oxygen was mixed with hp ^{83}Kr prior to delivery to the lungs, oxygen was delivered to “Storage Volume A” prior to the delivery of hp ^{83}Kr from the SEOP cell.

All longitudinal relaxation (T_1) measurements of hp ^{83}Kr as a function of the lung inflation fall into three different schemes. In scheme 6.1, an excess of hp ^{83}Kr gas mixture was provided for inhalation. A second, modified scheme (scheme 6.2) is the inhalation of non-hp gas prior to inhalation with hp ^{83}Kr. In this work, volumes of 6 mL and 12 mL of un-polarized krypton gas were used to keep the lungs partially inflated before hp ^{83}Kr inhalation. The most advanced scheme (scheme 6.3) used initial inhalation of 6 mL hp ^{83}Kr gas immediately followed by un-polarized gas until the final inflation volume was reached. This is achieved through selection of a total volume of 6 ml for “Storage Volume B” and assumes no mixing of the un-polarized gas with hp ^{83}Kr within this storage volume during the inhalation process.

6.3. Results and Discussion

Polarization levels of hp ^{83}Kr, from the addition of line-narrowed diode array lasers illuminating the SEOP cell from the front and the back, reached an enhancement

factor of 13,000, corresponding to 5.88% polarization. This is an increase of a factor of three from the highest polarization previously reported for hp ^{83}Kr [28]. While certain reductions in polarization are expected due to the relatively slow flow of hp ^{83}Kr from the syringe to the lung orifice (see Fig. 6.1), it is expected to be less than 50% [34]. Therefore, utilizing this high polarization with improvements in technique used to administer hp ^{83}Kr, higher signal-to-noise is obtained for all experiments in this work.

6.3.1. MRI of lungs

An hp ^{83}Kr MR image of an excised rat lung is shown in Fig. 6.2 obtained from variable excitation pulse FLASH experiments (raw data added together, x,y projection, no slice selection) using signal averaging from four experiments (NT = 4) separated by 20 min of SEOP. Image resolution of 0.83 mm x 1.66 mm (raw data) was obtained and shows clear improvement over the previously obtained hp ^{83}Kr rat lung image resolution of 2.33mm x 2.33 mm (raw data) that required 16 individual experiments, each corresponding to a different gradient increment [28]. This represents an improvement of a factor of four in time required for these imaging experiments, caused in part by the increase in polarization through the use of line-narrowed diode-array lasers. Further contributing factors for the signal improvement were the illumination of the front and the back of the pump cell during the polarization time, higher laser power 70 W, and a better hp ^{83}Kr gas delivery system for the inhalation process. The white dashed line encompassing the image in Fig. 6.2 provides the location of the inner wall of the inflation chamber, which constraints the lungs' position. The image provides clear separation

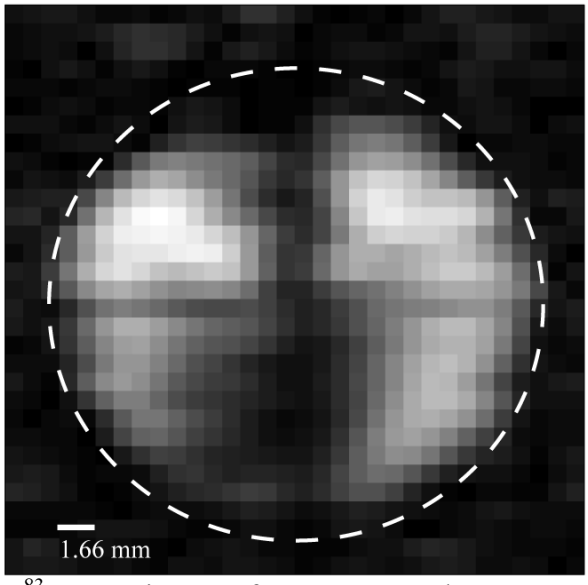

Fig. 6.2: Transverse hp ^{83}Kr MR image of an *ex vivo* rat lung. A variable excitation pulse FLASH sequence comprising 16 phase-encoding steps with no slice selection was employed to fully utilize the ^{83}Kr polarization. The raw data matrix size was 32 x 16 with a FOV of 2.656 cm and a BW of 14 KHz (NEX = 4, no slices selection). The image scale is displayed in the lower left corner and a dashed ring outlines the inner wall of the ventilation chamber. The direction of the applied magnetic field is defined as the z-axis.

between the left and right lungs. A dark area, between the two lungs, occurs in the bottom center region of the image corresponding to the heart, which is devoid of hp ^{83}Kr.

6.3.2. Fitting of longitudinal relaxation data from lungs

T_1 times were obtained for lungs using a pulse sequence which collects 32 spectra equally spaced in time. A typical spectra set for inflations of 20 and 6 mL with full lung inflation using hp ^{83}Kr gas (scheme 6.1) are shown in Figs. 6.3A and 6.4A. As each experiment begins, the inflation of the lung is "captured" as the signal intensity of ^{83}Kr grows with each subsequent spectrum until the signal intensity reaches a maximum. This maximum is assumed to be the point in time where the lung has reached it full inflation volume. However as small fluctuations in lung volume could still occur, data points considered for the T_1 fittings start two spectra after the maxima (corresponding to 0.4 s after the maxima). At this point in experimental time, labeled as t = 0 s, the dependence of the ^{83}Kr signal intensity is assumed to be caused solely by longitudinal relaxation since no significant volume change in the lung is expected. The t = 0 s point is marked in Figs. 3A and 4A by a diamond marker.

Data used in the fittings of T_1 extended, therefore, from t = 0 s for 2.6 s and data collected further than 2.6 s was not considered in the fitting. The 2.6 s cutoff is due to deviations from mono-exponential relaxation behavior. Signal decay that cannot be described by a single time constant (or rate constant) is called multi-exponential behavior and can be caused by multiple effects in the studied system. As lungs and the associated airways are a complex system by which one would expect multiple relaxation rates, a mono-exponential fitting would appear to be a gross simplification of this system. A

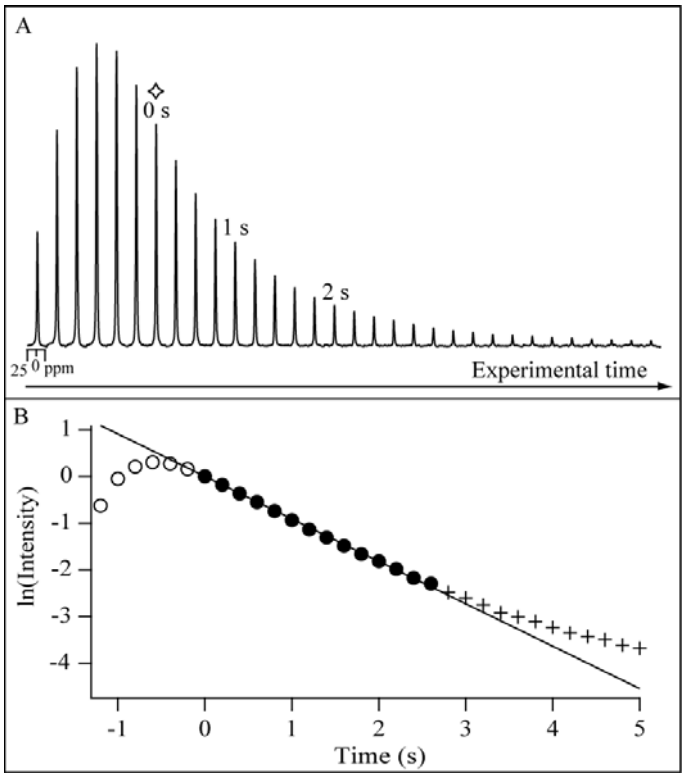

Fig. 6.3: Experimental and fitting data for a 20 mL lung inflation using full inflation volume of 20% hp ^{83}Kr gas available during the inflation of *ex vivo* rat lungs. A) Signal intensity rise and decay resulting from inflation of the *ex vivo* rat lung, where by the signal rises as the lungs inhale hp ^{83}Kr, and after the lungs stop inhaling T_1 relaxation provides for the signal decay. Signal is acquired from a series of 12º RF pulses spaced evenly every 0.2 s. The diamond marker, also marked at t = 0 s, is the time point where only T_1 decay is observed without interference from lung movement influencing the observed signal. B) Plot of the natural logarithm of the integrated intensity from the data shown in A versus time. Three regions are shown, data acquired prior to t = 0 s (open circle), data acquired at or after t = 0 s (closed circle), and data acquired 2.6 s after t = 0 s (crosses). Only data acquired between t = 0 to 2.6 s are fitted to a linear function with a correction factor for the polarization destroyed by the RF pulse to calculate the T_1 value.

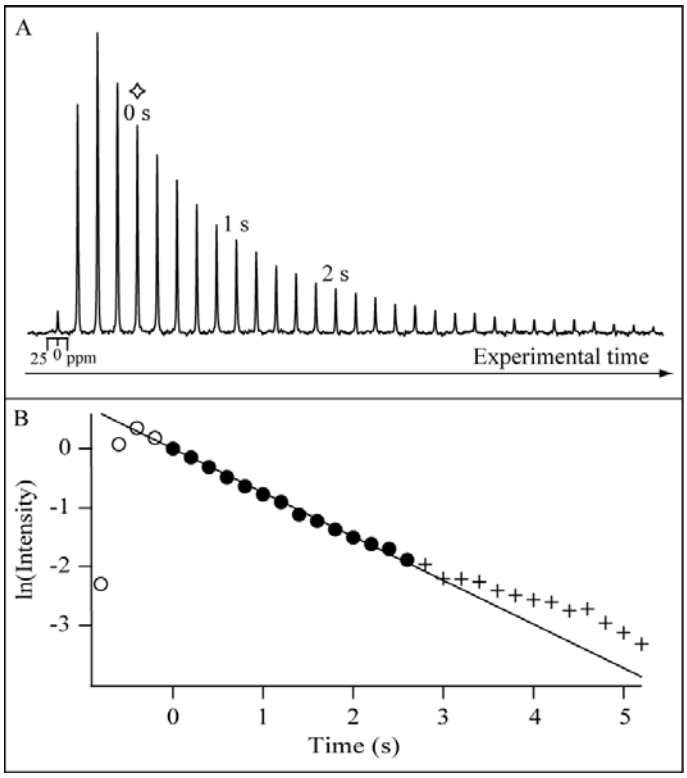

Fig. 6.4: Experimental and fitting data for a 6 mL lung inflation using full inflation volume of 20% hp ^{83}Kr gas available during the inflation of *ex vivo* rat lungs. With the exception of the spectra presented and the data plotted on the graph, all markings are identical to those used in Fig. 6.3.

single rate constant may still be a good description of the hp ^{83}Kr relaxation in lungs as long as the dominant contribution to the signal arises for hp ^{83}Kr contained in the alveolar space of the lung, assuming that the relaxation times from the various alveoli do not deviate excessively from an averaged alveolar T_1 time. However as time progresses, fast longitudinal relaxation in the high surface-to-volume ratio alveoli may reduce the relative contribution of the hp ^{83}Kr signal arising from the alveolar region compared to that from the airways hp ^{83}Kr in the airways will exhibit much slower relaxation with various rate constants depending on the diameter of the airway. Because of slower relaxation, its relative contribution to the signal intensity will therefore rise over time. At t = 2.6 s, a time period of two to three times the T_1 time of ^{83}Kr in the alveolar space, the remaining signal has decayed to about one tenth or less of the original signal from the alveolar space. At this point the decay of the signal arising from various areas of the airways will contribute to the overall appearance of the signal decay. The situation may be further complicated by the possibility that un-relaxed hp ^{83}Kr from "Storage Volume B" or its adapter tube to the lung could diffuse into the airways, thereby causing a perceived slower relaxation. To illustrate this, a semi-logarithmic plot with the natural logarithm of the integrated intensity normalized to t = 0 s versus experimental time is shown in Figs. 6.3B and 6.4B. Figs. 6.3B and 6.4B show the increasing intensity from the inhalation in the lung (shown as open circles) including an additional 0.4 s time period, up to the point where data fitting begins (shown as closed circles).

The linear fitting displayed on both Figs. 6.3B and 6.4B is the fitting to the solid circles and extended both backwards and forwards in time to show the deviations from this fitting as the lung inflates and for times beyond 2.6 s. As mentioned above, data

occurring after the solid circles are not considered in the T_1 fittings and are displayed as crosses. As a requirement for consideration, all spectra sets had to include at least one spectrum prior to reaching the maximum to ensure proper fitting of data, otherwise the spectra set was discarded.

6.3.3. Influence of different inflation schemes

As mentioned in the *Methods and materials* section, three different inflation schemes were developed for use in this work. These schemes were developed as a way to, at lease crudely, discriminate hp ^{83}Kr relaxation behavior in the larger airways from the relaxation in the alveoli and to obtain first approximations of ^{83}Kr T_1 times in these regions. Previously, hp ^{83}Kr T_1 has been shown to have a dependence on surface-to-volume ratio [32] and as such it would be expected that the T_1 times for ^{83}Kr in these different regions could have different T_1 times.

The first scheme does not discriminate between airways and alveoli since all of the void space of the lung is filled with hp ^{83}Kr. As a result, an average value for all regions of the lung is obtained. Note that the behavior may still appear as mono-exponential relaxation because the contribution from the airways is relatively small since an estimated 90% of the lung gas volume is contained within the alveoli. As time progresses, different relaxation in the different regions leads to a stronger relative contribution of the airways to the signal and the multi exponential nature of the hp ^{83}Kr decay becomes apparent. This happens typically after 2.6 s in the studied rat lungs. However, the contribution from the airways can also be emphasized by the second scheme described in the methods section.

In the second scheme, the lung is initially inflated with un-polarized gas for a pre-determined volume, 6 and 12 mL respectively, and then the rest of the volume is filled by hp ^{83}Kr. The idea behind this inflation scheme is to keep hp ^{83}Kr in the airways and out of the alveoli. The alveoli will be inflated with gas that first enters the lung and will therefore contain only thermally polarized gas. The following hp ^{83}Kr would not be able to reach all alveoli and remain to some extent in the airway. This assumption uses a strong simplification of the breathing process, because it ignores that different lobes of the lung expand at different times in the breathing cycle. Note further, that airways consist of very different regions, namely the trachea, the bronchi at different levels of branching and bronchioles. All regions have different surface-to-volume ratios and may additionally provide different ^{83}Kr surface relaxation. Nevertheless, the described scheme should direct hp ^{83}Kr towards the airways and should therefore provide the longest T_1s. Two different volumes of un-polarized gas are used to see whether the relaxation time increases further with increasing 'dark' inhaled gas volume.

The third scheme uses only a small portion of hp ^{83}Kr at the beginning of the lung inflation. In this case, the smallest volume that could be achieved with "Storage Volume B" from Fig. 6.1 was 6 mL. Using the same arguments as for the second scheme, this inflation scheme should direct hp ^{83}Kr towards the alveoli as opposed to the larger airways. Theoretically this would give the shortest T_1 times as the surface-to-volume ratio for the alveoli would be the largest compared to the airways.

Fig. 6.5 shows the results from these three different inflation schemes (two data sets for scheme 6.2 for the two different amount of 'dark' gas volume used), where the data for each fitting is plotted as the natural logarithm of the normalized intensity at t = 0

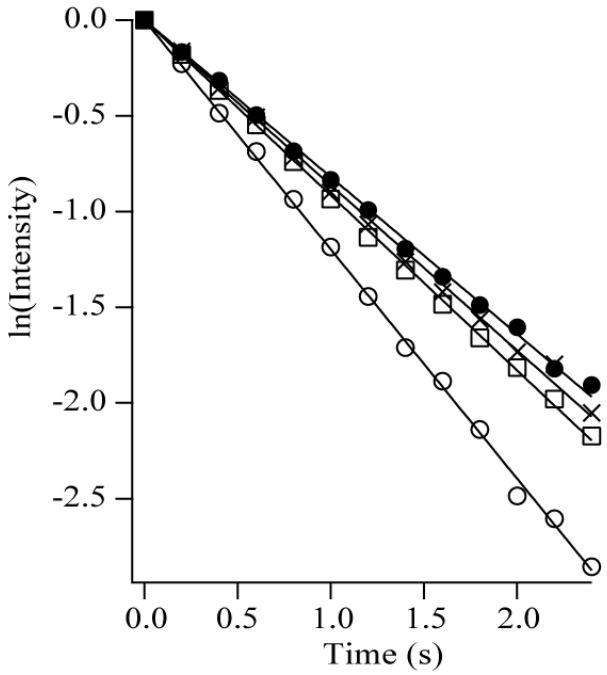

Fig. 6.5: Hp ^{83}Kr signal decay in an *ex vivo* rat lung under different inflation conditions. Presented here are four different inflation conditions for 20 mL lung inflation: only 6 mL of 20% hp ^{83}Kr gas available at the beginning of inflation (open circle), greater than 20 mL of 20% hp ^{83}Kr gas available at the start of inflation (open square), 6 mL un-polarized gas delivered prior to remaining volume being hp ^{83}Kr gas (diagonal crosses), and 12 mL un-polarized gas delivered prior to remaining volume being hp ^{83}Kr gas (closed crosses). The y-axis presented here is the natural log of the signal intensity at t = 0 s, as defined in the methods and materials section. These intensities are measured from a 12º RF pulse applied to the lung during the course of the NMR experiment. Lines are a linear fitting including a compensation term for spin destruction by the applied pulse. T_1 values obtained from this fitting are presented in Fig. 6.5 and Table 6.1.

s versus time. For all four data sets shown in Fig. 6.5, the data is for a final lung inflation volume of 20 mL, thereby keeping the lung inflation the same for each scheme. The inflation with an initial 6 mL of hp ^{83}Kr gas mixture followed by non-hp gas (scheme 6.3) exhibits the steepest slope and thus shortest relaxation time constant T_1 of 1.00 ± 0.08 s (see Fig. 6.5). The upper line in Fig. 6.5 corresponds to 12 mL of un-polarized gas administered before the balance of hp ^{83}Kr gas (scheme 6.2) and represents the slowest T_1 time of 1.48 ± 0.07 s. The remaining lines are the 6 mL of un-polarized gas administered before the balance of hp ^{83}Kr gas (also scheme 6.2) resulting to T_1 of 1.31 ± 0.05 s and full hp ^{83}Kr gas mixture (scheme 6.1) resulting to T_1 of 1.25 ± 0.07 s as the second and third lines from the top respectively. The order of the observed relaxation times for the three inflation schemes follows expected order if regional isolation of the respiratory system was achieved. These inflation schemes can be applied to other inflation volumes to develop a better understanding of ^{83}Kr relaxation in different regions of the respiratory system. Application of the inflation schemes to various lung inflation volumes is discussed in the following section.

6.3.4. Longitudinal relaxation times in lungs

By extending the inflation schemes discussed earlier to inflation volumes ranging from 3 to 20 mL in rat lungs, T_1 times have been acquired and are presented as a function of inflation volume in Fig. 6.6 and numerically in Table 6.1. Each relaxation time is the average of at least two T_1 fittings per inflation volume per rat and of five individual but similar rats (see methods section). The standard deviation shown is obtained from the deviation of individual values from the calculated average value. Similar to the trend

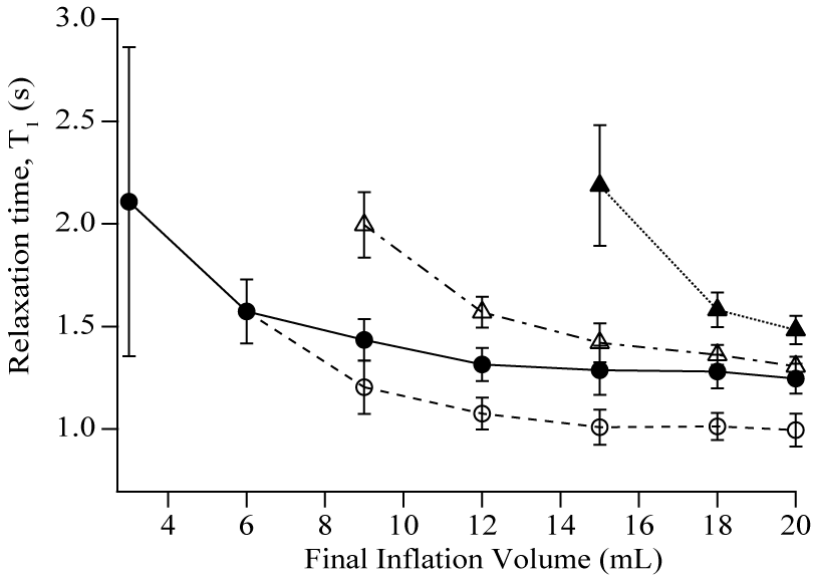

Fig. 6.6: Average longitudinal relaxation times as a function of final inflation volume for different inflation patterns. The four different inflation conditions with various final inflation volumes are shown: only 6 mL of 20% hp ^{83}Kr gas available at the beginning of inflation (open circle and dashed line), a greater volume of 20% hp ^{83}Kr gas available than needed at the start of inflation (closed circle and solid line), 6 mL un-polarized gas delivered prior to remaining volume being hp ^{83}Kr gas (open triangle and dot-dashed line), and 12 mL un-polarized gas delivered prior to remaining volume being hp ^{83}Kr gas (solid triangle and dotted line). Error bars represent one standard deviation for the individual experiments from the averaged value for all rats used in this study. The dashed light for only 6 mL of 20% hp ^{83}Kr gas available was extended to the lower inflation volumes with a greater volume of 20% hp ^{83}Kr gas available as a reference.

Final Inflation	Only hp ^{83}Kr gas T_1 (s)	6 mL hp ^{83}Kr gas at start of inflation T_1 (s)	6 mL of un-polarized gas at start of inflation T_1 (s)	12 mL of un-polarized gas at start of inflation T_1 (s)
3 mL	2.1 ± 0.8			
6 mL	1.6 ± 0.2			
9 mL	1.4 ± 0.1	1.2 ± 0.1	2.0 ± 0.2	
12 mL	1.31 ± 0.08	1.07 ± 0.08	1.57 ± 0.07	
15 mL	1.3 ± 0.1	1.01 ± 0.09	1.42 ± 0.09	2.2 ± 0.3
18 mL	1.28 ± 0.08	1.01 ± 0.07	1.36 ± 0.05	1.58 ± 0.08
20 mL	1.25 ± 0.07	1.00 ± 0.08	1.31 ± 0.05	1.48 ± 0.07

Table 6.1: Table of averaged longitudinal relaxation times for *ex vivo* rat lungs. Averaged T_1 values for all rats used in this study shows different inflation patterns for different final inflation volumes. The error values are representative of one standard deviation for the individual experiments from the averaged value.

observed in Fig. 6.5 for a single inflation volume, scheme 6.2 provides the longest T_1 values, followed by scheme 6.1, and the shortest T_1s are for 6 mL of hp gas administered before un-polarized gas to complete the lung inflation volume (scheme 6.3).

Several trends are observed in Fig. 6.6. One trend is that as the inflation volume increases for all schemes, T_1 times become shorter. In the case of schemes 6.1 and 6.3, the T_1 times are shown to decrease and eventually stabilize at about 12 ml inflation volume to values of T_1 = 1.3 s and T_1 = 1.0 s, respectively. In the case of inflation scheme 6.2, where un-polarized gas is administered prior to hp ^{83}Kr gas, the T_1 times decrease with increasing inflation volume and do not reach a stabilized T_1 time over the measured lung inflation volumes. This indicates that with increasing inhalation volume an increasing fraction of hp ^{83}Kr is contained in the alveolar space where the fastest relaxation is expected due to its high surface-to-volume ratio.

For the inflation scheme 6.2 where 6 mL of un-polarized gas is inhaled first, the T_1 values decrease rapidly with increasing inhalation volume, an effect that is even more pronounced with scheme 6.2 using 12 mL un-polarized gas. This trend can be explained again by the concept of increasing contributions from the alveoli compared to the airways at higher inhalation values. The effect is more pronounced with scheme 6.2 than with scheme 6.1 because a larger proportion of alveolar space is occupied by an un-polarized gas in scheme 6.2 than in scheme 6.1. The relaxation contribution from the airways is therefore more important in scheme 6.2 than in scheme 6.1.

By considering only the measurements that introduced the smallest amount (3 mL) of hp ^{83}Kr into the lungs, namely 3mL full hp ^{83}Kr (scheme 6.1) and 3 mL of hp ^{83}Kr after 6 and 12 mL of un-polarized gas (scheme 6.2), T_1 times of approximately the same

value are obtained (2.1 ± 0.8, 2.0 ± 0.2, and 2.2 ± 0.3 s respectively). Given the current polarization capabilities, 3ml is the smallest volume of hp ^{83}Kr that could be introduced into the lung. Hp ^{83}Kr gas in the airways will strongly contribute to these measurements although relaxation from the alveoli will also be a factor. The results indicate a lower limit of T_1 = 2 – 2.2 s for the averaged relaxation in the airways of rat lungs. The measurement with inflation scheme 6.1 at 3 mL has a large uncertainty but the obtained T_1 is supported by the T_1 times obtained from scheme 6.2. It is possible that the errors come from slight variations in lung structure from rat to rat or from precision in the inflation of the lung. At such small inflations as 3 mL, small deviations in the experiment could induce the greatest changes physiologically in the lungs and airways.

Experiments using scheme 6.3 were designed to isolate the T_1 times of ^{83}Kr in the alveolar space and are performed with final inflation volumes ranging from 9 to 20 mL. At inflation volumes beyond 12 ml, the T_1 times are found to be inflation independent with T_1 values of about 1 s. This is the fastest relaxation observed in the lungs studied. While some mixing could occur in the inhalation process, it is reasonable to consider the hp ^{83}Kr gas to be isolated to the alveolar space and perhaps in the bronchioles and smaller bronchia. The inflation independent relaxation time in the alveoli (and nearby airway regions) is remarkable because one would expect for the alveoli to further expand with increasing inhalation volume. The larger the alveoli, the smaller their surface-to-volume ratio is expected to be. Therefore an increase in the observed T_1 relaxation times with increasing inflation would be expected that is however not observed. There are a number of possible interpretations of the absence of increases in relaxation time with increasing inflation volume. One explanation is that the changing relative volume contribution

between airways and alveoli increases the observed relaxation and counteracts any decrease in relaxation due to the expanding alveoli. A second explanation is that the surface interaction for the krypton changes with increasing expansion and counteracts the decreasing surface-to-volume ratio. Most likely however, is the (third) explanation that the alveoli do not expand beyond an inflated volume that they initially assumed. In other words, when an alveolus expands, it expands rapidly into its inflated state and remains there until deflation. The gradual process of inhalation is then a consequence of individual alveoli expanding at different times rather than individual alveoli expanding gradually. This explanation can be supported by an argument that considers the alveolar surface tension dependence on alveolar expansion. In the collapsed state the tension is large because of the small radius r. However upon alveolar expansion, the surface tension will be reduced with increasing radius r (i.e. barring changes in the surface composition). This in turn would facilitate rapid alveolar expansion to its final inflated state. Vice versa, deflation should follow a similarly rapid process. More conclusive results may be obtained from further improved signal intensities that could be exploited for spatially resolved T_1 and T_2 relaxation measurements focusing on particular regions of the lungs.

Previous work with hp ^{83}Kr has explored the T_1 dependence not only on surface-to-volume ratios [32; 34] but also on surface composition [32], a fact that needs to be explored for lungs, in particular as a probe for lung diseases such as adult respiratory distress syndrome (ARDS) [37] and chronic obstructive pulmonary disease (COPD) [38].

6.3.5. *In vivo* consideration

While the work presented here is done with *ex vivo* rat lungs, it is necessary to consider the demands of studies to be carried out *in vivo* in anesthetized small animal. The foremost consideration for *in vivo* experiments is to use a breathable mixture of hp ^{83}Kr gas and oxygen combined prior to inhalation. Previous work with ^{83}Kr T_1 times has reported a reduction of T_1 by 18% from 10.5 to 8.6 s in desiccated canine tissue with 20% oxygen present [27]. This reduction is smaller than the reduction experienced by ^{3}He and ^{129}Xe, which in the presence of 20% oxygen are reduced from hours (or even days in the case of ^{3}He) to 10-20 s [7; 39; 40; 41].

The low degree of sensitivity of ^{83}Kr relaxation to paramagnetic species (i.e. oxygen) is due to the smaller gyromagnetic ratio of ^{83}Kr compared to those of ^{3}He and ^{129}Xe (4%, 76%, and 28% of ^{1}H, respectively). Although previous data has shown a reduction in T_1 times in the presence of oxygen, the faster T_1 times in rat lungs do are not affected by oxygen. In the presence of 20% oxygen and inflating the lung to 18 mL with this gas mixture (20% oxygen, 80 % hp ^{83}Kr gas mixture), the relaxation time of ^{83}Kr was found to be 1.25 ± 0.01 s from three replicate measurements. Increasing the percentage of oxygen, 40% oxygen and 60% hp ^{83}Kr gas mixture, the T_1 value was found to be 1.22 ± 0.01 s from two replicate measurements. These measurements were conducted identically to the inflation scheme 6.1 but with hp ^{83}Kr gas mixed with 20% oxygen. Comparison of these oxygen measurements to their hp ^{83}Kr analog find the T_1 times obtained are within the error of the full hp ^{83}Kr gas mixture T_1 (T_1 = 1.25 ± 0.07 s). This demonstrates that the presence of oxygen has no appreciable effect on ^{83}Kr T_1 when inside of the lungs. However, a 25% reduction in the hp ^{83}Kr signal for the oxygen

experiments was observed after accounting for the replacement of hp gas by oxygen. This is likely given the premixing of hp ^{83}Kr at low field (<0.1 T, stray field of magnet) with oxygen. Despite the premixing with oxygen, the signal intensity obtained for an 18 mL inflation with oxygen was a factor of three stronger than the best signal intensity obtained for any 3 mL inflation volume with only hp ^{83}Kr gas mixture.

Previous work with ^{83}Kr has shown a T_1 dependence on the surface-to-volume ratio [32] as well as on temperature [26]. While T_1 times of ^{83}Kr in rat lungs ranges from 0.9 to 2.2 s depend on the inflation scheme, it is presumable that T_1 times of ^{83}Kr in a human lung would be longer due to the lower surface-to-volume ratio in the alveoli. The average alveolar diameter of a rat is 94 μm while the average alveolar diameter of a human is 225 μm [42]. Additionally longer T_1 times for ^{83}Kr have been shown with increasing temperature, caused by decreased surface adsorption times on the surface [26]. While not explored in this report, it is presumed that by increasing the temperature of the lungs to the physiological temperature of a rat (310.5 K [43]) an increase in the T_1 time of ^{83}Kr might be observed.

6.4. Conclusions

With the employment of line-narrowed laser sources [44] at moderate power (70 W total) with illumination from the front and the back of the SEOP cell, signal enhancements of 13,000 were obtained for hp ^{83}Kr, corresponding to 5.88% polarization. This is the highest polarization obtained for ^{83}Kr reported to date; however, this polarization will be reduced by relaxation during the delivery to and inhalation by the lungs. Along with improvements in the delivery system, the high polarization of ^{83}Kr

was able to provide reproducible high signal-to-noise in rat lungs from a small flip angle (12°) RF experiment. This signal-to-noise was sufficient to produce the first hp ^{83}Kr FLASH image of a rat lung, allowed for small volumes of hp ^{83}Kr to be administered, and made the extensive data collection possible that provided reproducible T_1 times in multiple lungs.

T_1 times for hp ^{83}Kr in rat lungs were found to range from 1.0 to 2.2 s depending on the degree of lung inflation and on the applied inhalation scheme. This range of T_1 times should allow for *in vivo* hp ^{83}Kr MRI in rats, which breathe at a rate of 1 to 5 times per second. Additionally, initial work has shown that the quadrupolar relaxation of ^{83}Kr is not influenced by the presence of a breathable mixture of hp ^{83}Kr with up to 40% oxygen. Therefore the measured relaxation is from interactions of ^{83}Kr with the surface of the lungs, making this potentially important for *in vivo* diagnostics for lung diseases such as adult respiratory distress syndrome (ARDS) [37] and chronic obstructive pulmonary disease (COPD) [38].

The T_1 relaxation of ^{83}Kr is found to slow down with increasing inflation volume of the excised rat lungs. Using different inflation schemes, the relaxation time increase upon increasing inflation was attributed to a decrease of the relative contribution from hp ^{83}Kr in airways compared to hp ^{83}Kr in the alveoli. An inflation scheme was designed to reduce contributions from the airways. For this scheme, a small initial volume of hp ^{83}Kr was inhaled, followed by an incremented volume of un-polarized gas using a custom designed breathing apparatus. This scheme resulted into inflation independent relaxation times T_1 at higher inflation volumes. An increase of the T_1 time with increasing inhalation volume was never observed although it was expected assuming that alveoli

expand continuously with increasing lung inflation. Future studies will have to apply spatially resolved relaxation measurements to provide a better understanding of the effect and further improvements in the hp ^{83}Kr signal intensity are therefore crucial. Improvements to hp ^{83}Kr signal intensity could come from SEOP cell design [45; 46], higher powered lasers [47], other line-narrowed laser sources [48; 49; 50], and improved delivery methods [51; 52]. Understanding fundamental biological mechanics of the lung [53; 54] may also be possible with higher signal intensity of hp ^{83}Kr. Excluding system improvements mentioned here, an improvement of nearly a factor of eight can be achieved by using isotopically enriched krypton. With the employment of these improvements, hp ^{83}Kr could reach polarization levels capable of *in vivo* applications in small animals.

6.5. Acknowledgements

This work was funded by the National Science Foundation under Grant No.: CHE-0135082 and CHE-0719423. The authors wish to thank Michael Olsen, Tom Frederick, and James Shorkey for construction specialized glassware and equipment used in these experiment, as well as Paul Wilson for assisting with animal care and usage, Dr. Elias Haddad, Charlene Horton-Garcia, and Theresa Denison for assisting with relaxation experiments and Dr. Michael Barlow for discussions regarding line-narrowed laser systems.

References:

[1] D. Raftery, H. Long, T. Meersmann, P.J. Grandinetti, L. Reven, and A. Pines, High-Field NMR of Adsorbed Xenon Polarized by Laser Pumping. Physical Review Letters 66 (1991) 584-587.

[2] D. Raftery, Xenon NMR Spectroscopy. Annual Reports on NMR Spectroscopy 57 (2006) 205-271.

[3] B.M. Goodson, Nuclear magnetic resonance of laser-polarized noble gases in molecules, materials, and organisms. Journal of Magnetic Resonance 155 (2002) 157-216.

[4] A. Cherubini, and A. Bifone, Hyperpolarised xenon in biology. Progress in Nuclear Magnetic Resonance Spectroscopy 42 (2003) 1-30.

[5] E.J.R. van Beek, J.M. Wild, H.U. Kauczor, W. Schreiber, J.P. Mugler, and E.E. de Lange, Functional MRI of the lung using hyperpolarized 3-helium gas. Journal of Magnetic Resonance Imaging 20 (2004) 540-554.

[6] T.G. Walker, and W. Happer, Spin-exchange optical pumping of noble-gas nuclei. Review of Modern Physics 69 (1997) 629-642.

[7] M.S. Albert, G.D. Cates, B. Driehuys, W. Happer, B. Saam, C.S. Springer, and A. Wishnia, Biological Magnetic-Resonance-Imaging Using Laser Polarized Xe-129. Nature 370 (1994) 199-201.

[8] H. Middleton, R.D. Black, B. Saam, G.D. Cates, G.P. Cofer, R. Guenther, W. Happer, L.W. Hedlund, G.A. Johnson, K. Juvan, and J. Swartz, Mr-Imaging with Hyperpolarized He-3 Gas. Magnetic Resonance in Medicine 33 (1995) 271-275.

[9] M.C. Fischer, S. Kadlecek, J.S. Yu, M. Ishii, K. Emami, V. Vahdat, D.A. Lipson, and R.R. Rizi, Measurements of regional alveolar oxygen pressure using hyperpolarized He-3 MRI. Academic Radiology 12 (2005) 1430-1439.

[10] J.C. Woods, C.K. Choong, D.A. Yablonskiy, J. Bentley, J. Wong, J.A. Pierce, J.D. Cooper, P.T. Macklem, M.S. Conradi, and J.C. Hogg, Hyperpolarized He-3 diffusion MRI and histology in pulmonary emphysema. Magnetic Resonance in Medicine 56 (2006) 1293-1300.

[11] T.A. Altes, J. Mata, E.E. de Lange, J.R. Brookeman, and J.P. Mugler, Assessment of lung development using hyperpolarized helium-3 diffusion MR imaging. Journal of Magnetic Resonance Imaging 24 (2006) 1277-1283.

[12] B. Driehuys, G.P. Cofer, J. Pollaro, J.B. Mackel, L.W. Hedlund, and G.A. Johnson, Imaging alveolar-capillary gas transfer using hyperpolarized Xe-129 MRI. Proceedings of the National Academy of Sciences of the United States of America 103 (2006) 18278-18283.

[13] K. Ruppert, J.R. Brookeman, K.D. Hagspiel, and J.P. Mugler, Probing lung physiology with xenon polarization transfer contrast (XTC). Magnetic Resonance in Medicine 44 (2000) 349-357.

[14] B. Driehuys, H.E. Moller, Z.I. Cleveland, J. Pollaro, and L.W. Hedlund, Pulmonary Perfusion and Xenon Gas Exchange in Rats: MR Imaging with Intravenous Injection of Hyperpolarized Xe-129. Radiology 252 (2009) 386-393.

[15] C. Hilty, T.J. Lowery, D.E. Wemmer, and A. Pines, Spectrally resolved magnetic resonance imaging of a xenon biosensor. Angewandte Chemie-International Edition 45 (2006) 70-73.

[16] L. Schroder, T.J. Lowery, C. Hilty, D.E. Wemmer, and A. Pines, Molecular imaging using a targeted magnetic resonance hyperpolarized biosensor. Science 314 (2006) 446-449.

[17] Z.I. Cleveland, H.E. Moller, L.W. Hedlund, and B. Driehuys, Continuously Infusing Hyperpolarized Xe-129 into Flowing Aqueous Solutions Using Hydrophobic Gas Exchange Membranes. Journal of Physical Chemistry B 113 (2009) 12489-12499.

[18] J. Jokisaari, P. Ingman, J. Lounila, O. Pukkinen, P. Diehl, and O. Muenster, Electric-Field Gradients Experienced by the Noble-Gas Isotopes Ne-21, Kr-83 and Xe-131 in Thermotropic Liquid-Crystals. Molecular Physics 78 (1993) 41-54.

[19] M. Holz, R. Haselmeier, A. Klein, and R.K. Mazitov, Temperature-Dependence of Ne-21, Kr-83, and Xe-131 Quadrupole Relaxation and of Xenon Diffusion in Polyatomic Solvents. Applied Magnetic Resonance 8 (1995) 501-519.

[20] D. Brinkmann, and D. Kuhn, Nuclear Magnetic-Relaxation of Kr-83 in Krypton Gas. Physical Review A 21 (1980) 163-167.

[21] C.F. Horton-Garcia, G.E. Pavlovskaya, and T. Meersmann, Introducing krypton NMR spectroscopy as a probe of void space in solids. Journal of the American Chemical Society 127 (2005) 1958-1962.

[22] Z. Wu, W. Happer, and J.M. Daniels, Coherent Nuclear-Spin Interaction of Adsorbed ^{131}Xe Gas with Surfaces. Phys. Rev. Lett. 59 (1987) 1480-1483.

[23] T. Meersmann, S.A. Smith, and G. Bodenhausen, Multiple-quantum filtered xenon-131 NMR as a surface probe. Physical Review Letters 80 (1998) 1398-1401.

[24] I.L. Moudrakovski, C.I. Ratcliffe, and J.A. Ripmeester, Xe-131, a new NMR probe of void space in solids. Journal of the American Chemical Society 123 (2001) 2066-2067.

[25] G. Pavlovskaya, A.K. Blue, S.J. Gibbs, M. Haake, F. Cros, L. Malier, and T. Meersmann, Xenon-131 surface sensitive imaging of aerogels in liquid xenon near the critical point. Journal of Magnetic Resonance 137 (1999) 258-264.

[26] Z.I. Cleveland, G.E. Pavlovskaya, K.F. Stupic, C.F. LeNoir, and T. Meersmann, Exploring hyperpolarized ^{83}Kr by remotely detected NMR relaxometry. Journal of Chemical Physics 124 (2006) 044312.

[27] G.E. Pavlovskaya, Z.I. Cleveland, K.F. Stupic, and T. Meersmann, Hyperpolarized Krypton-83 as a New Contrast Agent for Magnetic Resonance Imaging. Proceedings of the National Academy of Sciences of the United States of America 102 (2005) 18275-18279.

[28] Z.I. Cleveland, G.E. Pavlovskaya, N.D. Elkins, K.F. Stupic, J.E. Repine, and T. Meersmann, Hyperpolarized Kr-83 MRI of lungs. Journal of Magnetic Resonance 195 (2008) 232-237.

[29] D.F. Cowgill, and R.E. Norberg, Spin-Lattice Relaxation and Chemical-Shift of Kr-83 in Solid and Liquid Krypton. Physical Review B 8 (1973) 4966-4974.

[30] Z.I. Cleveland, and T. Meersmann, Density-independent contributions to longitudinal relaxation in Kr-83. Chemphyschem 9 (2008) 1375-1379.

[31] Z.I. Cleveland, and T. Meersmann, Binary-collision-induced longitudinal relaxation in gas-phase Kr-83. Journal of Chemical Physics 129 (2008) 6.

[32] K.F. Stupic, Z.I. Cleveland, G.E. Pavlovskaya, and T. Meersmann, Quadrupolar Relaxation of Hyperpolarized Krypton-83 as a Probe for Surfaces. Solid State Nuclear Magnetic Resonance 29 (2006) 79-84.

[33] Z.I. Cleveland, G.E. Pavlovskaya, K.F. Stupic, J.B. Wooten, J.E. Repine, and T. Meersmann, Detection of Tobacco Smoke Deposition by Hyperpolarized Krypton-83 MRI. Magnetic Resonance Imaging 26 (2008).

[34] Z.I. Cleveland, K.F. Stupic, G.E. Pavlovskaya, J.E. Repine, J.B. Wooten, and T. Meersmann, Hyperpolarized Kr-83 and Xe-129 NMR relaxation measurements of hydrated surfaces: Implications for materials science and pulmonary diagnostics. Journal of the American Chemical Society 129 (2007) 1784-1792.

[35] L. Zhao, R. Mulkern, C.H. Tseng, D. Williamson, S. Patz, R. Kraft, R.L. Walsworth, F.A. Jolesz, and M.S. Albert, Gradient-echo imaging considerations for hyperpolarized Xe-129 MR. Journal of Magnetic Resonance Series B 113 (1996) 179-183.

[36] J.H. Gao, L. Lemen, J.H. Xiong, B. Patyal, and P.T. Fox, Magnetization and diffusion effects in NMR imaging of hyperpolarized substances. Magnetic Resonance in Medicine 37 (1997) 153-158.

[37] J.E. Repine, Scientific Perspectives on Adult Respiratory-Distress Syndrome. Lancet 339 (1992) 466-469.

[38] G. Viegi, A. Scognamiglio, S. Baldacci, F. Pistelli, and L. Carrozzi, Epidemiology of Chronic Obstructive Pulmonary Disease (COPD). Respiration 68 (2001) 4-19.

[39] E. Babcock, B. Chann, T.G. Walker, W.C. Chen, and T.R. Gentile, Limits to the polarization for spin-exchange optical pumping of He-3. Physical Review Letters 96 (2006) 083003.

[40] M.F. Hsu, G.D. Cates, I. Kominis, I.A. Aksay, and D.M. Dabbs, Sol-gel coated glass cells for spin-exchange polarized He-3. Applied Physics Letters 77 (2000) 2069-2071.

[41] H.E. Moller, X.J. Chen, B. Saam, K.D. Hagspiel, G.A. Johnson, T.A. Altes, E.E. de Lange, and H.U. Kauczor, MRI of the lungs using hyperpolarized noble gases. Magnetic Resonance in Medicine 47 (2002) 1029-1051.

[42] R.R. Mercer, M.L. Russell, and J.D. Crapo, Alveolar Septal Structure in Different Species. J. Appl. Physiol. 77 (1994) 1060-1066.

[43] C.B.C. D.F. Kohn, Bilogy and Diseases of Rats. in: L.C.A. J.G. Fox, F.L. Loew, F.W. Quimby, (Ed.), Laboratory Animal Medicine, Academic Press, New York, 2002, pp. 127.

[44] R.W. Mair, M.J. Barlow, M.S. Rosen, and R.L. Walsworth, Improved noble gas polarization production for porous and granular media studies using narrowed-line VBG laser sources. Journal of Magnetic Resonance 25 (2007) 549.

[45] I.C. Ruset, S. Ketel, and F.W. Hersman, Optical pumping system design for large production of hyperpolarized Xe-129. Physical Review Letters 96 (2006) 053002.

[46] G. Schrank, Z. Ma, A. Schoeck, and B. Saam, Characterization of a low-pressure high-capacity ^{129}Xe flow-through polarizer. Physical Review A 80 (2009) 063424.

[47] A.L. Zook, B.B. Adhyaru, and C.R. Bowers, High capacity production of > 65% spin polarized xenon-129 for NMR spectroscopy and imaging. Journal of Magnetic Resonance 159 (2002) 175-182.

[48] J.N. Zerger, M.J. Lim, K.P. Coulter, and T.E. Chupp, Polarization of Xe-129 with high power external-cavity laser diode arrays. Applied Physics Letters 76 (2000) 1798-1800.

[49] P. Nikolaou, N. Whiting, N.A. Eschmann, K.E. Chaffee, B.M. Goodson, and M.J. Barlow, Generation of laser-polarized xenon using fiber-coupled laser-diode arrays

narrowed with integrated volume holographic gratings. Journal of Magnetic Resonance 197 (2009) 249-254.

[50] E. Babcock, B. Chann, I.A. Nelson, and T.G. Walker, Frequency-narrowed diode array bar. Applied Optics 44 (2005) 3098-3104.

[51] K. Knagge, J. Prange, and D. Raftery, A continuously recirculating optical pumping apparatus for high xenon polarization and surface NMR studies. Chemical Physics Letters 397 (2004) 11-16.

[52] B. Driehuys, J. Pollaro, and G.P. Cofer, In vivo MRI using real-time production of hyperpolarized Xe-129. Magnetic Resonance in Medicine 60 (2008) 14-20.

[53] H. Kitaoka, G.F. Nieman, Y. Fujino, D. Carney, J. DiRocco, and I. Kawase, A 4-dimensional model of the alveolar structure. Journal of Physiological Sciences 57 (2007) 175-185.

[54] S.P. Albert, J. DiRocco, G.B. Allen, J.H.T. Bates, R. Lafollette, B.D. Kubiak, J. Fischer, S. Maroney, and G.F. Nieman, The role of time and pressure on alveolar recruitment. Journal of Applied Physiology 106 (2009) 757-765.